STRUCTURAL ENERGY AND POWER FLOW USING A SCANNING LASER DOPPLER VIBROMETER

by

Jonathan D. Blotter

Dissertation submitted to the Faculty of the Virginia Polytechnic Institute and State University in partial fulfillment of the requirements for the degree of

Doctor of Philosophy
in
Mechanical Engineering

APPROVED:

Robert L. West, Chair

Michael W. Hyer

Charles E. Knight

Larry D. Mitchell

William R. Saunders

August, 1996
Blacksburg, Virginia

Keywords: Power Flow, ESPF, Intensity, Laser

STRUCTURAL ENERGY AND POWER FLOW USING A SCANNING LASER DOPPLER VIBROMETER

by

Jonathan D. Blotter

Robert L. West, Chairman

Mechanical Engineering

ABSTRACT

A three-stage Experimental Spatial Power Flow (ESPF) method which computes an experimentally derived, spatially continuous representation of the structural power in 1-D and 2-D structures is presented. The three stages of the ESPF method consist of first using a scanning laser Doppler vibrometer (SLDV) to acquire spatially dense measurements of the structure's dynamic response. Second, the continuous 3-D complex-valued velocity field is solved from the laser data. Third, a spatially continuous model of the power is computed from the velocity-field model obtained in stage 2.

The results of the ESPF method were validated by using both simulated and experimental laser data. In the simulated laser data cases, the power injected into a simply supported plate computed analytically, compared to within 1.33% of the power injected as computed by the ESPF method. In the experimental validation, three methods were used to compute the power injected and extracted from a simply supported plate forced with two shakers. The three methods consisted of the ESPF method and two methods of computing the injected power using impedance head type measurements. The injected power results

were compared at four different frequencies. These frequencies were 79.0 Hz, 311.0 Hz, 909.0 Hz, and 1100.0 Hz. In all cases, the injected and extracted power results of the three methods compared to within 20% and to within 12% for all cases except the 909.0 Hz case. These results are currently better than other experimental techniques.

Advantages of this method are 1) a spatially continuous representation of the power is computed 2) the affects of the actual boundary conditions and near-field effects of the structure are inherently measured by the SLDV 3) the SLDV does not affect the response of the structure by mass loading and is fully portable for in-field testing 4) the method allows for convergence of the power-flow vector field in addition to convergence of the velocity field and 5) the ESPF method is extendable to account for power due to in-plane motion and to account for shells of arbitrary geometry.

Acknowledgements

First and foremost I thank my wife Marti, and two daughters Sara, and Hannah. Without their support I never would have had the stamina required to complete this work. They provided great moral support, encouragement, and a lot of happiness along the way.

I would like to thank Professor Robert L. West for the many things outside of engineering that he taught. I thank him for always demonstrating high moral and ethical standards and being up front on all issues. He taught that a person must "Stand on their own merits and live with it." I have sincerely appreciated his support in publishing papers, attending conferences, and completing this work.

I would also like to thank Professor Larry D. Mitchell for sharing his expertise in many areas of engineering. He was always willing to come down in the lab, get his hands dirty, or better said, get my hands dirty and help out.

I also express my sincere appreciation for the other members of my committee, Professor Michael W. Hyer, Professor Charles E. Knight, and Professor William Saunders. They all provided significant insight and demonstrated a genuine concern in my research. I also appreciate Professor Ricardo Burdisso for his willingness to be a substitute on my examining committee.

I thank George and Gladys Cunningham for providing the Cunningham Fellowship which provided me with three years of funding to perform my research.

I am thankful for the many friends who acted as great sounding boards and helped with the experimental testing. I give special thanks to David Coe, Monty Moshier, Scott

Vendemia, Joseph Fritszhe, David Montgomery, Chris Doktor, and Brian Lindholom. I would also like to thank the members of Scout Troop 142 who over the past three and a half years and over 50 nights camping have provided a great relief from the day to day pressures of school.

Finally, I would like to thank my parents Tom and Jill Blotter. I thank them for all the "five-step-behinders" I had as a child in which they taught me the "work ethic" and that "when the going gets tough I had better get going." They have sacrificed many of their wants and needs to provide for their kids. Without their endless support I never could have completed this goal. I only hope that I can return to their grandchildren what they have given to me.

If it were not for the "tough times" the "good times" wouldn't feel so good

Contents

List of Figures

List of Tables

Chapter 1

Introduction

1.1 Power-Flow Concept

We live in a world that most people consider to have progressed and improved due to the vast technological developments which have taken place over the centuries. However, some would also argue the second law of thermodynamics and state that all the developments and inventions over the years have actually caused a greater disorganization in our universe.

Regardless of your point of view, there will always be a push to make things stronger, faster, lighter, and cheaper. These measures have lead the engineering design world to no longer accept the "just use a large safety factor so it won't break" type design. To be competitive, engineers must use new design technologies which often require analytical development as well as cross-validation with experimental testing. Simple static designs in which the load paths in the structure are determined no longer provide the necessary design results in many applications. However, applying the same ideas of developing a load path but instead of using the load path, use an energy path, the dynamic characterization of the structure can be determined. The research presented in this dissertation is based on these ideas of using an energy map in the design or analysis stages of the structure.

In the literature, analytical and experimental methods which seek to develop a spatial map of the power or energy flow in vibrating structures are generally referred to as power-flow

methods. Power is defined as the time-averaged product of the phased generalized force and velocity components in the direction of the force. The term power flow is derived from the fact that since the directions of the generalized forces are known from the assumed positive directions in the mechanics model, the direction of the power is also known. Hence, since both the magnitude and direction are known, power can be represented as a vector. When plotting power vectors, a flow-type pattern is generated, and hence the term power flow.

The concept behind power-flow methods is that the magnitudes of the energy sources and sinks, as well as the paths of energy transmission, can be determined. Once the energy path has been determined, the structure can theoretically be designed or controlled to channel or dissipate the energy as required. The design or control problem becomes a problem of "managing" the energy in the system. As a result, power-flow techniques have been proposed and applied to a broad range of problems associated with structural dynamics, such as noise control, structural acoustics, adaptive control, dynamic characterization, non-destructive evaluation, and health monitoring.

Power flow and modal analysis techniques provide very different results. Power flow provides information on how power is injected into a structure and the flow paths it takes to transfer vibrations to other connected structures. While, modal analysis is a representation of the harmonic movements of the vibrating system.

The difficulties associated with many of the present power-flow techniques stem primarily from two issues. The first issue is that a spatial model of the structure's dynamic response is required in order to spatially map the energy path in the structure. Secondly, it is extremely difficult to analytically model the actual boundary conditions, near-field effects, and geometry of the test structure. Analytical models provide spatial representation of the response, but accurate modeling of the actual boundary conditions on the structure are unknown both in magnitude and representation. Experimental models inherently include the actual boundary conditions in the measurements of the dynamic response, but do not typically develop an ad-

equate spatial model of the response and in many cases are unable to represent the near-field effects.

The Experimental Spatial Power Flow (ESPF) method presented in this dissertation is unique in that it addresses the issue of a spatially continuous power-flow model, and inherently includes the actual boundary conditions since it is derived from experimental measurements. These capabilities of the ESPF method provide the link between the analytical and experimental power-flow methods.

The ESPF method is developed around the high spatial density measurement capability of a scanning laser Doppler vibrometer (SLDV). The high spatial density measurement is used to solve for a spatially continuous representation of the 3-D complex-valued velocity field over the structure. This velocity field is integrated in time to obtain the 3-D continuous displacement field. An appropriate deformation mechanics model is used to relate the generalized forces to the experimentally derived displacement field. By taking the dot product between the generalized force and velocity-vector fields, a spatially continuous representation of the power is obtained. Since the real and imaginary velocities are kept separate throughout the solution, the real and imaginary power components can be computed. The real part of the power is termed the active power and represents the net energy flow in the structure. By computing the real power component over the structure, the magnitudes and locations of the energy sources and sinks, as well as the paths of energy transmission can be determined. This information can provide significant insight to both the design and analysis stages of a structure. The imaginary power is termed the reactive power and does not contribute to the net energy flow but is believed to be a representation of the reverberant energy in the structure.

Figure 1.1 illustrates how the development of the research presented in this document can contribute to the structural dynamics engineering community. The general area of structural dynamics is shown to be broken down into experimental and analytical techniques. As pre-

viously mentioned, large inadequacies currently exist in both the analytical and experimental power-flow techniques. The proposed research will combine the strengths of the experimental and analytical power-flow methods and result in a tool which can be developed for use in many industrial applications as well as fundamental research.

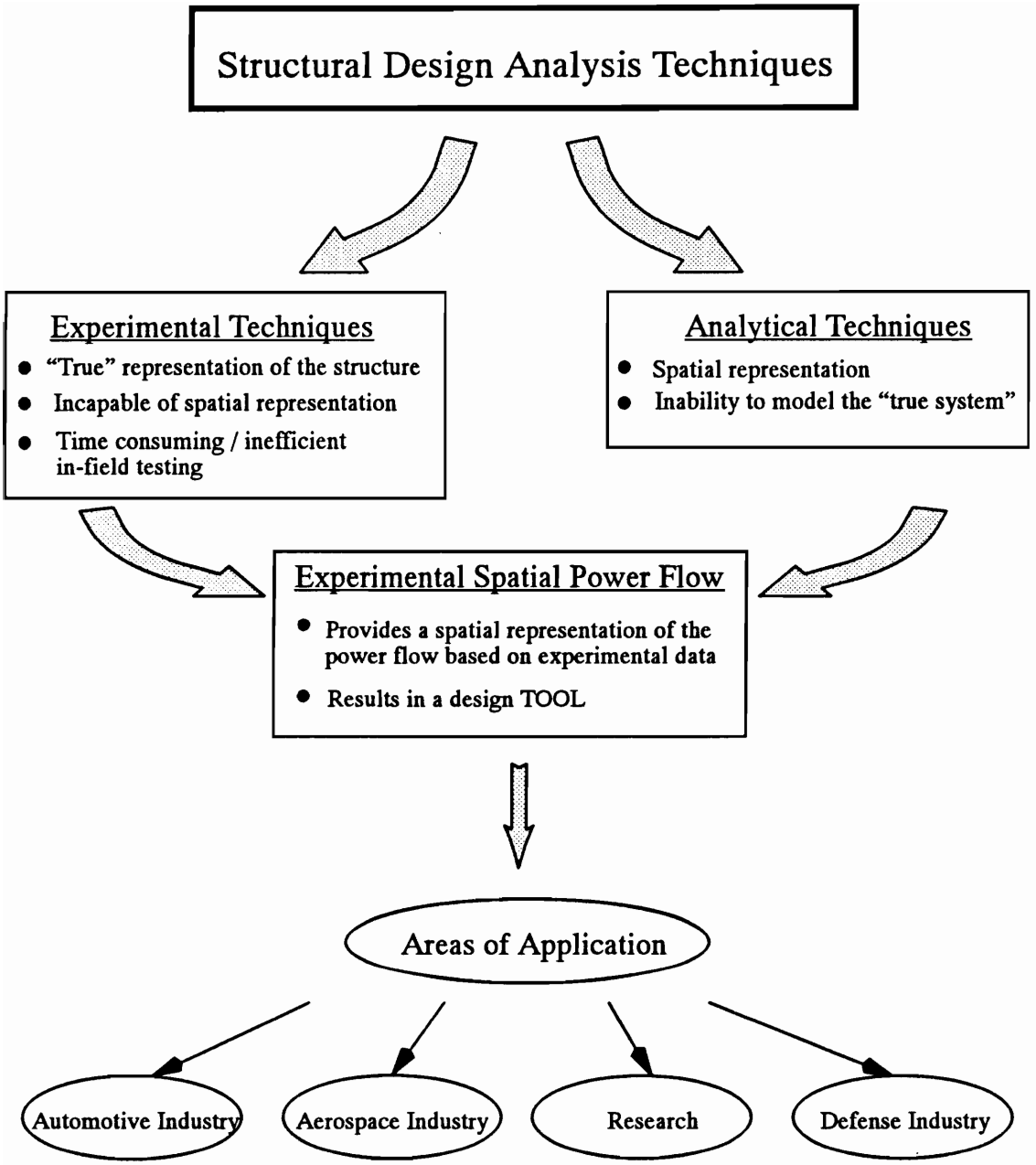

Figure 1.1. Impact of the ESPF method to the general area of structural dynamics

1.2 Research Goal

The goal of this research is to develop an Experimental Spatial Power Flow (ESPF) method which derives a spatially continuous model of the power in the structure from experimental data acquired using a scanning laser Doppler vibrometer. The ESPF method developed from this research will be used as a tool in the design and analysis stages of the structure. The ESPF method will account for power due to transverse motion in 1-D and 2-D structures and must be capable of computing both the magnitudes and spatial locations of the energy sources and sinks as well as the paths of energy transmission. The ESPF method is a novel approach and will provide significant impact to current techniques in that it provides a spatially continuous representation of the power which is derived from experimental data.

1.3 Research Hypothesis And Objectives

The ability to spatially compute and statistically qualify power in vibrating structures will affect many areas of research as shown in Fig. 1.1. The ability to experimentally locate energy sources and sinks and compute the paths of energy transmission will be a useful tool in both the design and analysis stages of a structure. The proposed research goal of Section 1.2 will be realized by developing a three-stage experimentally based process. The three stages will consist of; 1) Test setup and data acquisition using a scanning laser Doppler vibrometer (SLDV); 2) Velocity-field reconstruction using the Experimental Spatial Dynamics Modeling (ESDM) technique; and 3) Power computation based on the experimentally derived velocity field obtained from step 2. Each of these three main stages require the development of several smaller research objectives as shown in Table 1.1. The theoretical development of these research objectives will be thoroughly discussed in Chapter 3.

Table 1.1. Outline of the ESPF research objectives

1. Test Setup and Data Acquisition

A. Test setup and data acquisition techniques to improve the quality of the laser data

B. Instrument calibration

C. Signal processing

2. Velocity-Field Representation

A. Laser registration process

B. ESDM velocity solution

C. Quintic B-spline basis functions / Jacobian matrix

3. Power-Flow Computation

A. Power-flow concept

B. External source injected power development

C. Spatially continuous computation of the generalized forces and velocities

D. Convergence of the power-flow vector field

E. ESPF method validation process

1.4 Dissertation Outline

The purpose of this dissertation is to illustrate the need for the ESPF method, provide the theoretical development behind the method, and present and validate the ESPF concept with simulated and actual laser data. This is done by first presenting the detailed literature review which brought to light the idea of the ESPF method. The underlying theory of the ESPF method is then presented. Simulated laser results are then used to prove the validity of the theoretical development. Finally, experimental results will be presented which illustrate the novel abilities of the ESPF approach. The chapters of this dissertation will present these issues as follows.

Chapter 2. Literature Review

The purpose of this chapter is to provide a detailed historical outline of the key research which lead to the concept of the ESPF method. Several different analytical and experimental power-flow methods will be introduced and the differences between these methods and the ESPF method will be emphasized.

Chapter 3. Theoretical Development of the ESPF Method

The theoretical development of the ESPF method is broken down into three major sections. These sections are: 1) Test setup and data acquisition; 2) Velocity-field representation; and 3) Power-flow development.

Test setup and data acquisition

The test setup and data acquisition processes also have three major components. These components consist of: 1) The physical steps taken, such as test structure surface preparation, to improve the quality of the measured data; 2) Calibration of all the equipment used in the experimental process; and 3) Signal processing of the measured signals. This research will focus on the development of the first two components and use existing developments for the signal processing.

Velocity-field representation

This section briefly presents the theory behind the laser registration process and ESDM velocity solution. The general procedures in the laser registration technique will be explained and the key equations in the ESDM velocity solution algorithm will be presented. The development of the quintic B-spline basis functions and the Jacobian matrices which were developed as part of this research are also presented.

Power-flow development

The underlying theory of power in vibrating structures is presented in this section. The equations from which the power is computed in the ESPF approach are derived from basic relationships. Equations for the power injected by distributed loads in beams and plates are also derived and discussed. This is the key section which provides the theoretical understanding for Chapters 4 and 5.

Chapter 4. Laser Simulated Results

Method comparison and theoretical validation

The purpose of this chapter is to validate the theory behind the ESPF approach. It will be shown that the ESPF method is theoretically sound and capable of computing the power given "perfect" (i.e. noise free) data. The "perfect" data is obtained by developing a computer generated laser simulator in which the operator has control of the signal noise. The most fundamental test, will be to show that the energy entering the structure, through the applied loads, is conserved and accurately represented both in magnitude and spatial location by the ESPF results. This validation process will be performed for both beams and plates. The results presented in this chapter will also validate the software developed for the ESPF method in that the same code will be used with real experimental data.

Chapter 5. Experimental Results

This chapter is divided into two main sections. The first section presents the experimental setup and the validation procedures. The second section presents the experimental results.

Experimental setup

This section describes in detail the approximated simply supported plate setup used to illustrate the capabilities of the ESPF method. Three different methods of computing the

power in the plate are used to validate each other. This section describes these three methods and explains the validation process. The validation process will be similar to the process presented in the simulated laser results in that the power injected by an external source will be compared to the power computed by the ESPF method.

Experimental results

ESPF results will be presented for four different forcing frequencies of the plate. These frequencies will illustrate various types of power-flow patterns. The capabilities of the ESPF method will be made clear by comparing the results with other known methods of power computation. The ability of the ESPF method to obtain a converged solution of the power will also be illustrated.

Chapter 6. Summary

Finally, the entire dissertation will be summarized. The strong points of the ESPF method will be reemphasized as well as the areas where continued research should be performed.

Chapter 2

Literature Review

2.1 Literature Review

The goal of developing an experimental power-flow method capable of providing a continuous representation of the power flow in a structure was generated from a comprehensive literature search. This section outlines the major contributions in the literature that lead to the development of the proposed research goal.

In 1990, the Modal Analysis Laboratory at Virginia Tech was awarded an NSF research grant which entailed the purchase of a scanning laser Doppler vibrometer (SLDV). At that time the grant was the largest NSF grant that had been awarded for research equipment. Since receiving this grant, many investigations as to possible applications of the laser have been performed. During these investigations many engineering degrees have been earned through research in understanding the laser capabilities, laser registration techniques, and velocity-field reconstruction methods [1][2][3][4][5][6]. After the development of these primary capabilities came the need to further the technology and build upon the laser applications. It was during this time that the ideas of extracting energy or power-flow maps based on laser data were initiated by Professor Robert L. West.

Energy travels through vibrating structures as a result of plane waves which are generally reverberant in nature. The strongly reverberant field that develops in these structures makes

it difficult to see the small part of the wave responsible for the transfer of energy in the structure. This was the basic motivation for Noiseux whom in 1969 published one of the first theoretical developments of the equations for power in beams and plates [7]. His goal was to develop a method which would un-mask the energy path and provide a spatial map of the power in these structures. Noiseux verified his theoretical development by comparing with experimental results obtained from an accelerometer-based power-flow approach. Since Noiseux's initial work, the interest in techniques which describe the energy in vibrating structures has grown at a increasingly rapid rate.

Previous to this development by Noiseux, Lyon in 1959, computed the power flow between two lightly coupled linear resonators. This was the ground work research for what has become known as Statistical Energy Analysis (SEA). In 1975, Lyon published a text book on the theory of SEA [8]. SEA is one of the first computational methods used to compute the power in structures at high frequency [9]. The SEA technique can be derived by a conventional modal approach in which the main structure is broken down into substructures. The response of each substructure is then expressed in terms of the response of its modes. Orthogonality and closure properties of the mode shapes are used to average over the spatial extent of the substructure so that the response can be defined in terms of its modal energies [10]. SEA is a useful method for determining the behavior of built-up structures but does not provide a spatial mapping of the power in the structure and detailed spatial variations in the power are not obtained. SEA is most suitable for cases of broad-band excitation over a band width encompassing many natural frequencies. The two reasons for these restrictions are that: 1) the basic relationship between power flow and energy difference between oscillators takes a very simple form provided that the excitation spectrum extends over a frequency range encompassing the resonance frequencies of the uncoupled modes involved; 2) a statistical description of the parameter of the coupled system is only useful if a reasonably large population of modes is involved [11] [12]. Other key publications on SEA were published by

Remington and Manning [13]. In their paper the authors showed that the power flow between two coupled rods averaged over a sufficiently broad frequency band agreed closely to the SEA predictions. Woodhouse published a paper which provides a general understanding of the SEA concept. The goal of his paper was to present the SEA concept without all of the theoretical development and to answer the question of what can SEA do for me [14].

Paralleling the developments in SEA, Pavic in 1976, published a two part paper that presented the theoretical development of the power-flow equations in plates [15]. This work was similar in nature to the previous work performed by Noiseux. In these papers, Pavic used an accelerometer-based experimental approach to compute the power using a finite difference technique to compute the generalized forces. A complete formulation using this method requires a minimum of 4 sensors, 13 measurement points, and 34 different measurements between the pairs of sensors in order to determine the amplitudes and phase between the sensors. Many experimenters have used this principle but when they have been faced with the need to increase the number of measurement points they have resorted to the use of mechanisms grouping the sensors which impose significant loading on the structure. Since the two main publications of Noiseux and Pavic, the area of power flow developed at a moderate rate through the 1980's with both analytical and experimental methods being investigated.

In 1985, Pavic published another paper in which strain gauges were used to measure the displacements in beams and plates [16]. He concluded that is was difficult to obtain sufficient signal-to-noise ratios using strain gauges unless large amplitudes of vibration were present or unless only the far-field intensity component was considered.

In 1985, Maynard et al. presented a measurement technique based on near-field acoustic holography (NAH) [17]. They demonstrated that relatively accurate results compared to the previous accelerometer based techniques could be obtained with the NAH technique. The main draw backs of holography techniques are the requirements for the test setup. It is not practical to transport a holographic setup so that in-field testing can readily be performed.

In their approach, Maynard et al., used a 256 microphone array to capture the response of the plate excited by two point forces. As they presented their results they emphasized the importance of careful calibration. Their method also works primarily for beams and flat plates. Since this initial work several other power-flow techniques based on NAH have been published [18][19][20].

In 1989, Nefske and Sung published the basic theory for computing power flow in a beam and coupled beams using a finite element approach [21]. Nefske and Sung based their approach on conserving energy through a differential control volume which resulted in a heat conduction type partial differential equation where the vibrational energy density plays the role of the temperature and damping acts as a heat sink. This approach reduces the order of the governing differential equations and has been successfully applied to point loaded beams. However, Langley, illustrates that the heat conduction analogy is not valid for 2-D structures such as plates. Langley further presented a wave-equation approach which still reduces the order of the governing differential equations and can be applied to both beams and plates [22].

In 1990, The Third International Congress on Intensity Techniques was held in Senlis, France [23]. This congress prompted the rebirth of the power-flow concept. In this congress, several analytical methods were presented. Hambric presented a finite element approach to computing power flow in beams, plates, and simple trusses [24]. He illustrated the ability of the finite element method to compute results over a large frequency range and the ability to compute a spatially continuous representation of the power-flow field over the structure. Gavric et al., also presented a finite-element-based approach to compute the power flow through beam-plate assemblies [25]. These finite element based approaches can provide accurate results in cases of low spatial wave numbers. However, as the spatial wave number increases, the finite element method becomes inefficient and expensive, due to the large number of elements or the increasingly high order of the elements required to appropriately

represent the field. The ability to correctly model the actual boundary conditions and account for damping in these analytical models is also a difficult task which can greatly effect the power-flow results. In most of the analytical methods presented, structures with free boundary conditions are used to simplify the modeling process.

Several experimental power-flow methods were presented in the same 1990 International Congress on Intensity Techniques. Gavric et al. and others presented several accelerometer based approaches which built on the previous developments of Noiseux and Pavic. The various methods developed were based mainly on a two or a four accelerometer approach. Various methods of wave decomposition and finite difference techniques were used to compute the generalized forces from the experimental data. If the boundary conditions and near-field effects are measured using these methods it can be extremely time consuming. Hence, the accelerometer based methods in general do not provide a detailed spatial sampling of the structure's response.

Carroll presented a paper on the phase accuracy required between the accelerometers used in the 2 and 4 accelerometer based methods [26]. It was shown that for moderate to lightly damped structures, phase accuracy on the order of 0.1 degree was required to accurately measure power flow. This high phase accuracy requirement is needed in order to separate the energy carried in the standing and traveling waves. This paper also discusses the types of accelerometers and the test conditions that provide the best results. Unfortunately, this work was only investigated for beams. This work was based on Carroll's Ph.D. dissertation [27].

Various laser techniques were also presented in the 1990 congress. McDevitt, Koopmann, and Burroughs presented a laser vibrometer approach which used two laser vibrometers activated by the same laser which have their beams focused at two closely spaced points [28]. In this method the two laser beams are used to replace the two accelerometers and near-field information is not obtained. Hayek et al. presented a laser Doppler vibrometer technique in

which four points in the near-field and four points in the far-field were measured by the laser [29]. These points along with a finite difference technique were used to compute the power in a flat plate. The entire surface of the structure using this method is not easily scanned and the results at four points are used to reconstruct the entire field. This method is very similar to the four accelerometer method except that the laser is used as the transducer. Since these initial investigations of laser-based approaches published in 1990, further advances in structural power computation using laser technology have been somewhat slowed. This has been due to the fact that few researchers have been investigating the problems because of the relatively high cost of the laser. However, due to the large inadequacies of the current experimental methods, researchers have recently regained interest in using laser technology. Special interest has been built around scanning laser Doppler vibrometers which use electronically controlled mirrors to position the laser beam on the structure and are capable of high spatial density measurement of the vibrating surface.

In 1992, Bouthier and Bernhard presented a finite element based method that takes into account the local absorption of energy due to internal damping and also predicts the intensity field in plates [30]. Their development was limited to the far-field and was never cross validated with experimental results.

Several papers in the area of control using power as the control parameter have recently been presented. One of the most recognized papers was written by Tanaka et al. in which methods for predicting the power-flow patterns given the mode shape of the plate were presented [31]. Tanaka uses a feedforward control technique on a simply supported plate with two shakers. He illustrates with both analytical models and experimental results the various power-flow patterns which can develop in the plate. In 1993, Gibbs completed a Ph.D. dissertation in which the goal was to sense and adaptively control, simultaneously, the flexural and extensional waves in thin beams using piezoelectric actuators and sensors [32]. Other papers which focus on power-based-control techniques are given by Miller and Hall [33] and

Pan and Hansen [34]. Health monitoring and damage detection can also be investigated using power techniques as discussed by Norwood and Wood [35].

In 1993, The Fourth International Congress on Intensity Techniques was held in Senlis, France [36]. Papers in this conference ranged from new theoretical developments to new experimental techniques. Lee et al. presented the only paper that dealt with a laser-based approach [37]. In their approach, a laser probe was used to measure the velocity at a few discrete points. The laser probe consisted of 3 laser beams and was designed to measure one in-plane and one out-of-plane component of the displacement vector field. Only preliminary results were presented and no further work on this technique has been found.

The Inter-Noise 95 Conference contained well over 20 papers dedicated to analytical and experimental power techniques [38]. Various laser-based approaches were also presented. Morikawa et al. presented a laser-based approach in which two different types of laser heads were used [39]. The first consisted of a single laser which measured the displacement perpendicular to the structure. The second laser head consisted of two laser beams which formed an oblique incident angle and was used to measure the in-plane power component. Their power computation method consisted of using a few discrete points on the structure and a finite difference technique to compute the generalized forces. Benes, E. et al. also presented a laser-based approach which uses a total of 6 in-plane laser Doppler vibrometers to determine the in-plane velocity components at six points on the vibrating surface [40]. Again, their method was based on a finite difference technique for computing the generalized forces.

A few other laser-based approaches and measurement techniques have been presented. However, they are all based on measuring a few points on the structure and computing the power based on a finite difference approach. None of the current laser methods, save the ESPF method presented in this dissertation, are based on scanning laser Doppler vibrometers. The SLDV adds another complete dimension to the power-computation methods in that

spatially dense measurements can be obtained. This allows a continuous model of the velocity and power fields to be computed.

In 1994, Montgomery developed an Experimental Spatial Dynamics Modeling (ESDM) technique which solves for the spatially continuous 3-D complex-valued velocity field over the entire surface of the structure [2]. This velocity measurement technique employs a scanning laser Doppler vibrometer which provides spatially dense sampling of the velocity field.

The Experimental Spatial Power Flow (ESPF) technique presented in this dissertation builds a power model using the experimentally derived velocity model obtained from the ESDM technique. The goal of the ESPF development is to bridge the gap between the present analytical and experimental power-flow models. The ESPF method is a unique power-flow method in that it is based on the use of an SLDV. This provides the means of computing a spatially continuous model of the power in the structure. It will further be shown in this dissertation that the ESPF method is capable of accurately computing both the magnitude and location as well as the paths of energy transmission in a vibrating structure. These capabilities provide results which other experimental and analytical methods are incapable of computing.

Since these conferences and publications mentioned several other major conferences such as Inter-Noise 96 and the Fourth International Congress on Sound and Vibration will consist of several sessions dedicated solely to new developments in power-flow techniques. The promise and the need for an experimentally derived, spatially continuous power-flow model has been realized. Research in this area will continue to rapidly grow based on the strong interest of industry and the wide area of application to which power-flow techniques can be applied.

Chapter 3

Theoretical Development of the ESPF Method

3.1 Introduction

The ESPF method can be broken down into three fundamental stages. These three stages are the data acquisition, velocity-field representation, and power computation. This chapter discusses in detail the underlying development of each stage.

3.2 Test Setup and Data Acquisition

Nomenclature

t	time
$Y()$	general time-signal function
α	signal amplitude
β	time-signal model coefficient
ϕ	phase angle
ω	driving frequency

3.2.1 Introduction

The data acquisition process has three major components which significantly affect the quality of the experimental results. The first component consists of the steps taken in the test

setup and data acquisition process which help improve the quality of the measured data. The second component consists of a thorough calibration of all the equipment used in the test. The third component consists of the signal processing techniques used to develop time signal models of the force, acceleration, and velocity signals. This section discusses these three components in detail.

3.2.2 Test Setup Design Factors

Proper test setup and instrument calibration are crucial in acquiring high quality data. The test setup should be designed for repeatability and to minimize the effects of temperature fluctuations, wind disturbances, and various other conditions which are not constant.

In order to compute the continuous 3-D velocity field the position and orientation of the laser relative to the structure must be known. The process of determining the laser position and orientation is known as laser registration. Accurate laser registration is vital to acquiring useful velocity data. Therefore, the test setup should be designed to provide high quality laser registration results. Free hanging structures have typically been known as being highly repeatable tests and the boundary conditions are easily modeled by analytical methods. However, when using an SLDV which requires a registration process that is highly sensitive to slight movement of the test structure, free-hanging structures are not very repeatable and do not provide as high quality results as do test structures that are fixed to ground. This is because the structure can easily move during the scanning process. This movement renders the laser registration invalid.

When scanning two-dimensional structures such as beams and plates a registration point which provides an out-of-plane component should also be incorporated in the registration process. This out-of-plane point will help the registration algorithm converge to a more accurate solution.

It was also demonstrated that significant backlash associated with the mirror scanning system in pointing the laser beam can exist. For example, if the laser beam is moved to a particular point on a structure and the voltages from the positioning mirrors are recorded, then the laser beam is moved randomly over the structure and returned to the original voltages which marked the starting point. When the laser is approximately 3 m from the structure, the laser beam will be off the original point by as much as a 3/16 of an inch in both the x and y directions. To minimize this backlash effect each time the laser beam is moved it should first be moved to an extreme corner of the laser range and then to the point of interest. It was shown that moving the laser only ten digital-to-analog converter (DAC) steps in each direction does not clear out the backlash. With the current registration process it is further suggested that after the structure has been registered a scan of just the registration points be performed. This should be done in addition to the scans of the entire structure.

Significant error in the laser registration can also occur due to thermal drift. The laser should be allowed to warm up for at least twenty minutes before performing the laser registration process. The current laser systems can be provided with thermal jackets which decrease the warm up time and help maintain a constant temperature during the test. However, in the system used in this dissertation these thermal jackets were not supplied with power and could not be used as effectively.

Surface preparation techniques such as coating the structure with Magnaflux, which is a white, spray-on, dust, or a highly reflective paint are not required. However, it has been determined by many users that these preparations do significantly improve the quality of the signal produced by the SLDV [1]. These surface preparations improve the SLDV signal quality by increasing the back scatter and hence the intensity of the reflected laser beam. Also by coating the surface of the test structure the SLDV is more easily focused and maintains this high focus even when scanning over large areas and at high angles of incidence.

3.2.3 Equipment Setup and Calibration

Three independent methods of computing the power in the structure were used in the experimental test results discussed in Chapter 5. This section describes the equipment setup for the three methods and discusses the calibration procedures and results of the equipment involved.

Method 1 was the ESPF method which consisted of using the SLDV to measure the velocity field over the entire surface of the structure. Method 2 consisted of acquiring force and acceleration data from impedance-head measurements. Impedance heads are transducers which consist of both a force gage and an accelerometer. The data for these two methods was acquired simultaneously using a Frequency Devices 9016 low-pass Butterworth 8-pole filter, an Iotech ADC488/8S analog-to-digital converter (A/D), and a Silicon Graphics Iris Crimson workstation. Method 3 consisted of collecting force and acceleration data from the impedance heads using an HP 35665A Dynamic Signal Analyzer. The digital-to-analog converter (D/A) used to control the scanning mirrors of the laser was an Iotech DAC488/4. The equipment schematic for all three methods is shown in Fig. 3.1.

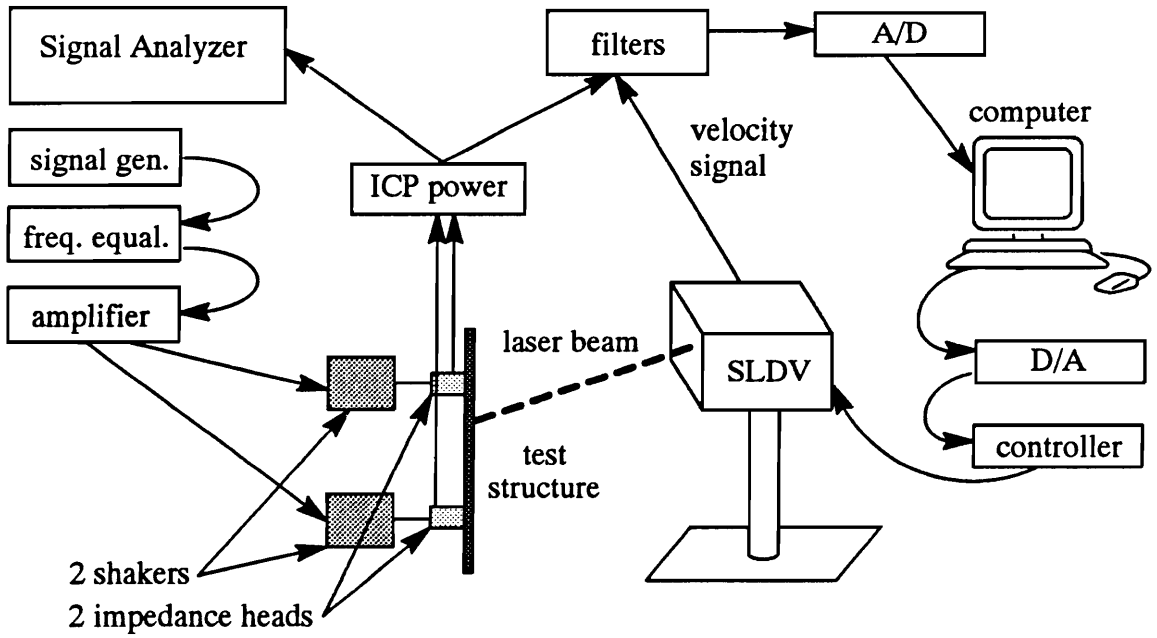

Figure 3.1. Data acquisition setup schematic

Before the equipment setup shown in Fig. 3.1 is performed the impedance heads, integrated-circuit piezoelectric (ICP) power supplies, and the laser should be independently calibrated. This calibration should then be followed by a single calibration of the entire loop which contains the filters, A/D, and computer. This section continues by presenting the calibration procedures and the results obtained. These results and an understanding of the uncertainty in these results are vitally important to the interpretation of the data presented in Chapter 5.

Impedance heads

Under most circumstances calibration sheets traceable to a national standard will be provided for the impedance heads. However, the impedance heads used in this research were a relatively new design and were not provided with calibration sheets. Hence, this calibration needed to be performed. The results obtained from this calibration provide significant insight to the quality of the power method comparisons which are made in Chapter 5.

The impedance heads were calibrated using an accelerance technique. The governing equation is Newtons second law of motion as shown by Eq. (3.1).

$$F = m\,a \tag{3.1}$$

Rearranging, it can be shown that the accelerance, $\left(\frac{a}{F}\right)$, is equal to one over the mass as shown by Eq. (3.2). Equation (3.2) indicates that the mass of a vibrating structure can be experimentally determined by computing the accelerance from measured acceleration and force signals.

$$\frac{a}{F} = \frac{1}{m} \tag{3.2}$$

Assuming that the acceleration and force are experimentally measured using an accelerometer and a force gage, Eq. (3.2) can be written in terms of voltages and calibration factors. Solving for the force calibration constant results in Eq. (3.3). The units of each component are also shown in Eq. (3.3). It is noted that the force and acceleration ratio is volts over volts and hence dimensionless.

$$Force\ Cal.\ Factor\left(\frac{mv}{\frac{m}{N}}\right) = \left[Accel.\ Cal.\ Factor\left(\frac{mv}{\frac{m}{s^2}}\right)\right]\frac{1}{Mass\ (kg)}\frac{F}{a} \tag{3.3}$$

The experimental setup used to calibrate the impedance heads consists of a relatively large mass, an electromagnetic shaker, a reference accelerometer, and the impedance head as shown in Fig. 3.2. Details of the test mass dimensions and properties are shown in Fig. 3.3. A more detailed discussion of this calibration method, which includes a discussion of the various system models, was presented by Mitchell et al. [41].

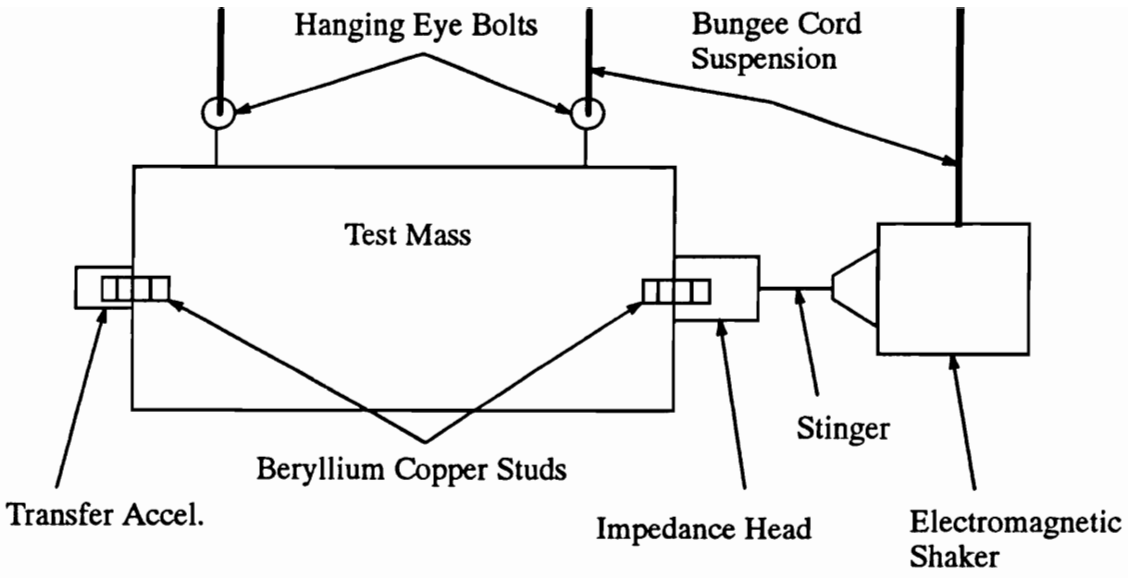

Figure 3.2. Impedance head calibration setup

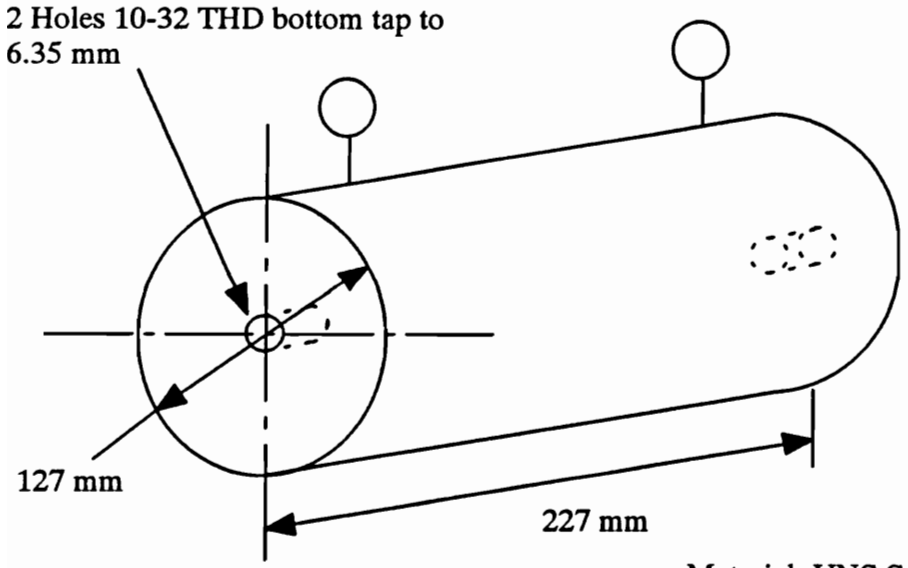

Total mass including eye bolts, 1 transducer, and the mass below the force gage of 1 transducer = 22.72 kg, 50.08 lbs

Material: UNS S 30400 Annealed

S_y = 241.32 MPa

S_{ut} = 586.05 MPa

$$\gamma = 76,004.8 \frac{N}{m^3}$$

Figure 3.3. Test mass dimensions and properties

In the calibration process, the mass is forced with a random signal from which the voltage accelerance ratio can be computed. Using the known mass and the calibration factor for the accelerometer the force calibration factor can then be computed using Eq. (3.3).

The impedance heads used were the old PCB model 288C01. This model number has now been changed to U288C01 and manufacturing has been discontinued. This is due to either a design flaw or a manufacturing flaw which caused the transducers to be torque sensitive. When asked, PCB would not comment on the type of flaw found in the gage. PCB reproduced the impedance head and removed the torque sensitivity leaving the model number as 288C01. One of these new impedance heads (Model 288C01 SN 864) with a calibration traceable to NIST was used as the reference accelerometer in the calibration process.

Since the impedance heads were determined to be torque sensitive each transducer was calibrated over a torque range of 14-20 in-lbs. Figure 3.4 shows plots of the calibration factor over a frequency range of 0-800 Hz for the impedance head model U288C01 SN 708. The phase between the reference accelerometer and the impedance head is also shown. The dip in the plots around 290 Hz is due to a system resonance. There also appears to be another system resonance around 830 Hz. Figure 3.4 indicates that the calibration factor can range from 124 mv/lbs to 127 mv/lbs depending on the torque with which the gage is mounted to the structure. This can result in about a 2.5% error in the reading which is just due to the torque with which the impedance heads are attached to the structure.

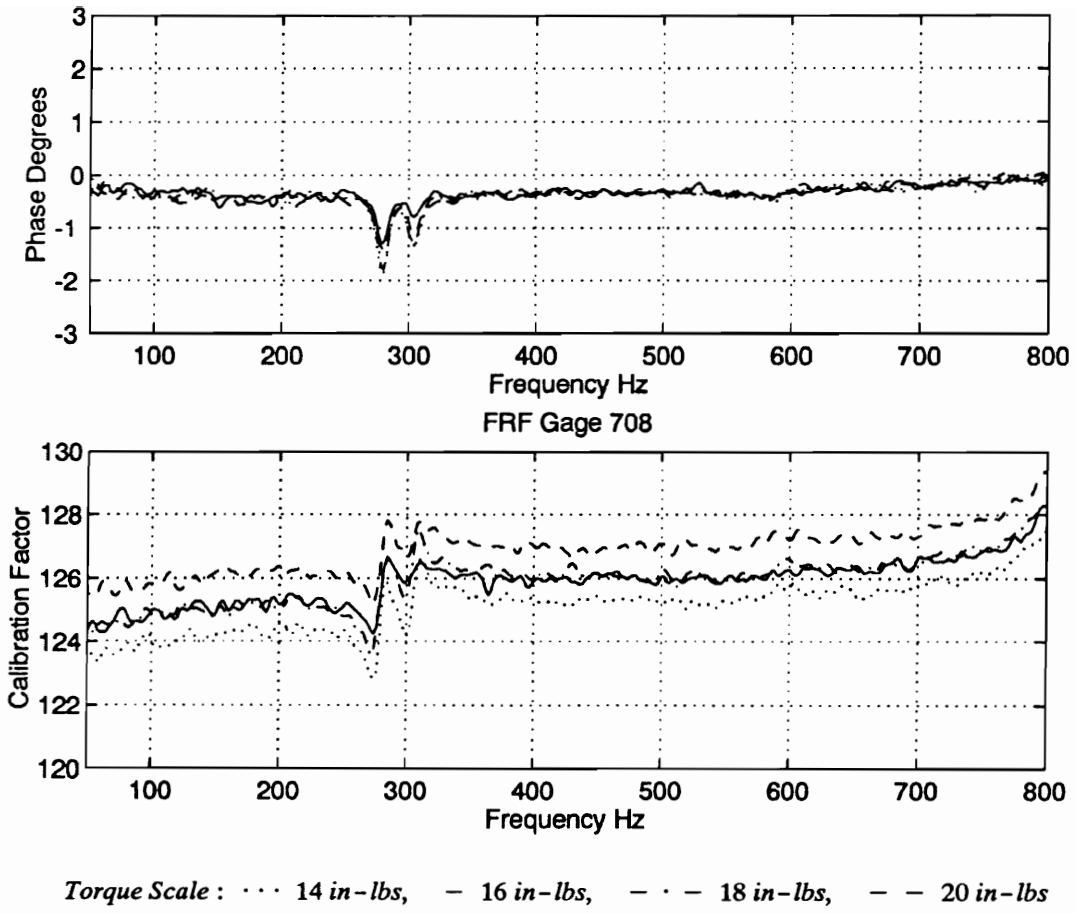

Figure 3.4. Frequency response plot of the force gage from the impedance head SN 708 and the reference accelerometer

This same type of plot which indicates the calibration factor and the phase over the torque range of 14-20 in-lbs for the second impedance head SN 784 is shown in Fig. 3.5. These results indicate that the calibration factor ranges from 114 mv/lbs to 119 mv/lbs depending on the torque. This could result in an error of 4.4%. It is further noted from these plots that the first resonance frequency has shifted to a slightly higher frequency of approximately 300 Hz.

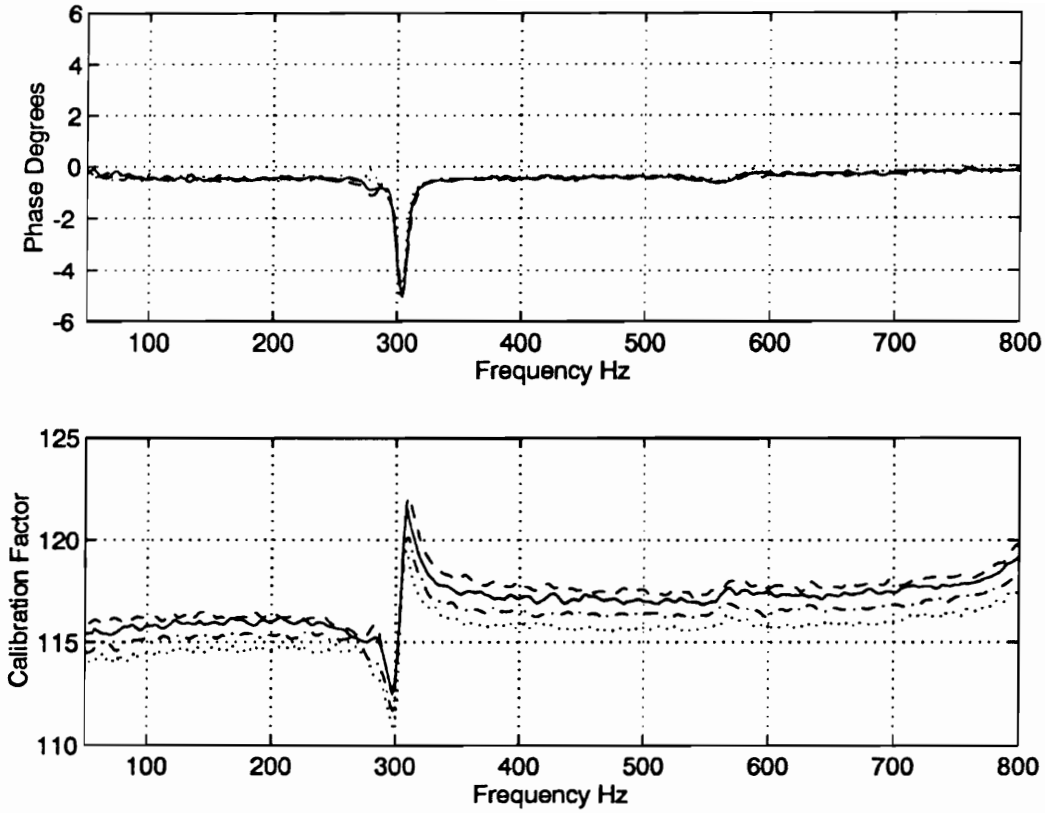

Figure 3.5. Frequency response plot of force gage from the impedance head SN 784 and the reference accelerometer

The fact that the impedance heads used in the data acquisition process are sensitive to torque will increase the uncertainty of the power results discussed Chapter 5. It also adds to the importance of correctly attaching the impedance to the plate with a specified torque.

The accelerometer signal from the impedance heads was calibrated using a piggy back method. In this method the accelerometer to be calibrated is mounted on top of a reference standard accelerometer, which is in turn mounted to an electromagnetic shaker. This setup is shown Fig. 3.6.

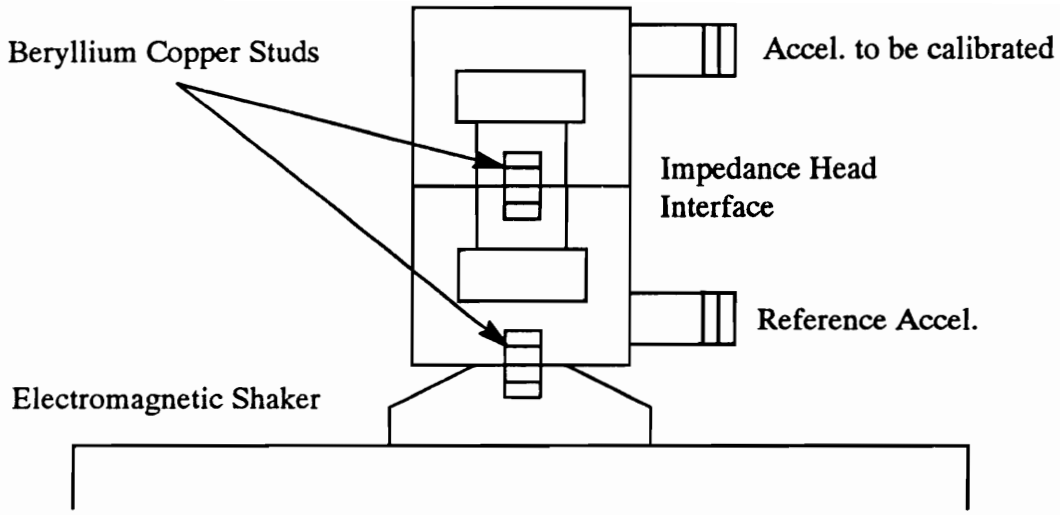

Figure 3.6. Impedance head acceleration calibration setup

The reference accelerometer used to calibrate the accelerometers in the impedance heads was the same reference accelerometer used to calibrate the force gage (i.e. Model 288C01 SN 864). A random signal over the frequency range of 0-1600 Hz was used to determine the calibration factors for the accelerometers. Figure 3.7 illustrates both the phase in degrees and the calibration factor in mv/g for the impedance head model U288C01 SN 708. The phase is 180 degrees which is expected as shown by the setup. At first glance it appears as though the phase is shifting over a large range. However, in reality the phase is simply shifting slightly around 180 degrees. When the phase is 180 degrees or less the plot accurately represents the phase. However, when the phase shifts slightly above 180 degrees it is plotted as slightly less than -180 which causes a large jump in the plot. It was further determined that the accelerometer signal was not affected by torque.

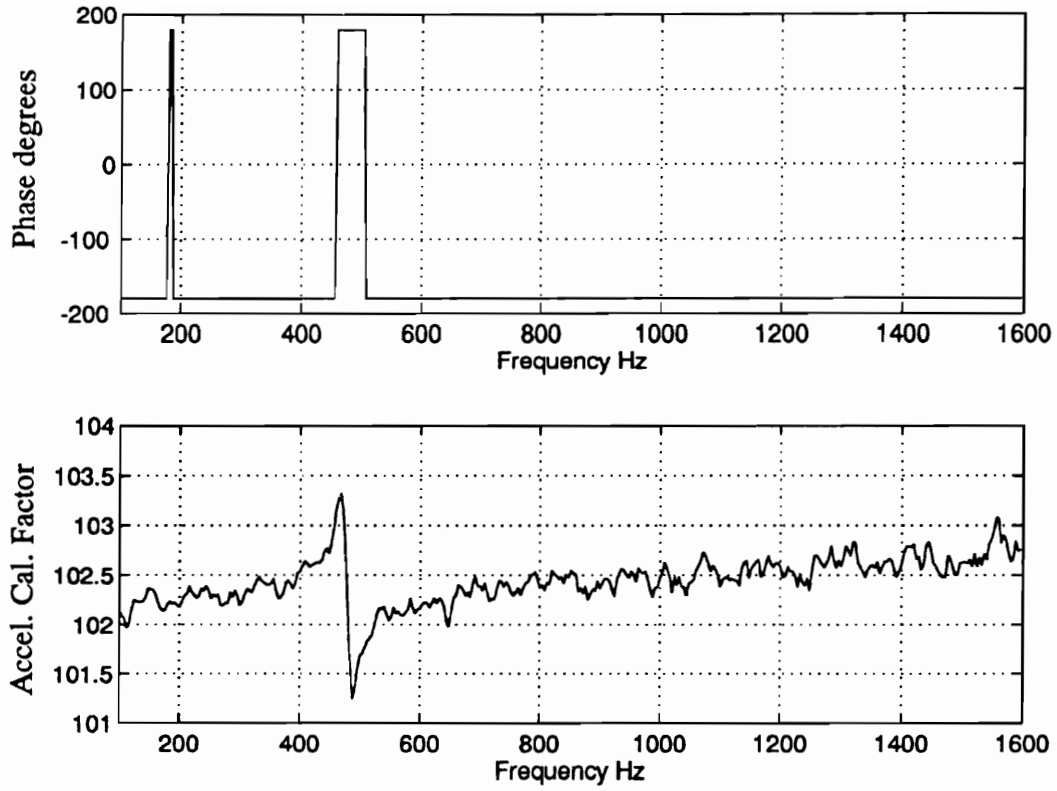

Figure 3.7. Frequency response plot of Accelerometer from the impedance head SN 708 and the reference accelerometer

Figure 3.8 presents the phase and calibration factor results for the impedance head Model U288C01 SN 784. Again, the accelerometer signal from this transducer was shown to be un-affected by the amount of torque with which the gages were connected..

Proper calibration of the impedance heads is vital to the power-method comparison made in Chapter 4. The purpose for presenting this detailed calibration of the impedance heads was to provide some understanding of the uncertainty obtained in the impedance heads alone.

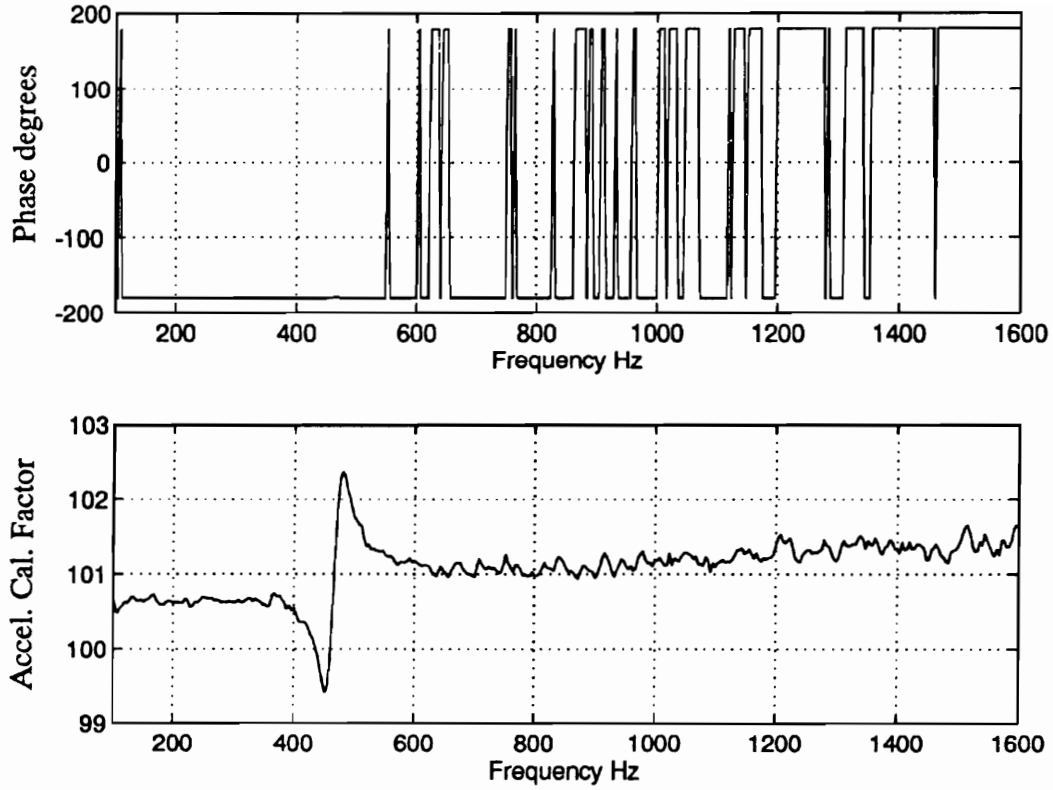

Figure 3.8. Frequency response plot of Accelerometer from the impedance head SN 784 and the reference accelerometer

ICP power supply

The purpose of the Integrated Circuit Piezoelectric (ICP) power supply is to provide constant-current power to the built-in transducer amplifier in ICP transducers. The signal from the transducer is also passed through the ICP power supply. As the signal is passed through the power supply it is possible to create both a magnitude and phase change in the signal. This gives rise to the need of calibrating the ICP power supplies.

The calibration procedure for the ICP power supplies consisted of using a source follower which acted as a simulated transducer. The purpose of the source follower was to absorb the DC voltage sent back from the ICP power supply before it could enter the signal generator. The source follower was first calibrated. This was done by passing a random signal of known

amplitude through the source follower and plotting the frequency response of the source follower output and the original signal. The schematic of this setup is shown in Fig. 3.9.

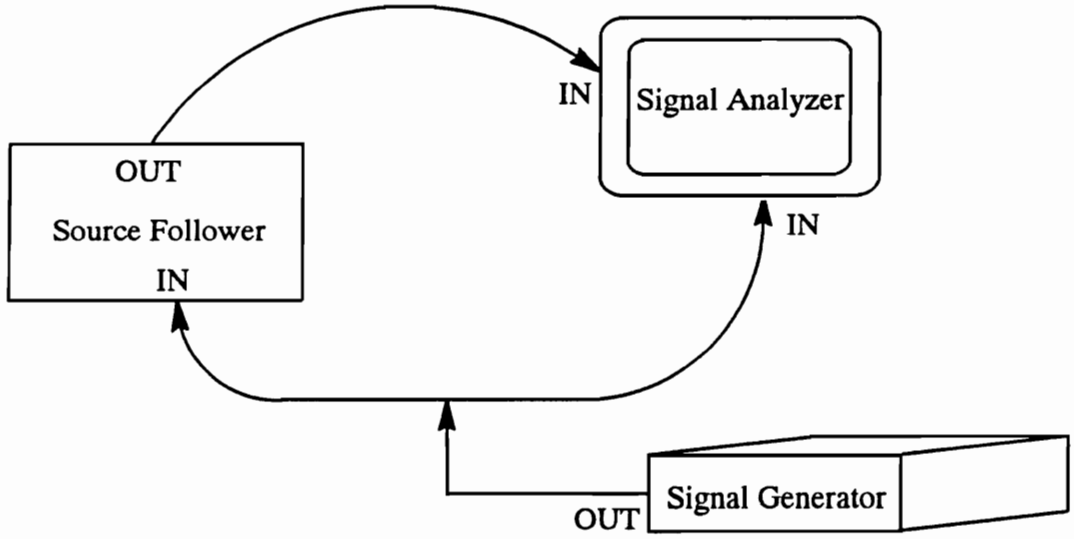

Figure 3.9. Source follower calibration schematic

A frequency range from 0 to 1.6 kHz was used and 100 averages were obtained. The frequency response and phase plots are shown in Fig. 3.10.

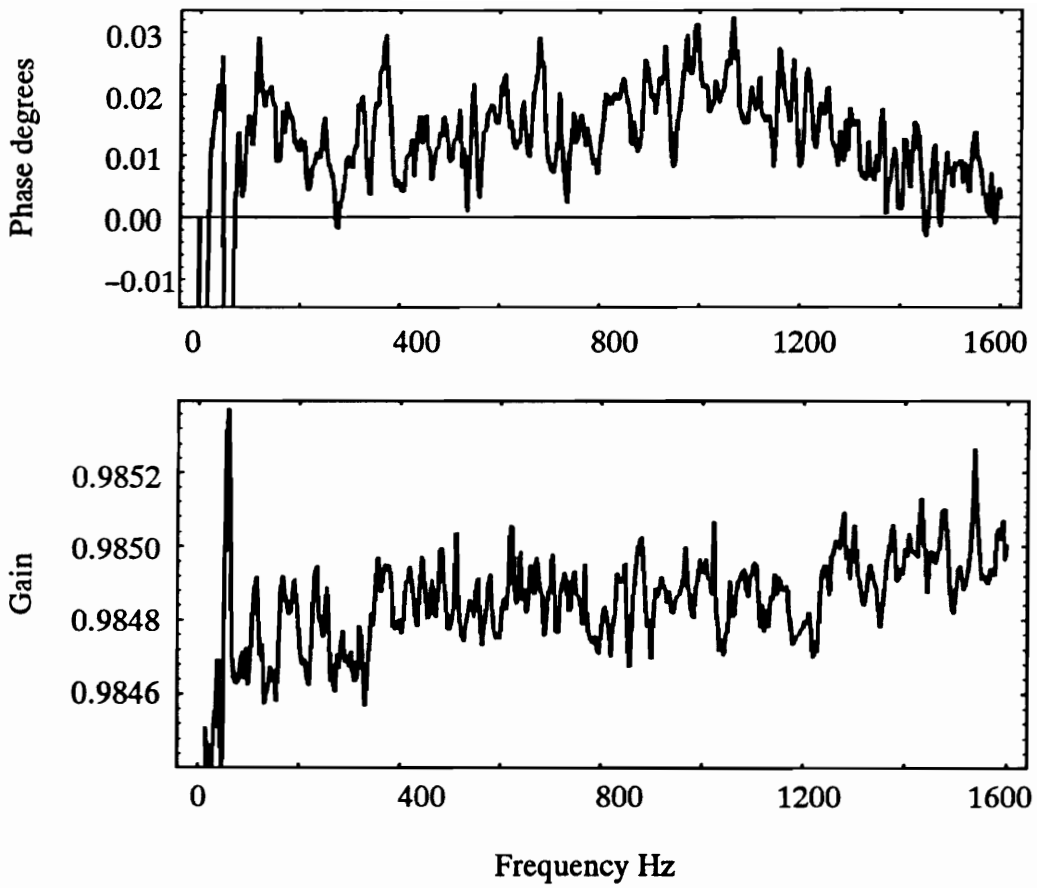

Figure 3.10. Source follower frequency response and calibration constants

The mean magnitude over the frequency range of 20-1600 Hz was 0.9848 with a standard deviation of 1.1047E–04. The mean phase difference was 0.0138 degrees with a standard deviation of 0.0068 degrees.

After calibrating the source follower the ICP power supplies could be calibrated. This procedure was the same as the procedure for calibrating the source follower except now the ICP power supply was included in the loop. The schematic is shown in Fig. 3.11.

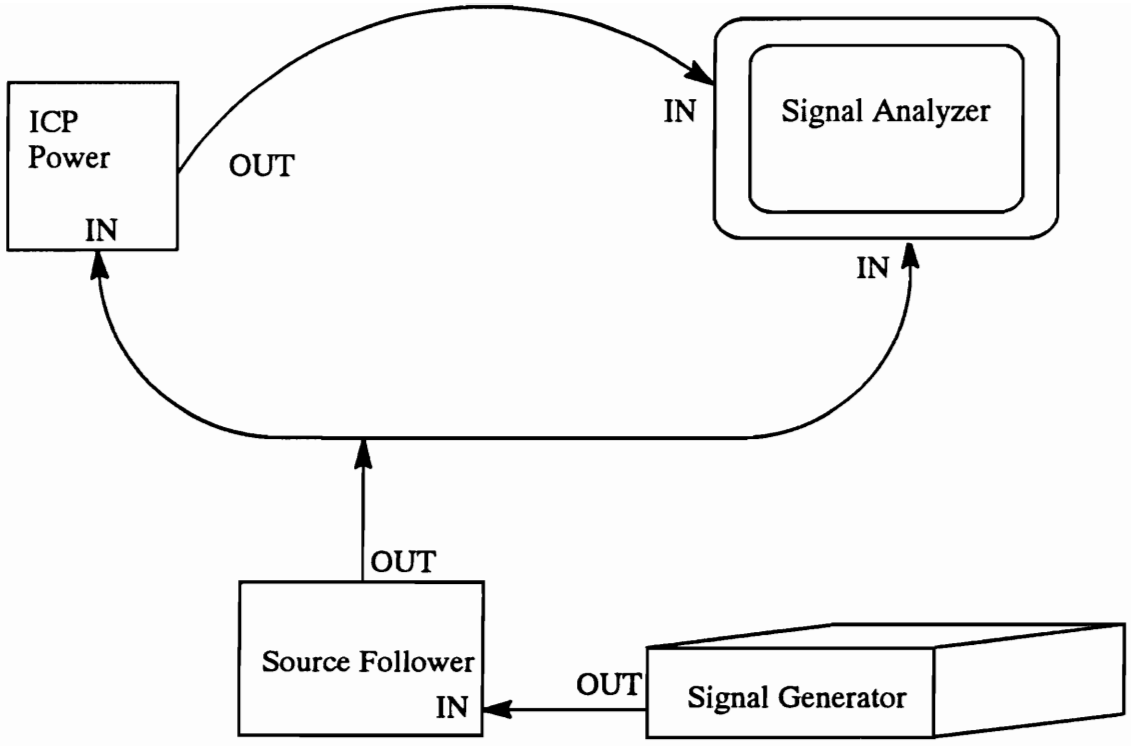

Figure 3.11. ICP power supply calibration schematic

The plots of the frequency response and phase for one of the ICP power supplies is shown in Fig. 3.12.

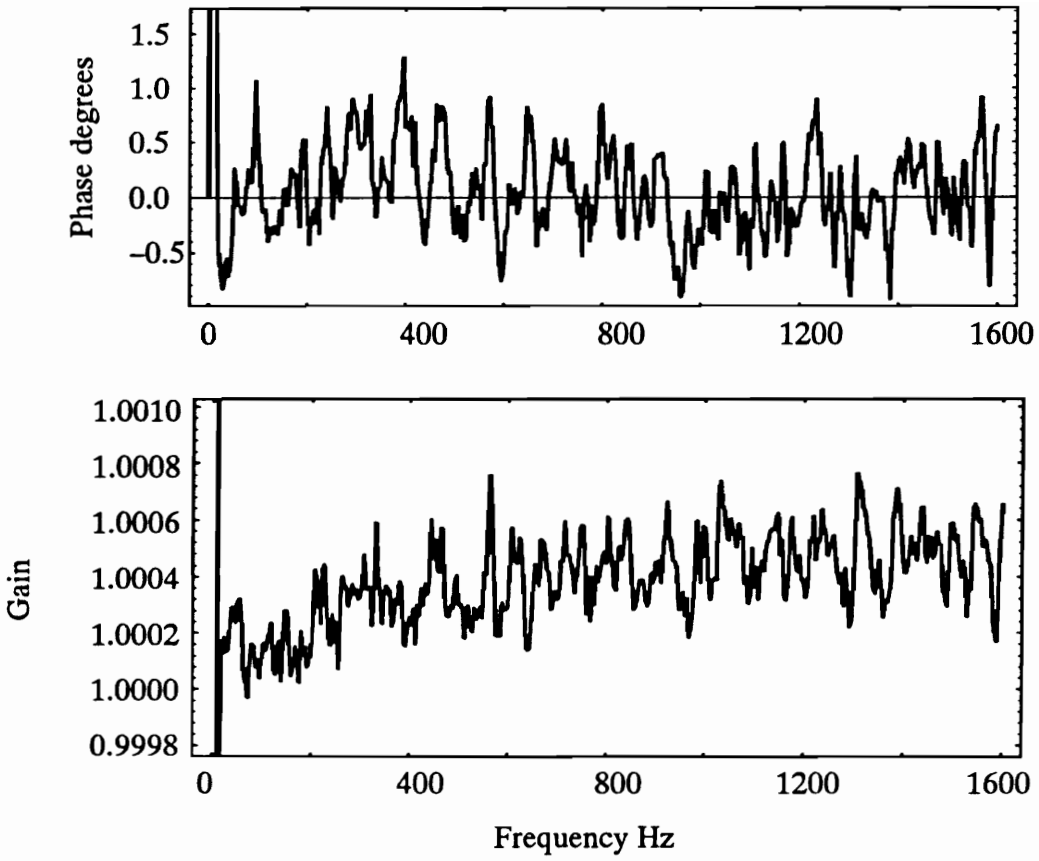

Figure 3.12. Source follower and ICP power supply frequency response and calibration factor

Table 3.1 summarizes the calibration results for the four ICP power supplies used. From these results it can be concluded that the signals are essentially unaffected by the ICP power supplies used in the test setup.

Table 3.1. ICP power supply signal calibration statistics

	ICP BOX 1	ICP BOX 2	ICP BOX 3	ICP BOX 4
Mean Magnitude	1.00073839	1.00101509	1.00112829	1.00092731
Std. of Mag.	0.00083823	0.00743696	0.00925715	0.0083283
Mean Phase	0.00008455	-0.00018397	-0.00021310	0.00011350
Std. Phase	0.00083823	0.00261327	0.00282742	0.00094256

Scanning laser Doppler vibrometer

The SLDV is one of the fundamental components that sets this research apart from current techniques. The SLDV contains a 1 mW Helium-Neon (He-Ne) laser theoretically capable of extracting velocities in the range of 0 to + or – 1000 mm/s. Scanning mirrors, which permit controlled deflection of the laser beam allow the entire test surface to be scanned without moving the laser base or the test structure. The scanning capability of the SLDV allows spatially dense non-contacting measurement of the velocity field over the structure. A photograph of the Ometron SLDV used in this research is shown in Fig. 3.13.

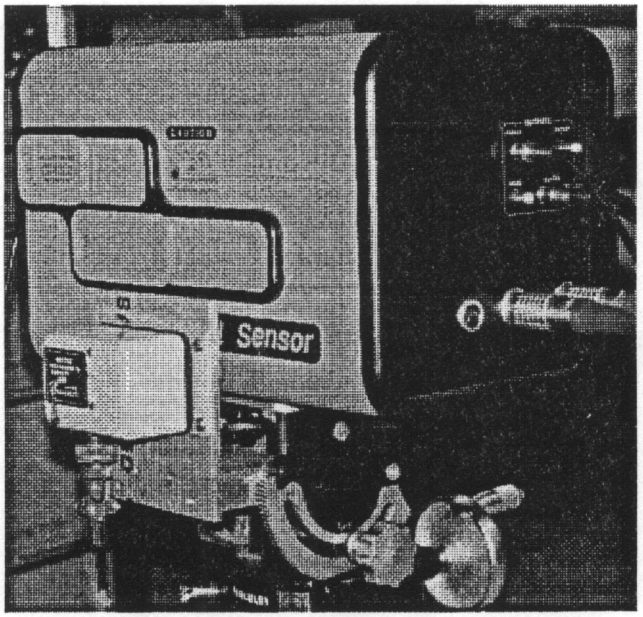

Figure 3.13. SLDV with linear transducer

The velocity measurement principle of the SLDV is based on the well known Doppler shift. The frequency shift due to a moving object is clearly illustrated in sound waves by the passing of a train or an automobile with a siren. This same frequency shift occurs in a beam of light which has been reflected from a moving structure. The shift in the frequency of the light beam is proportional to the surface velocity of the vibrating structure [42]. A more detailed description of the SLDV is provided in appendix A.

The calibration of the SLDV was performed by Ometron Inc. and verified by Galaitsis [43]. Table 3.2 lists the calibration constants used in this dissertation. These are the values given by Ometron Inc. and compared closely to the calibration obtained by Galaitsis.

Table 3.2. Laser calibration factors

Low Range	300 mv/(mm/s)
Medium Range	30.0 mv/(mm/s)
High Range	3.00 mv/(mm/s)

Filter, A/D, and computer loop - electrical calibration

The last calibration task consists of calibrating the complete loop of the filters, A/D, and the computer. This calibration is performed after the forcing frequencies and magnitudes, the filter gains and cutoff frequencies, and the laser range have been selected.

The process is performed by first suppling a zero volt signal at a zero frequency to the filter, A/D, and computer loop and calibrating the offset. Under these conditions the software calibration factors should be set such that the offset values computed by the signal processing are zero. The next step is to provide a known harmonic signal to the loop and again adjust the software data acquisition calibration factors such that the signal processing software computes the correct known signal magnitude. This calibration step is very important and should be performed just before the actual testing is to be performed.

3.2.4 Signal Processing

The velocity signal from the SLDV and the signals from the impedance heads are acquired using an analog-to-digital (A/D) converter. Some error is initiated during the A/D conversion. The maximum error should be less than 1 DAC step or 1/2 DAC step if rounding is used. For this reason it is important to optimize the dynamic range of the A/D board.

The current research focus has dealt with single frequency sine-dwell excitation. The time signal model used to approximate this type of excitation is shown in Eq. (3.4). Equation (3.4) can be rewritten in terms of an offset β_0, real β_1, and imaginary β_2, coefficients as shown by Eq. (3.5) where β_1 and β_2 are given by Eqs. (3.6).

$$Y(\omega t) = \beta + \alpha(\omega t - \phi) \tag{3.4}$$

$$Y(\omega t) = \beta_0 + \beta_1 \cos(\omega t) + \beta_2 \sin(\omega t) \tag{3.5}$$

$$\beta_1 = \alpha \cos(\phi) \qquad \beta_2 = \alpha \sin(\phi) \tag{3.6}$$

A multiple linear regression technique is used to solve for the offset, real, and imaginary coefficients as discussed by Montgomery [2]. It should be further noted that the variance between the time signal model and the actual data is used to weight the velocity-field solution as discussed in the next section.

Summary

The purpose of this section was to present testing methods which will improve the quality of the data acquired by the SLDV and to present and discuss the calibration procedures and results used in this dissertation. The techniques presented and the results obtained provide an understanding of the difficulties in the calibration techniques and the possibilities for variation in the results. These results will provide significant insight to the comparison of different power methods presented in Chapter 5.

3.3 Velocity-Field Representation

Nomenclature

$b()$	B-spline basis functions
e	velocity error in finite element model

$F()$	force
$f()$	force amplitude (spatial component)
$\vec{f}_D(\omega)$	effective dynamic force vector
h	thickness
J	Jacobian matrix
$K_D(\omega)$	effective dynamic stiffness matrix
m	total number of nodes in the finite element mesh
$\hat{m}$	number of nodes in a single finite element
$N(\xi, \eta, \zeta)$	3-D basis functions
n	total number of samples
$\hat{n}$	number of samples in a single finite element
P	projection of vector a into vector b
Q	B-spline curve
q	distributed force
q	power component
SSE	sum of squares for error
s_e^2	estimated error variance
s_e	estimated standard deviation
t	time
$V()$	velocity
$\mathcal{V}$	finite element nodal velocity value (model parameter)
$v()$	velocity amplitude (spatial component)
$\vec{v}$	modeled velocity vector
$\hat{v}_L$	signed velocity value measured by laser
$\vec{v}_L$	velocity vector measured by laser

x, y, z	spatial Cartesian variables
ξ, η, ς	parametric variables
Π	variational operator
ϕ	phase angle
$\vec{\psi}$	direction cosine vector
ω	driving frequency

Subscript

i, j, k, l	general indices
L	component along laser line-of-sight
x, y, z	spatial components
ξ, η	parametric components

3.3.1 Introduction

This section provides an overview of the Experimental Spatial Dynamics Modeling (ESDM) technique which is used to solve for the 3-D continuous complex-valued velocity field from the laser data. The ESDM technique is a two step process mainly developed by Montgomery [2]. The first step consists of a laser registration process in which the position and orientation of the laser relative to the structure are determined. The second step consists of solving for the velocity field from the raw laser data. This section provides a brief overview of these two processes.

3.3.2 Laser Registration

As previously mentioned, the laser measures the velocity along the line-of-sight of the laser beam. In order to group all the laser measurements together and solve for the velocity field, the position and orientation from which the laser measurements were made must be determined. The process of determining the position and orientation of the laser is known as laser registration.

Over the past few years, several laser registration techniques have been developed. Zeng et al. [44] formulated a four-point algorithm which performs an iterative search for the laser-to-structure coordinates transformation matrix by solving for the four unknown ranges to the given registration points. Montgomery [2] developed a multiple point indirect registration algorithm which uses the laser beam deflection angles to the structures known registration points for computing the structure-to-laser transformation matrix. This method involves minimizing three nonlinear equations using a least squares minimization technique. Lindholm, [45] developed another registration algorithm based on a minimization of the differences between the measured laser beam angles and the computed angles. This method is based solely on the scan angles used to hit the registration points on the structure where the previous method by Zeng used estimated ranges. In all three registration techniques at least three registration points for which the distances are accurately known in the same coordinate system are required.

In general, these three registration techniques produce the same results. The key factors in high quality registration are not necessarily which registration algorithm is used but instead the accuracy of the experimental data used in solving for the position and orientation of the laser.

3.3.3 Velocity-Field Solution

The continuous 3-D complex-valued velocity representation of the true structure velocity used in the ESPF method is solved for using an Experimental Spatial Dynamics Modeling (ESDM) technique. In its simplest definition, the ESDM method provides a surface fit of the velocity data acquired by the SLDV. The ESDM method is based on a least squares collocation (LSC) method also known as point least squares and overdetermined collocation [46].

The LSC method is a weak form of stating the governing differential equations. In general, this method consists of minimizing the squared residuals between the known solution and

an approximated model of the solution. Typically, the approximated model satisfies essential boundary conditions and contains unknown coefficients. In the LSC method it is these unknown coefficients which are solved for by minimizing the squared residuals between the true model and the approximate model. In the ESDM approach, the true model is taken as the magnitude of the raw laser measurements, $\hat{v}_L$, and is not known in functional form. The approximated model is given by Eq. (3.7) which represents a 3-D complex-valued harmonic velocity field under steady-state conditions.

$$\vec{V}(x, y, z, \omega, \phi, t) = \vec{v}(x, y, z, \omega)\cos(\omega t - \phi) \tag{3.7}$$

This equation can be rewritten in terms of real and imaginary coefficients as shown by Eqs. (3.8), (3.9), and (3.10). The coefficients given in Eqs. (3.9) and (3.10) are solved for using a single frequency least squares formulation as discussed in the previous section.

$$\vec{V}(x, y, z, \omega, \phi, t) = \vec{v}_{RE}(x, y, z, \omega)\cos(\omega t) + \vec{v}_{IM}(x, y, z, \omega)\sin(\omega t) \tag{3.8}$$

$$\vec{v}_{RE}(x, y, z, \omega) = \vec{v}(x, y, z, \omega)\cos(\phi) \tag{3.9}$$

$$\vec{v}_{IM}(x, y, z, \omega) = \vec{v}(x, y, z, \omega)\sin(\phi) \tag{3.10}$$

The error statement used in the least squares approach from which the residuals between the two models are computed is developed by taking the difference between the true structure velocity vector at the point the laser beam hits the structure projected into the direction of the laser measurement and the velocity vector measured by the SLDV. The projection P of vector a in the direction of vector b is defined by Eq. (3.11) where $a \cdot b$ is the dot product of vectors a and b and $\| b \|$ is the magnitude of vector b [47].

$$P = \frac{a \cdot b}{\| b \|} \tag{3.11}$$

In theory, the projection of the true structure velocity into the direction of the velocity measured by the SLDV, and the velocity measured by the SLDV should be equal. Hence,

using Eq. (3.11) to represent the projection of the true structure velocity in the direction of the laser measurement and setting this equal to the velocity measured by the SLDV results in Eq. (3.12).

$$\hat{v}_L = \frac{\vec{v} \cdot \vec{v}_L}{\| \vec{v}_L \|} \tag{3.12}$$

Expanding Eq. (3.12) into 3-D components results in Eq. (3.13). Equation (3.13) is the basic equation which sets the true model and the approximated model equal. In this equation, $\hat{v}_L$, is a scalar value, v_x, v_y, and v_z represent the undetermined components of the structure's velocity field in the approximate model, and $\frac{v_{Lx}}{\| \vec{v}_L \|}$, $\frac{v_{Ly}}{\| \vec{v}_L \|}$, and $\frac{v_{Lz}}{\| \vec{v}_L \|}$ represent the direction cosines of the laser beam projected into the structures x, y, z coordinate system. The direction cosines are the cosines of the angles between the true structure velocity vector and the velocity vector measured by the SLDV. These values were determined from the laser registration process previously discussed.

$$\hat{v}_L = \frac{v_x v_{Lx}}{\|\vec{v}_L\|} + \frac{v_y v_{Ly}}{\|\vec{v}_L\|} + \frac{v_z v_{Lz}}{\|\vec{v}_L\|} \tag{3.13}$$

Using ψ_{Lx}, ψ_{Ly}, and ψ_{Lz} to represent the direction cosines, Eq. (3.13) can be rewritten in a more simple notation as shown by Eq. (3.14).

$$v_x \psi_{Lx} + v_y \psi_{Ly} + v_z \psi_{Lz} = \hat{v}_L \tag{3.14}$$

In the ESDM method, the squared residual equation or the least squares statement used to solve for the velocity coefficients in Eq. (3.14) is derived by setting Eq. (3.14) equal to zero, squaring it, and weighting the entire equation by the estimated error variance as shown by Eq. (3.15). At this point the functional or least squares variational statement relates the continuous velocity field components to laser measurements. To solve for these velocity field components a finite element formulation will be used. The subscript i in Eq. (3.15) represents the laser sample number.

$$\Pi = SSE = \sum e_i^2/s_{ei}^2 = \sum\left(v_{xi}\psi_{Lxi} + v_{yi}\psi_{Lyi} + v_{zi}\psi_{Lzi} - \hat{v}_{Li}\right)^2/s_{ei}^2 \quad (3.15)$$

Before solving for the unknown functions v_{xi}, v_{yi} and v_{zi} in Eq. (3.15), these components will be defined in terms of basis functions $N_j(\xi, \eta, \zeta)$ and nodal velocities $\mathcal{V}$. Rewriting the unknown coefficients in this form results in Eqs. (3.16) where $\hat{m}$ represents the number of nodes or control points ($\mathcal{V}_{xj}$, $\mathcal{V}_{yj}$, and $\mathcal{V}_{zj}$) used to define each element.

$$\begin{aligned} v_{xi} &= v_x(\xi_i, \eta_i, \zeta_i) = \sum_{j=1}^{\hat{m}} N_j(\xi_i, \eta_i, \zeta_i)\mathcal{V}_{xj} \\ v_{yi} &= v_y(\xi_i, \eta_i, \zeta_i) = \sum_{j=1}^{\hat{m}} N_j(\xi_i, \eta_i, \zeta_i)\mathcal{V}_{yj} \\ v_{zi} &= v_z(\xi_i, \eta_i, \zeta_i) = \sum_{j=1}^{\hat{m}} N_j(\xi_i, \eta_i, \zeta_i)\mathcal{V}_{zj} \end{aligned} \quad (3.16)$$

The control points which are used to define the velocity field are then solved for by requiring stationarity of the variational statement which results in minimizing the error between the laser measurements and the model of the velocity field. This is done by taking the partial derivatives of Eqs. (3.16) and setting them equal to zero as shown by Eqs. (3.17). The residual or error equation , e, is shown in Eq. (3.18). Equation (3.19) shows the expansion of the partial derivative with respect to $\mathcal{V}_{xk}$. After all the partial derivatives are defined for an element, the resulting set of equations can be assembled by the direct stiffness method into the "effective" dynamic stiffness matrix, the nodal velocity vector, and the "effective" nodal force vector as shown by Eq. (3.20) where the notation $N_{ji} = N_{ji}(\xi, \eta, \zeta)$ has been used to simplify the expressions. It is important to note that Eq. (3.20) has the same form as the direct dynamic stiffness formulation shown by Eq. (3.21).

$$\frac{\partial \Pi}{\partial \mathcal{V}_{xk}} = 2\sum_{i=1}^{\hat{n}} e_i N_k(\xi_i, \eta_i, \zeta_i)\psi_{Lxi}/s_{ei}^2 = 0$$

$$\frac{\partial \Pi}{\partial \mathcal{V}_{yk}} = 2\sum_{i=1}^{\hat{n}} e_i N_k(\xi_i, \eta_i, \zeta_i)\psi_{Lyi}/s_{ei}^2 = 0 \tag{3.17}$$

$$\frac{\partial \Pi}{\partial \mathcal{V}_{zk}} = 2\sum_{i=1}^{\hat{n}} e_i N_k(\xi_i, \eta_i, \zeta_i)\psi_{Lzi}/s_{ei}^2 = 0$$

$$e_i = \sum_{j=1}^{\hat{m}} \left(N_j(\xi_i, \eta_i, \zeta_i)\left(\mathcal{V}_{xj}\psi_{Lxi} + \mathcal{V}_{yj}\psi_{Lyi} + \mathcal{V}_{zj}\psi_{Lzi}\right) - \hat{v}_{Li} \right) \tag{3.18}$$

$$\frac{\partial \Pi}{\partial \mathcal{V}_{xk}} = 0 =$$

$$\sum_{i=1}^{\hat{n}} \left[\sum_{j=1}^{\hat{m}} N_j(\xi_i, \eta_i, \zeta_i)\left(\mathcal{V}_{xj}\psi_{Lxi} + \mathcal{V}_{yj}\psi_{Lyi} + \mathcal{V}_{zj}\psi_{Lzi}\right) - \hat{v}_{Li} \right] N_k(\xi_i, \eta_i, \zeta_i)\psi_{Lxi}/s_{ei}^2 \tag{3.19}$$

$$\sum_{i=1}^{\hat{n}} \begin{bmatrix} N_{1i}N_{1i}\psi_{Lxi}\psi_{Lxi} & N_{1i}N_{1i}\psi_{Lxi}\psi_{Lyi} & \cdots & N_{1i}N_{\hat{m}i}\psi_{Lxi}\psi_{Lzi} \\ & N_{1i}N_{1i}\psi_{Lyi}\psi_{Lyi} & \cdots & N_{1i}N_{\hat{m}i}\psi_{Lyi}\psi_{Lzi} \\ & & \cdots & N_{1i}N_{\hat{m}i}\psi_{Lzi}\psi_{Lzi} \\ & & \ddots & \vdots \\ \text{symmetric} & & & N_{\hat{m}i}N_{\hat{m}i}\psi_{Lzi}\psi_{Lzi} \end{bmatrix} \begin{Bmatrix} \mathcal{V}_{x1} \\ \mathcal{V}_{y1} \\ \mathcal{V}_{z1} \\ \vdots \\ \mathcal{V}_{z\hat{m}} \end{Bmatrix} \left(\frac{1}{s_{ei}^2}\right) =$$

$$\sum_{i=1}^{\hat{n}} \begin{Bmatrix} N_{1i}\psi_{Lxi}\hat{v}_{Li} \\ N_{1i}\psi_{Lyi}\hat{v}_{Li} \\ N_{1i}\psi_{Lzi}\hat{v}_{Li} \\ \vdots \\ N_{\hat{m}i}\psi_{Lzi}\hat{v}_{Li} \end{Bmatrix} \left(\frac{1}{s_{ei}^2}\right) \tag{3.20}$$

$$K_D(\omega)\vec{\mathcal{V}} = \vec{f}_D(\omega) \tag{3.21}$$

The continuity of the velocity field is dependent upon the element type. A field has C^n continuity if the derivatives of the field through order n are continuous. To compute a spatially continuous model of the power over the structure at least C^3 continuity is required in the velocity-field representation. This continuity requirement is determined by the derivatives

required to compute the shear forces in the power equations. The next section presents the development of the quintic B-spline basis functions which were developed as part of this research to provide a continuous representation of the power over the structure.

3.3.4 Quintic B-spline Representation of the Velocity Field

This section presents the development of the uniform bi-quintic B-spline elements which are used to represent the velocity as well as the power across the structure in the ESPF method. First, the general theory of B-splines as well as the derivation of the uniform quintic basis functions for a single element will be presented. The formulation of a uniform bi-quintic B-spline surface will then be discussed. A similar development for cubic B-splines was presented by Bartels et al. [48].

General B-spline theory

A B-spline curve is constructed by a linear combination of polynomial segments or basis functions defined in uniform parametric space from 0 to 1. The basis functions are derived such that continuity through each individual segment of the curve and continuity between the curves is guaranteed.

The order m of the basis functions determines the order of continuity of the curve. m + 1 basis functions of order m are required to have C^m continuity at the knots. Knots are the parametric values at which the B-spline segments are joined. The "uniform," qualification on the basis functions implies that the basis functions are derived for knots that are uniformly spaced. Seven knots are required for each cubic B-spline segment and 12 knots are required for each quintic B-spline segment. Control points are weighting coefficients on the B-spline basis functions much like the nodal coordinates in a conventional finite element model. m + 1 control points are required to define a segment of the curve. The control points define the curve and allow for local control. The control points are not the velocity values at the

knots and they have no real physical significance. They are simply weighting coefficients to the B-spline shape functions. Local control implies that by altering the position of a single control point causes only a part of the curve to change. The entire B-spline curve is expressed as a linear combination of the control points, V_i, and basis functions, b_i, as shown by Eq. (3.22) . Equation (3.22) can also be thought of as a weighted sum of the control vertices.

$$Q(\xi) = \sum_{i=1}^{m+1} V_i \, b_i(\xi) \tag{3.22}$$

As previously mentioned, third-order spatial derivatives of the displacement field are required to represent the shear forces and, hence, compute the power in the ESPF method. Coefficients for quintic B-spline basis functions were derived from this continuity requirement. Quintic B-splines provide quadratic representation (C^2 continuity) of the shear forces used to compute the power.

For a fifth-order B-spline curve, 12 knots, 6 control points, and six, fifth-order basis functions are required. The relationships between the knots, control points, and the defined section of the curve are shown in Fig. 3.14. The defined section of the curve is the sum of all 6 curves between control points 3 and 4.

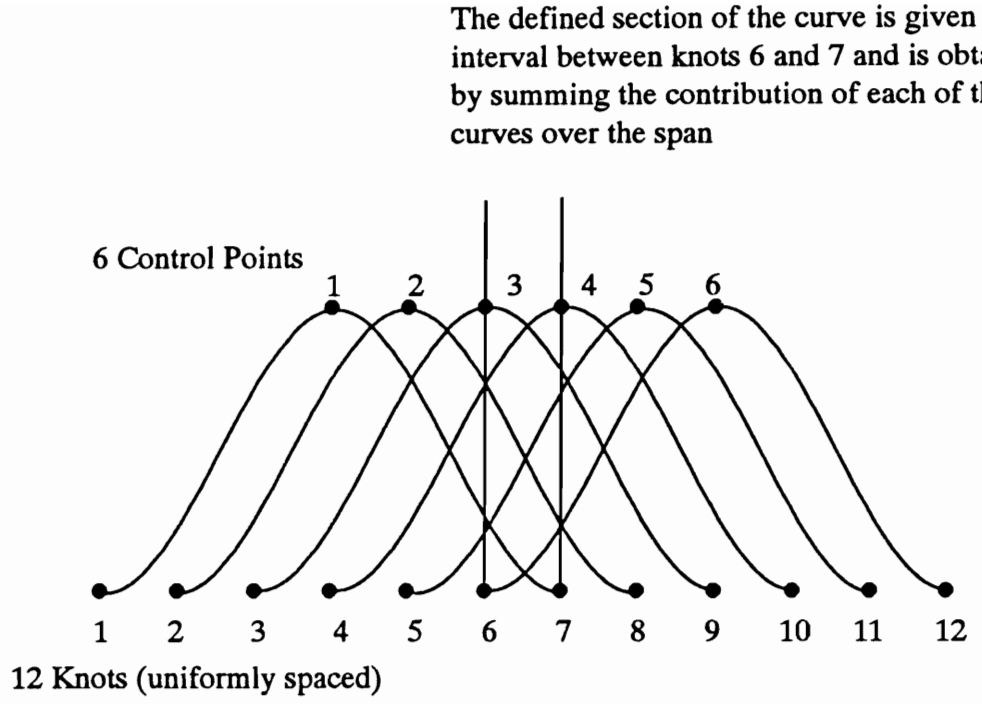

Figure 3.14. Relationship between knots, control points, and the defined section of the curve for a single uniform quintic B-spline curve

Since the basis functions are fifth order, 36 unknown coefficients must be determined. These coefficients are computed by making the following constraints where $b_n(\xi)$ represents the n^{th} polynomial evaluated at the parametric coordinate (ξ). The end conditions $b_1(0)$, and $b_6(1)$ along with the first, second, third, and fourth derivatives at these locations are zero. These constraints provide 10 of the 36 required equations. It is also required that the same fourth-order continuity exists at the five interior knots which results in 25 more equations. The final equation required to compute the unknown coefficients states that at any point on the surface, the sum of the basis functions must equal one. This condition is mathematically expressed by Eq. (3.23).

$$b_1(\xi) + b_2(\xi) + b_3(\xi) + b_4(\xi) + b_5(\xi) + b_6(\xi) = 1 \qquad (3.23)$$

The results of solving these 36 equations for the 36 coefficients of the basis functions are shown by Eq. (3.24).

$$\left[b_1,\ b_2,\ b_3,\ b_4,\ b_4,\ b_5,\ b_6\right] = \left[\xi^5,\ \xi^4,\ \xi^3,\ \xi^2,\ \xi,\ 1\right]$$

$$\begin{bmatrix} 1/120 & 0 & 0 & 0 & 0 & 0 \\ -1/24 & 1/24 & 1/12 & 1/12 & 1/24 & 1/120 \\ 1/12 & -1/6 & -1/6 & 1/6 & 5/12 & 13/60 \\ -1/12 & 1/4 & 0 & -1/2 & 0 & 11/20 \\ 1/24 & -1/6 & 1/6 & 1/6 & -5/12 & 13/60 \\ -1/120 & 1/24 & -1/12 & 1/12 & -1/24 & 1/120 \end{bmatrix} \tag{3.24}$$

Equations (3.24), are the basis functions for a fifth-order B-spline curve. Substituting these expressions into Eq. (3.22), the curve defined by the control points is represented.

B-spline surface elements

A B-spline surface is constructed in a piecewise manner by polynomial segments which make up elements of the surface in the same manner that a B-spline curve is developed. B-spline elements are defined in a uniform parametric space from 0 to 1 in (ξ, η) coordinates by the same set of basis functions as shown by Eq. (3.24).

Formally, B-spline surfaces are called tensor product surfaces formed from the tensor product of the B-spline basis functions as shown in Eq. (3.25). Equation (3.25) represents the mathematical formulation for a B-spline surface element representation of the transverse velocity, $V_{ij}(\xi, \eta)$, over the ij^{th} element. In Eq. (3.25), b_r and b_s represent the B-spline basis functions of polynomial order $(m - 1)$. The array of control points describing the B-spline element are $V_{i+r,j+s}$ which form a two dimensional $(m \times m)$ array of control points. In this application of B-spline elements, the control points are solved for as the nodal velocities in the ESDM solution of the velocity field.

$$V_{ij}(\xi, \eta) = \sum_{r=1}^{m} \sum_{s=1}^{m} b_r(\xi)\, b_s(\eta)\, V_{i+r,j+s} \tag{3.25}$$

The entire velocity field over the structure is represented by a mesh of B-spline elements which are connected continuously up through the desired spatial continuity. Figure 3.15 il-

lustrates a single quintic B-spline surface element with 36 control points and a 2x2 element mesh illustrating the inter-element continuity. It is important to note that the uniformly spaced knots are not shown in Fig. 3.15. Only the control points which are used to define the curve are shown. The shaded region represents the area over which the surface is defined for the given element.

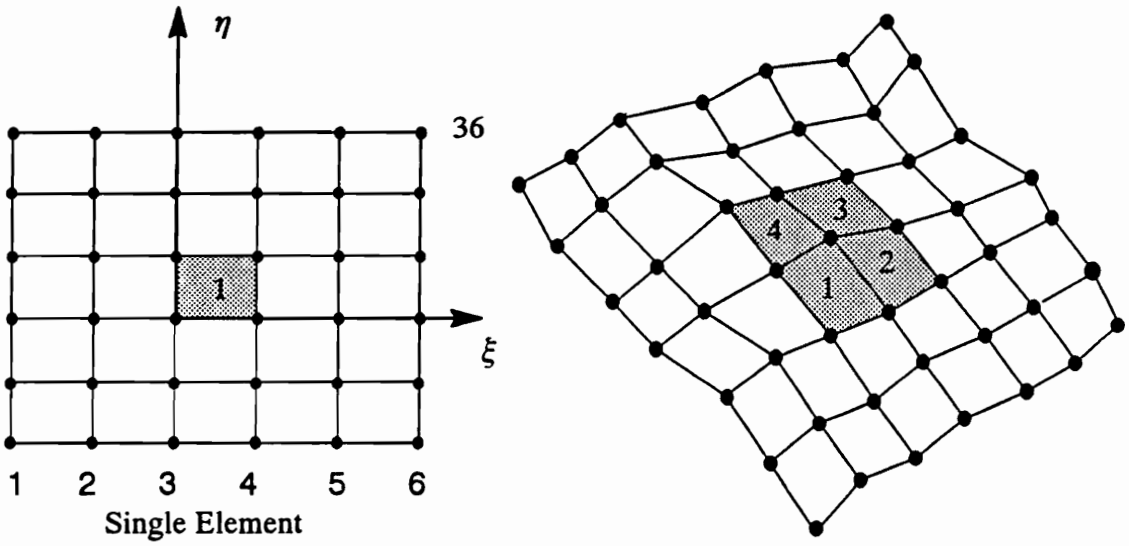

Figure 3.15. B-spline surface representation

Jacobian matrix development

Structural power is computed from the generalized forces and velocities in vibrating structures. The generalized forces are computed from derivatives of the displacement field with respect to the model space coordinates (x, y). The B-spline representation expresses the displacements in terms of the parametric coordinates (ξ, η). Therefore, the Jacobian matrix relating spatial derivatives of the displacement field between the model space, (x, y), and parametric space, (ξ, η), must be developed.

In order to obtain the required third derivatives and all the corresponding cross derivatives, a 2-D element, such as a flat plate, requires that the 9×9 Jacobian matrix shown in Eq. (3.26) be computed and inverted. In Eq. (3.26) the nomenclature is such that x_ξ^3 represents the partial derivative of x with respect to ξ raised to the third power. Similarly, $3x_\xi x_{\xi\xi}$ implies three multiplied by the first partial derivative of x with respect to ξ multiplied by the second partial of x with to ξ squared.

$$J = \begin{bmatrix} x_\xi^3 & 3y_\xi x_\xi^2 & 3x_\xi x_{\xi\xi} & 3y_\xi^2 x_\xi & 3y_{\xi\xi}x_\xi + 3y_\xi x_{\xi\xi} & x_{\xi\xi\xi} & y_\xi^3 & 3y_\xi y_{\xi\xi} & y_{\xi\xi\xi} \\ & & & & & x_\xi & & & y_\xi \\ & & & & & x_\eta & & & y_\eta \\ x_\eta x_\xi^2 & 2y_\xi x_\eta x_\xi + y_\eta x_\xi^2 & 2x_{\eta\xi}x_\xi + x_\eta x_{\xi\xi} & 2y_\eta y_\xi x_\xi + y_\xi^2 x_\eta & 2y_{\eta\xi}x_\xi + y_{,\eta}x_{\xi\xi} + 2y_\xi x_{\eta\xi} + y_{\xi\xi}x_\eta & x_{\eta\xi\xi} & y_\eta y_\xi^2 & 2y_{\eta\xi}y_\xi + y_\eta y_{\xi\xi} & y_{\eta\xi\xi} \\ & & x_\xi^2 & & 2y_\xi x_\xi & x_{\xi\xi} & & y_\xi^2 & y_{\xi\xi} \\ x_\eta^2 x_\xi & 2y_\eta x_\eta x_\xi + y_\xi x_\eta^2 & 2x_{\eta\xi}x_\eta + x_{\eta\eta}x_\xi & 2y_\eta y_\xi x_\eta + y_\eta^2 x_\xi & 2y_{\eta\xi}x_\eta + y_\xi x_{\eta\eta} + 2y_\eta x_{\eta\xi} + y_{\eta\eta}x_\xi & x_{\eta\eta\xi} & y_\eta^2 y_\xi & 2y_{\eta\xi}y_\eta + y_{\eta\eta}y_\eta & y_{\eta\eta\xi} \\ & & x_\eta x_\xi & & y_\eta x_\xi + y_\xi x_\eta & x_{\eta\xi} & & y_\eta y_\xi & y_{\eta\xi} \\ x_\eta^3 & 3y_\eta x_\eta^2 & 3x_\eta x_{\eta\eta} & 3x_\eta x_{\eta\eta} & 3y_{\eta\eta}x_\eta + 3y_\eta x_{\eta\eta} & x_{\eta\eta\eta} & y_\eta^3 & 3y_{\eta\eta}y_\eta & y_{\eta\eta\eta} \\ & & x_\eta^2 & & 2y_\eta x_\eta & x_{\eta\eta} & & y_\eta^2 & y_{\eta\eta} \end{bmatrix} \tag{3.26}$$

In an arbitrary 3-D shell element a 19×19 Jacobian matrix is required. By inverting the Jacobian matrix the spatial derivatives of the displacement field in (x, y) space are obtained and all the generalized force terms in the power-flow equations can be determined.

It should be noted that in the case of a flat plate, described by elements using uniform knot spacing in the B-spline mesh, the Jacobian matrix given by Eq. (3.26) can be diagonalized as shown by Eq. (3.27). This diagonalization occurs for two reasons. The first is that all derivatives higher than first order are zero since the derivative of a constant is zero. The second is that all derivatives of a given direction with respect to the perpendicular parametric direction are zero because the axes are perpendicular, (i.e. the parametric coordinate system is aligned with the structural coordinate system).

$$J = \begin{bmatrix} x_\xi^3 & & & & & & & & \\ & x_\xi^2 & & & & & & & \\ & & x_\xi & & & & & & \\ & & & y_\eta^3 & & & & & \\ & & & & y_\eta^2 & & & & \\ & & & & & y_\eta & & & \\ & & & & & & [y_\eta]^2 x_\xi & & \\ & & & & & & & y_\eta [x_\xi]^2 & \\ & & & & & & & & y_\eta x_\xi \end{bmatrix} \tag{3.27}$$

It can further be state that the diagonalization is due to the fact that the model space (x, y) and the parametric space (ξ, η) are parallel. For shells of revolution, such as cylinders, the Jacobian matrix can also be reduced by using the appropriate coordinate system. However, for shells of arbitrary geometry the 19×19 Jacobian matrix cannot be reduced which significantly increases the computation time.

After the Jacobian matrix has been computed the derivative components are then obtained as shown by Eq. (3.28) where ϕ represents the field variable of interest. In this case ϕ would represent either the displacement or velocity fields.

$$\begin{Bmatrix} \phi_{\xi\xi\xi} \\ \phi_{\xi\xi} \\ \phi_{\xi} \\ \phi_{\eta\eta\eta} \\ \phi_{\eta\eta} \\ \phi_{\eta} \\ \phi_{\eta\eta\xi} \\ \phi_{\eta\xi\xi} \\ \phi_{\eta\xi} \end{Bmatrix} = \begin{bmatrix} x_\xi^3 & & & & & & & & \\ & x_\xi^2 & & & & & & & \\ & & x_\xi & & & & & & \\ & & & y_\eta^3 & & & & & \\ & & & & y_\eta^2 & & & & \\ & & & & & y_\eta & & & \\ & & & & & & [y_\eta]^2 x_\xi & & \\ & & & & & & & y_\eta [x_\xi]^2 & \\ & & & & & & & & y_\eta x_\xi \end{bmatrix} \begin{Bmatrix} \phi_{xxx} \\ \phi_{xx} \\ \phi_{x} \\ \phi_{yyy} \\ \phi_{yy} \\ \phi_{y} \\ \phi_{yyx} \\ \phi_{yxx} \\ \phi_{yx} \end{Bmatrix} \tag{3.28}$$

Surface velocity and mid-plane power

Although the ESPF method could be extended to include the power component due to in-plane motion, the work in this dissertation focuses on the power due to out-of-plane motion only. The mechanics models from which the equations used to compute power are derived have several underlying assumptions as will be discussed in the next section. However, the assumptions that the displacements in the vibrating structure are small is also used in the ESDM solution of the velocity field.

Figure 3.16 shows an initially flat beam in both an undeformed and a deformed state. The deformation has been extremely exaggerated in order to more clearly visualize the angles and distances of interest. In the ESDM method the laser measures the velocity at point M_p but maps this velocity to the undeformed x, y, z coordinate system which would be point A. In order for this mapping to be valid, the small angle or displacement theory must be applied. Under the small displacement theory the angle ψ is small and hence the $\cos\psi \simeq 1$ and $\sin\psi \simeq \psi$ where ψ is in radians. This implies that length A-B is the same as length B-M_p.

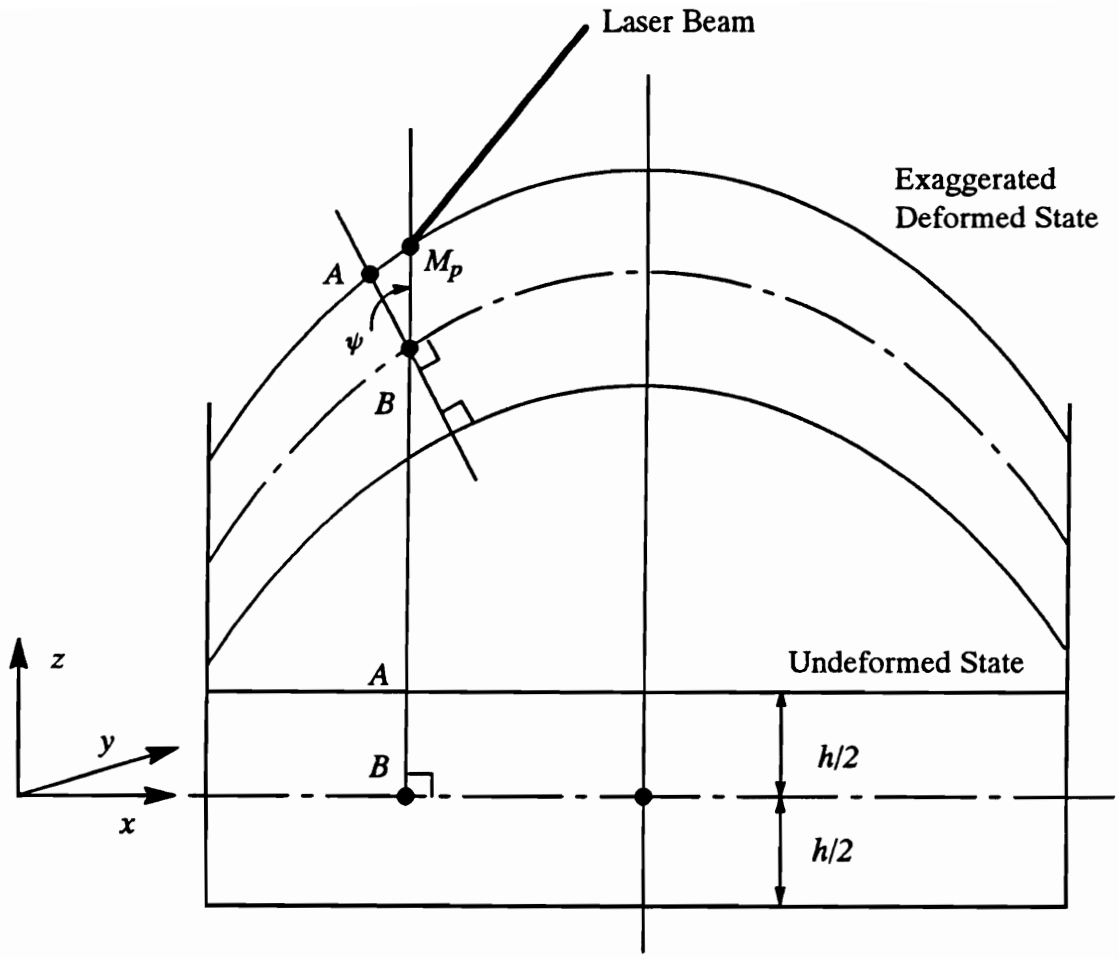

Figure 3.16. Surface to mid-plane velocity relationship

Another point of concern is that the laser measures the velocity at the surface of the structure and the power is computed about the mid-plane of the structure. However, referring again to Fig 3.16. it is shown that the transverse velocity at point M_p is the same as the transverse velocity at point B if small displacements are assumed. This is also discussed by Shames and Dym [50]. Therefore, the power due to transverse motion only, can be computed from the surface normal velocity.

3.4 Power-Flow Development

Nomenclature

a, b	plate dimensions
E	Young's modulus of elasticity
F	generalized force
F_r	real component of the force
F_i	imaginary component of the force
h	thickness
I	area moment of inertia
$Im[\,]$	Imaginary part of the quantity
L	beam length
M	bending or twisting moment
P	total power
q	power component
Q	shear force
$Re[\,]$	Real part of the quantity
u, v, w	displacements
$\dot{u}, \dot{v}, \dot{w}$	velocities
h	thickness
γ	shear strain
ϵ	normal strain
η	structural damping factor
ρ	beams (mass per unit length kg/m)
	plates (mass per unit volume kg/m^3)
σ	normal stress

τ	shear stress
ω	forcing frequency
ω_n	natural frequency

Subscript

ξ, η	parametric coordinates
x, y, z	generalized force and velocity directions

3.4.1 Introduction

This section presents the theoretical development of the power in vibrating beams and plates. The development presented will consist of deriving the general expressions for power in terms of the displacements. The power equations used to compute the energy injected into the structure through a source acting over a finite area will also be presented.

3.4.2 General Power Development

Power is defined as the time-averaged product of the phased generalized force and velocity components in the direction of the force. Mathematically power can be represented as shown by Eq. (3.29) [51]. Although Eq. (3.29) represents the dot product of two vectors, the power can be given a direction due to the fact that the directions of the generalized forces and the generalized velocities are known. It should be noted that the power in this dissertation refers to structural or mechanical power.

$$P = \left[\mathrm{Re}\left[Fe^{i\omega t}\right] \cdot \mathrm{Re}\left[Ve^{i\omega t}\right]\right] \tag{3.29}$$

In Eq. (3.29), F and V represent complex values which can be expressed as shown by Eqs. (3.30) where i represents the imaginary number $\sqrt{-1}$. In Eqs. (3.30), F_r, F_i, V_r, and V_i are real numbers.

$$F = F_r + iF_i \qquad V = V_r + iV_i \tag{3.30}$$

By substituting Eqs. (3.30) into Eq. (3.29) and using Euler's complex number expansion formula, Eq. (3.29) can be rewritten as shown by Eq. (3.31).

$$P = \left[F_r \cos[\omega t] - F_i \sin[\omega t]\right] \cdot \left[V_r \cos[\omega t] - V_i \sin[\omega t]\right] \tag{3.31}$$

Performing the multiplication shown in Eq. (3.31) results in Eq. (3.32).

$$P = F_r V_r \cos^2[\omega t] + F_i V_i \sin^2[\omega t] - \left[F_r V_i + F_i V_r\right] \cos[\omega t] \sin[\omega t] \tag{3.32}$$

By taking the time-average of Eq. (3.32) over an integral number of periods, the last term goes to zero and both the cosine-squared and sine-squared terms become $\frac{1}{2}$. Therefore, the time-averaged power can be expressed as shown by Eq. (3.33) where the star indicates complex conjugate.

$$P = \frac{1}{2}\left[F_r V_r + F_i V_i\right] = \frac{1}{2} \mathrm{Re}\left[F \cdot V^*\right] \tag{3.33}$$

Equation (3.33), represents the real or active power in the structure. The active power represents the net flow of energy in the structure and can be used to identify locations of energy sources and sinks. It is further noted that Eq. (3.33) is independent of time, this implies that the steady-state power in the structure over one complete cycle does not change with time.

The reactive power component is obtained by taking the imaginary part of the force and velocity dot product instead of the real part as shown by Eq. (3.34). The reactive power indicates the amount of reverberance in the field and does not contribute to the net power flow [25]. Although the reactive power has no real physical meaning it can be used for calculating other quantities such as the product of the time-averaged kinetic and potential energy densities, the time-average of the Lagrangian density, the curl of the active intensity, the energy flux density as a function of time, and the gradient of the time-averaged potential energy density. From this view point, the reactive power can be considered a useful tool [52].

$$P_{reactive} = \frac{1}{2} \mathrm{Im}\left[F \cdot V^*\right] \tag{3.34}$$

Equations (3.33) and (3.34) can be used to compute the power at a point. To compute the total power injected to a structure by an external force the power equation given by Eq. (3.33)

must be integrated over the area the force is applied as shown by Eq. (3.35). In Eq. (3.35), s represents the area over which the force is applied.

$$P = = \frac{1}{2} \int_{s} \mathrm{Re}\left[F \cdot V^{*}\right] ds \tag{3.35}$$

In the ESPF method, the power is a spatially continuous field but is computed at discrete points using Eq. (3.33). The forces in this case are not the externally applied loads but the internal forces which develop in the structure due to the applied loads. The power equation given by Eq. (3.35) is used in the power simulation models discussed in Chapter 4 but is not part of the ESPF process. This chapter continues by discussing in detail the development of the power equations specifically for beams and plates.

3.4.3 Structural Power in Beams

In general, energy in beams has six transport mechanisms. The six force components of these mechanisms consist of an axial force Q_x, two shear forces Q_y and Q_z, two bending moments M_x and M_y, and torque T. The associated generalized velocities are the translational velocities $\dot{u}$, $\dot{v}$, $\dot{w}$, and the angular velocities $\dot{\theta}_x$, $\dot{\theta}_y$, and $\dot{\theta}_z$. The positive directions of these generalized forces and velocities are defined on a beam element as shown in Fig. 3.17. Due to the mechanics models, energy in beams is restricted to flow unidirectionally along the length of the beam as clearly indicated by the definitions of the generalized forces and velocities shown in Fig. 3.17.

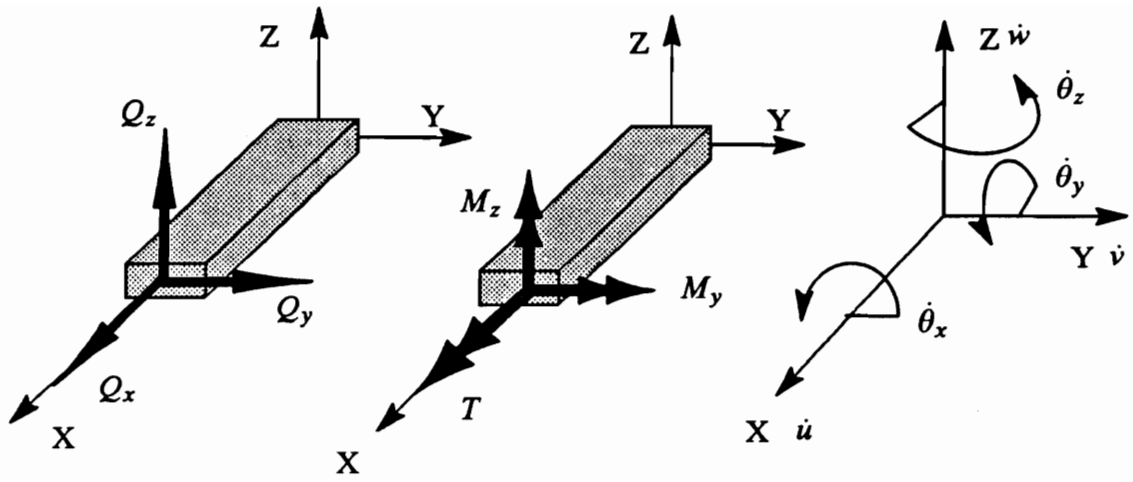

Figure 3.17. General beam coordinate system, force, and velocity positive direction definitions

Substituting the force and velocity beam power components into Eq. (3.33), an expression for the power in beams is obtained as shown by Eq. (3.36).

$$q_x = \frac{1}{2}\,\mathrm{Re}\left[Q_x\dot{u}^* + Q_y\dot{v}^* + Q_z\dot{w}^* + M_y\dot{\theta}_y^* + M_z\dot{\theta}_z^* + T\dot{\theta}_x^*\right] \quad (3.36)$$

Equation (3.36) is general in that it considers all possible modes of energy transport in a beam. When only transverse motion in the z-direction is considered, the possible energy transport mechanisms are reduced from six to two as shown by Eq. (3.37).

$$q_x = \frac{1}{2}\,\mathrm{Re}\left[Q_z\dot{w}^* + M_y\dot{\theta}_y{}^*\right] \quad (3.37)$$

Expanding Eq. (3.37) and using a complex modulus to represent the damping of the material in the structure results in Eq. (3.38). Equation (3.38), represents an expression for the total time-averaged power due to transverse motion of a Bernoulli-Euler beam broken into real and imaginary components.

$$\begin{aligned} q_x = {} & .5[\mathrm{Re}[Q_z]\,\mathrm{Re}[\dot{w}] + \mathrm{Im}[Q_z]\,\mathrm{Im}[\dot{w}]] + .5\left[\mathrm{Re}[M_y]\,\mathrm{Re}\left[\dot{\theta}_y\right] + \mathrm{Im}[M_y]\,\mathrm{Im}\left[\dot{\theta}_y\right]\right] + \\ & .5\,\eta\,[\mathrm{Re}[Q_z]\,\mathrm{Im}[\dot{w}] - \mathrm{Im}[Q_z]\,\mathrm{Re}[\dot{w}]] + .5\,\eta\left[\mathrm{Re}[M_y]\,\mathrm{Im}\left[\dot{\theta}_y\right] - \mathrm{Im}[M_y]\,\mathrm{Re}\left[\dot{\theta}_y\right]\right] \end{aligned} \quad (3.38)$$

In this analysis, the focus will be on beams subject to transverse motion only. For this case Eq. (3.37) completely represents the power model. The next step is to express the power model in terms of the displacements. These expressions are developed by satisfying equilibrium, and using the strain-displacement and stress-strain relations.

Equilibrium

The first step is to draw a free body diagram and write the equilibrium equation. Figure 3.18 illustrates a simply supported beam and a typical beam element with the assumed positive directions of the generalized forces and velocities that are used in this development.

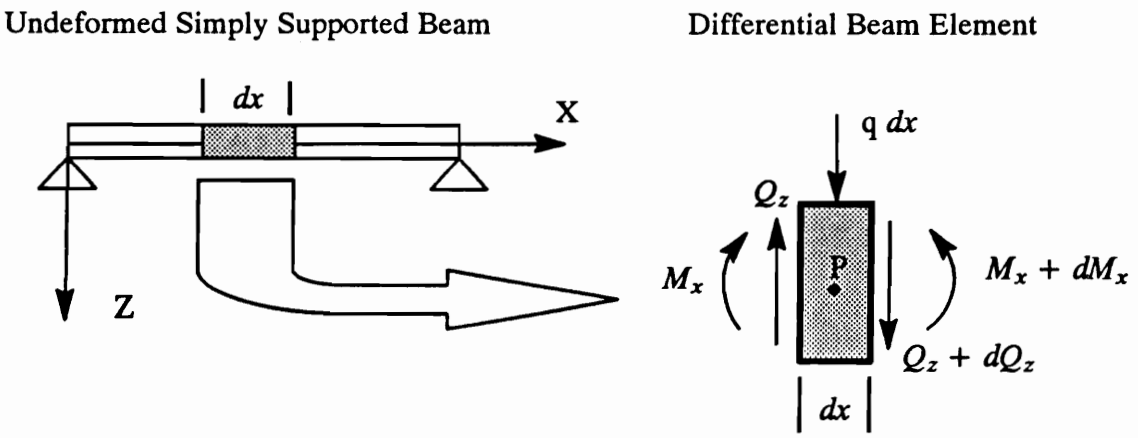

Figure 3.18. Generalized force and beam coordinate system definitions

From the free-body diagram of the differential beam element shown in Fig. 3.18 the differential equations of equilibrium for the transverse force and moment components are obtained. This is done by summing the vertical forces and moments about point p and eliminating higher-order differentials as shown by Eqs. (3.39).

$$q dx + dQ_z = 0 \qquad Q_z dx - dM_x = 0 \tag{3.39}$$

Substituting the latter equation into the former results in a single differential equation as shown by Eq. (3.40).

$$q + \frac{d^2M_x}{dx^2} = 0 \tag{3.40}$$

Strain-displacement equations

The second step is to derive the strain-displacement relations. Consider a section through the beam before and after deformation as shown by Fig. 3.19. Point A at a distance z from the middle surface before deformation has moved to point A' after deformation. The displacement of point A in the x-direction is equal to the middle surface displacement u_o minus the displacement due to rotation as shown by Eq. (3.41).

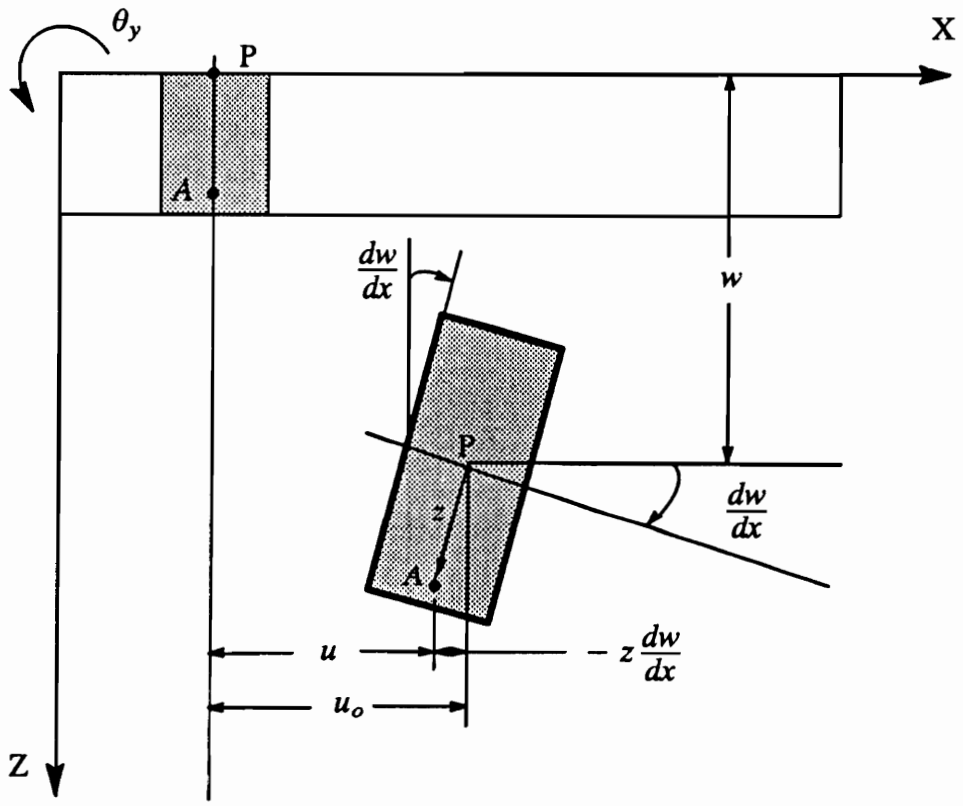

Figure 3.19. Strain-displacement geometric representation

$$u = u_o - z\frac{\partial w}{\partial x} \tag{3.41}$$

The strains are then obtained by the differentiation shown by Eq. (3.42).

$$\epsilon_x = \frac{du}{dx} \quad so \quad \epsilon_x = \frac{du_o}{dx} - z\frac{d^2w}{dx^2} \tag{3.42}$$

The $\frac{du_o}{dx}$ term represents the extensional effects and under the transverse motion only assumption this term goes to zero. Therefore, the strain-displacement equation is as shown by Eq. (3.43).

$$\epsilon_x = -z\frac{d^2w}{dx^2} \tag{3.43}$$

Stress-strain relations

Now that the strain is expressed in terms of the transverse displacement, the next step consists of using this expression to represent the generalized forces in terms of the transverse displacement. Using Hookes Law, the normal stress, σ_x, can be expressed as shown by Eqs.(3.44).

$$\sigma_x = E\,\epsilon_x = -E\,z\,\frac{\partial^2 w}{\partial x^2} \tag{3.44}$$

The bending moment, M_x, is obtained by integrating the normal stress, σ_x, through the thickness, h, as shown by Eqs. (3.45). In Eqs. (3.45), b represents the width of the beam and I represents the moment of inertia of the cross-sectional area about the neutral axis.

$$M_x = \int_{\frac{-h}{2}}^{\frac{h}{2}} \sigma_x z\, b\, dz \quad \Rightarrow \quad \sigma_x = \frac{M z}{I} \tag{3.45}$$

Substituting Eq. (3.44) into the second of Eqs. (3.45) and rearranging terms the bending moment in a beam can be expressed as shown by Eq. (3.46).

$$M_x = -EI\,\frac{\partial^2 w}{\partial x^2} \tag{3.46}$$

The shear force is obtained by substitution into the second equation of Eq. (3.39) as shown by Eq. (3.47).

$$Q_x = -EI\frac{\partial^3 w}{\partial x^3} \tag{3.47}$$

The generalized velocities associated with these forces in terms of displacements are also obtained from Fig. 3.18 as shown by Eq. (3.48).

$$\dot{w} = \frac{dw}{dt} \qquad \dot{\theta}_y = -\frac{d^2 w}{dx\,dt} \tag{3.48}$$

In the ESPF method Eqs. (3.46), (3.47), and (3.48) represent complex-valued forces and velocities. Substituting these equations into Eq. (3.33) results in the power equation expressed in terms of displacements for a Bernoulli-Euler beam as shown by Eq. (3.49) where the star indicates complex conjugate.

$$q_x = \frac{1}{2}\,\mathrm{Re}\left[-EI\frac{d^3 w}{dx^3}\,\frac{dw^*}{dt} + EI\frac{d^2 w}{dx^2}\,\frac{\partial^2 w^*}{\partial x\,\partial t}\right] \tag{3.49}$$

This derivation is based on Bernoulli-Euler beam theory and neglects shear deformation in the potential energy and rotatory inertia in the kinetic energy formulations. It is further assumed that planes remain plane during bending and that only small displacements in the structure occur.

Development of the displacement equation

Now that the power is expressed in terms of the transverse displacement, an expression for this displacement will be developed such that analytical beam power models can be investigated and used to validate the theory of the ESPF method before experimental data is applied. It is well known that the equation of motion of a vibrating beam can be expressed as shown by Eq. (3.50) [53]. In Eq. (3.50), w represents the transverse displacement, η, represents the structural damping factor, m is the mass per unit length of the beam in kg/m, ω is the forcing frequency, the product of Young's modulus of elasticity and the area moment of inertia is given by EI, and F represents the applied force.

$$(1 + i\eta)\frac{\partial^4 w}{\partial x^4} - \frac{m\omega^2}{EI}w = \frac{F(x)}{EI} \tag{3.50}$$

This is the same equilibrium equation as given by Eq. (3.40) except that it accounts for the dynamics of the beam and incorporates a complex Young's modulus of elasticity to account for the damping in the structure. The complex stiffness is used to represent the structural damping due to the hysteresis associated with cyclic stresses. In structures subject to harmonic excitation structural damping can be represented as viscous damping by the complex Young's modulus [53].

In order to solve Eq. (3.50), boundary conditions and a description of the force are required. A schematic of the simply supported beam used in the ESPF simulation models is shown in Fig. 3.20. It will be assumed that the force is harmonic and uniformly distributed between X_1 and X_2 as expressed by Eq. (3.51).

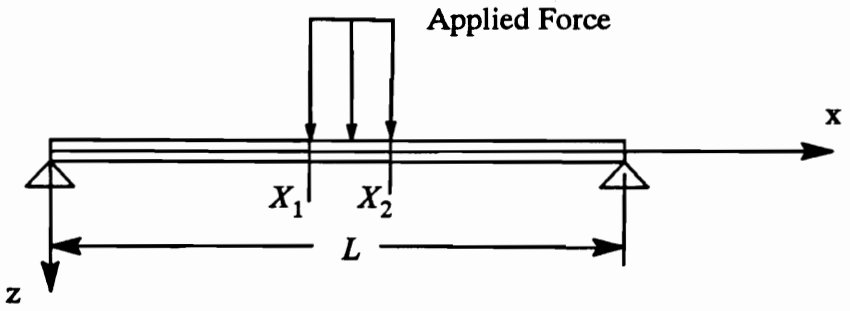

Figure 3.20. Beam setup and force description

$$F(x) = \begin{cases} F & x_1 \le x \le x_2 \\ 0 & \textit{everywhere else} \end{cases} \tag{3.51}$$

The first step in the development of an expression for the displacement is to represent the force in terms of an infinite series. Let the force be represented by Eq. (3.52) where the ϕ_n's are a set of orthogonal functions which are single-valued, continuous in the interval, and real. The a_n's represent the coefficients or weighting terms of the ϕ_n's.

$$F(x) = \sum_{n=1}^{\infty} a_n \phi_n(x) \tag{3.52}$$

For the simply supported beam let the $\phi_n's$ be expressed as shown by Eq. (3.53). Equation (3.53) satisfies both the geometric and the natural boundary conditions of the simply supported beam.

$$\phi_n(x) = \sin\frac{n\pi x}{L} \tag{3.53}$$

To solve for a_n multiply both sides of Eq. (3.52) by what multiplies a_n, $\left(i.e. \ \sin\frac{n\pi x}{L} \right)$, and then integrate over the length of the beam as shown by Eq. (3.54).

$$\int_0^L F(x) \sin\frac{r\pi x}{L} dx = \int_0^L \sum_{n=1}^{\infty} a_n \sin\frac{n\pi x}{L} \sin\frac{r\pi x}{L} dx \tag{3.54}$$

Using the orthogonality concept, all the terms in the summation are zero except for $n = r$. Integrating and solving for a_n results in Eq. (3.55).

$$a_n = \frac{2F}{n\pi}\left[\cos\frac{n\pi x_1}{L} - \cos\frac{n\pi x_2}{L}\right] \tag{3.55}$$

Rewriting Eq. (3.52) making substitutions for a_n and ϕ_n an expression for the force as shown by Eq. (3.56), where F is in units of N/m is obtained.

$$F(x) = \sum_{n=1}^{\infty} \frac{2F}{n\pi}\left[\cos\frac{n\pi x_1}{L} - \cos\frac{n\pi x_2}{L}\right] \sin\frac{n\pi x}{L} \tag{3.56}$$

Now that the force has been expressed in terms of a series we can perform a similar procedure on the equation of motion given by Eq. (3.50). As before, the first step consists of assuming a solution as given by Eq. (3.57). Substituting this into Eq. (3.50) results in Eq. (3.58).

$$w(x) = \sum_{n=1}^{\infty} w_n \sin\frac{n\pi x}{L} \tag{3.57}$$

$$\begin{aligned}(1 + j\eta) \sum_{n=1}^{\infty} w_n\left[\frac{n\pi}{L}\right]^4 \sin\frac{n\pi x}{L} - \frac{m\omega^2}{EI} \sum_{n=1}^{\infty} w_n \sin\frac{n\pi x}{L} = \\ \sum_{n=1}^{\infty} \frac{2F}{EIn\pi}\left[\cos\frac{n\pi x_1}{L} - \cos\frac{n\pi x_2}{L}\right]\sin\frac{n\pi x}{L}\end{aligned} \tag{3.58}$$

Solving for w_n by multiplying both sides of Eq. (3.58) by the coefficients of the w_n terms integrating over the beam, and using orthogonality it can be shown that w_n is given by Eq. (3.59).

$$w_n = \frac{\frac{2F}{n\pi m}\left[\cos\frac{n\pi x_1}{L} - \cos\frac{n\pi x_2}{L}\right]}{(1 + i\eta)\frac{EI}{mL^4}(\pi)^4 - \omega^2} \tag{3.59}$$

Substituting Eq. (3.59) into Eq. (3.57) and recalling that the unforced natural frequencies of a beam are given by Eq. (3.60), it can be shown that the displacement of the beam is given by Eq. (3.61).

$$\omega_n^2 = \frac{EI}{mL^4}(n\pi)^4 \tag{3.60}$$

$$w = \frac{\frac{2F}{n\pi m}\left[\cos\frac{n\pi x_1}{L} - \cos\frac{n\pi x_2}{L}\right]}{\omega_n^2\left[\left[1 - \frac{\omega^2}{\omega_n^2}\right]^2 + \eta^2\right]^{\frac{1}{2}}}\sin\frac{n\pi x}{L} \tag{3.61}$$

From this expression for the displacement the velocity in the beam can be obtained by taking the time derivative of Eq. (3.61). The time derivative is obtained simply by multiplying Eq. (3.61) by $i\omega$. This result is shown by Eq. (3.62).

$$\dot{w}(x) = \sum_{n=1}^{n=\infty} \frac{\frac{2F\omega}{n\pi m}\left[\cos\left[\frac{n\pi X_1}{L}\right] - \cos\left[\frac{n\pi X_2}{L}\right]\right]\left[i(\omega_n{}^2 - \omega^2) + \eta\omega_n{}^2\right]\sin\left[\frac{n\pi x}{L}\right]}{\left[(\omega_n{}^2 - \omega^2)^2 + (\eta\omega_n{}^2)^2\right]} \tag{3.62}$$

Substituting Eqs. (3.56) and (3.62) into Eq. (3.33) results in Eq. (3.63) which is an expression for the power in the system at any point x.

$$P(x) = \frac{2F^2\omega}{\pi\rho}\sum_{n=1}^{n=\infty}\frac{1}{n^2}\frac{\left[\cos\left[\frac{n\pi X_1}{L}\right] - \cos\left[\frac{n\pi X_2}{L}\right]\right]^2\left[\eta\omega_n{}^2\right]\sin^2\left[\frac{n\pi x}{L}\right]}{\left[(\omega_n{}^2 - \omega^2)^2 + (\eta\omega_n{}^2)^2\right]} \tag{3.63}$$

The total power entering the system due to the applied load is obtained by integrating Eq. (3.63) as shown by Eq. (3.64).

$$P(x) = \frac{2F^2\omega}{\pi\rho}\int_{X_1}^{X_2}\sum_{n=1}^{n=\infty}\frac{1}{n^2}\frac{\left[\cos\left[\frac{n\pi X_1}{L}\right] - \cos\left[\frac{n\pi X_2}{L}\right]\right]^2 \left[\eta\omega_n{}^2\right] \sin^2\left[\frac{n\pi x}{L}\right]}{\left[\left(\omega_n{}^2 - \omega^2\right)^2 + \left(\eta\omega_n{}^2\right)^2\right]} dx \quad (3.64)$$

3.4.4 Structural Power in Plates

The development of the power equations in plates is similar to the development for beams except that now the energy flow is no longer unidirectional. In general, the power equations in plates consist of transverse shear forces Q_x, Q_y, membrane forces F_x, F_y, membrane shear F_{xy}, F_{yx}, bending moments M_x, M_y, and twisting moments M_{xy}, M_{yx}. The velocities which correspond to these forces are the translational velocities $\dot{w}$, $\dot{u}$, $\dot{v}$, and the rotational velocities $\dot{\theta}_x$, $\dot{\theta}_y$. The power equations in the x and y directions are given by Eqs. (3.65) and (3.66) A schematic of these forces and velocities indicating positive directions for a differential plate element is shown in Fig. 3.21. It should be noted that the definitions of the bending moments for the plates are different than the definitions used in the beam.

$$q_x = \frac{1}{2}\mathrm{Re}\left[Q_x\dot{w}^* + F_x\dot{u}^* + F_{xy}\dot{v}^* + M_x\dot{\theta}_y^* + M_{xy}\dot{\theta}_x^*\right] \quad (3.65)$$

$$q_y = \frac{1}{2}\mathrm{Re}\left[Q_y\dot{w}^* + F_y\dot{v}^* + F_{yx}\dot{u}^* + M_y\dot{\theta}_x^* + M_{yx}\dot{\theta}_y^*\right] \quad (3.66)$$

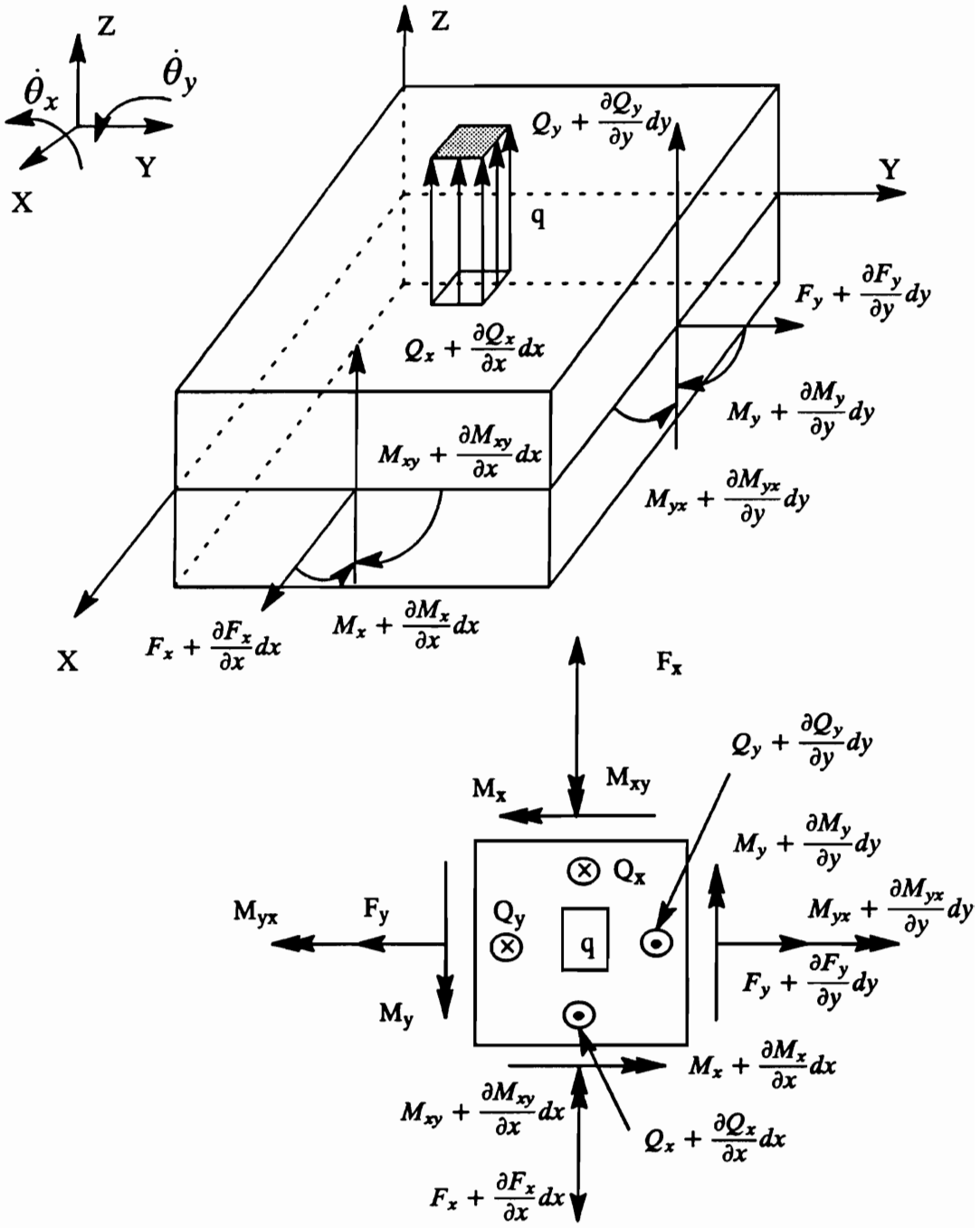

Figure 3.21. Plate coordinate system and positive direction definitions

When only transverse motion in the z-direction is considered Eqs. (3.65) and (3.66) reduce to Eqs. (3.67) and (3.68). These equations can be further expanded in terms of real and imaginary components as was done for the beam as shown by Eq. (3.38).

$$q_x = \frac{1}{2}\mathrm{Re}\left[Q_x\dot{w}^* + M_x\dot{\theta}_y^* + M_{xy}\dot{\theta}_x^*\right] \tag{3.67}$$

$$q_y = \frac{1}{2}\mathrm{Re}\left[Q_y\dot{w}^* + M_y\dot{\theta}_x^* + M_{yx}\dot{\theta}_y^*\right] \tag{3.68}$$

The next step is to express the forces and velocities given in Eqs. (3.65) and (3.66) in terms of displacements. Using the free-body diagram of the plate element shown in Fig. 3.21 and summing forces in the vertical direction, summing moments about the center of the plate and parallel to the y-axis, and summing moments about the center of the plate and parallel to the x-axis it can be shown that Eqs. (3.69) develop respectively.

$$q + \frac{\partial Q_y}{\partial y} + \frac{\partial Q_x}{\partial x} = 0, \qquad \frac{\partial M_x}{\partial x} + \frac{\partial M_{xy}}{\partial y} - Q_x = 0, \qquad \frac{\partial M_y}{\partial y} + \frac{\partial M_{yx}}{\partial x} - Q_y = 0 \tag{3.69}$$

Taking the partial derivative with respect to x of the second equation of Eqs. (3.69) and the partial derivative with respect to y of the third equation of Eqs. (3.69) and substituting into the first of Eqs. (3.69) , one equation which satisfies equilibrium in the plate can be developed as shown by Eq. (3.70).

$$\frac{\partial^2 M_x}{\partial x^2} + 2\frac{\partial^2 M_{xy}}{\partial x \partial y} + \frac{\partial^2 M_y}{\partial y^2} + q(x,y) = 0 \tag{3.70}$$

Equation (3.70) contains three unknowns. However, using strain-displacement relations which are derived from the deformed geometry and stress-strain relations which are based on the material properties Eq. (3.70) can be reduced to an equation with a single unknown which is the transverse displacement.

Strain-displacement relations

The development of the strain-displacement relations for plates is very similar to the development for beams. Therefore, assume that the deformed beam section shown by Fig. 3.19

represents a plate. Using Fig. 3.18 for both the x and y direction as well as the theory previously discussed it can easily be shown that the strain displacement relations are as shown by Eqs. (3.71).

$$\epsilon_x = \frac{\partial u}{\partial x} = \frac{\partial u_o}{\partial x} - z\frac{\partial^2 w}{\partial x^2}$$
$$\epsilon_y = \frac{\partial v}{\partial y} = \frac{\partial v_o}{\partial y} - z\frac{\partial^2 w}{\partial y^2} \tag{3.71}$$
$$\gamma_{xy} = \frac{\partial u_o}{\partial y} + \frac{\partial v_o}{\partial x} - 2z\frac{\partial^2 w}{\partial x \partial y}$$

Again, the terms $\frac{\partial u_o}{\partial x}$, $\frac{\partial v_o}{\partial y}$, $\frac{\partial u_o}{\partial y}$, and $\frac{\partial v_o}{\partial x}$ represent the extensional effects and in pure transverse motion can be neglected.

Stress-strain relations

The state of stress for thin plates can be represented as a plane-stress state. Substituting the strain-displacement equations into Hookes Law for plane-stress results in Eqs. (3.72).

$$\sigma_x = \frac{E}{1-\nu^2}[\epsilon_x + \epsilon_y] = \frac{E}{1-\nu^2}(-z)\left[\frac{\partial^2 w}{\partial x^2} + \nu\frac{\partial^2 w}{\partial y^2}\right]$$
$$\sigma_y = \frac{E}{1-\nu^2}[\epsilon_y + \epsilon_x] = \frac{E}{1-\nu^2}(-z)\left[\frac{\partial^2 w}{\partial y^2} + \nu\frac{\partial^2 w}{\partial x^2}\right] \tag{3.72}$$
$$\tau_{xy} = \frac{E}{2(1+\nu)}\gamma_{xy} = \frac{E}{1-\nu^2}\left(\frac{1-\nu}{2}\right)(-2z)\frac{\partial^2 w}{\partial x^2}$$

Expressions for the moments are now obtained by integrating the stress–strain relations as shown by Eqs. (3.73).

$$M_x = \int_{\frac{-h}{2}}^{\frac{h}{2}} \sigma_x z\, dz, \quad M_y = \int_{\frac{-h}{2}}^{\frac{h}{2}} \sigma_y z\, dz, \quad M_{xy} = \int_{\frac{-h}{2}}^{\frac{h}{2}} \tau_{xy} z\, dz \tag{3.73}$$

Performing these integrations and using Eqs. (3.69) to determine the shear forces it can be shown that Eqs. (3.74)-(3.78) represent the three generalized forces and velocities in

terms of the transverse displacement only. These equations can be substituted into Eq. (3.33) to express the power in terms of displacements as shown by Eqs. (3.79) and (3.80).

$$M_x = D\left(\frac{\partial^2 w}{\partial x^2} + \nu\frac{\partial^2 w}{\partial y^2}\right); \qquad M_y = D\left(\frac{\partial^2 w}{\partial y^2} + \nu\frac{\partial^2 w}{\partial x^2}\right) \tag{3.74}$$

$$Q_x = D\frac{\partial}{\partial x}\left(\frac{\partial^2 w}{\partial x^2} + \frac{\partial^2 w}{\partial y^2}\right); \qquad Q_y = D\frac{\partial}{\partial y}\left(\frac{\partial^2 w}{\partial x^2} + \frac{\partial^2 w}{\partial y^2}\right) \tag{3.75}$$

$$M_{xy} = M_{yx} = D(1 - \nu)\frac{\partial^2 w}{\partial x \partial y} \tag{3.76}$$

$$D = -\frac{Eh^3}{12(1 - \nu^2)} \tag{3.77}$$

$$\dot{w} = \frac{\partial w}{\partial t} \qquad \dot{\theta}_x = \frac{\partial^2 w}{\partial y \partial t} \qquad \dot{\theta}_y = -\frac{\partial^2 w}{\partial x \partial t} \tag{3.78}$$

$$q_x = \frac{1}{2}\,\mathrm{Re}\left[D\frac{\partial}{\partial x}\left(\frac{\partial^2 w}{\partial x^2} + \frac{\partial^2 w}{\partial y^2}\right)\frac{\partial w^*}{\partial t} - D\left(\frac{\partial^2 w}{\partial x^2} + \nu\frac{\partial^2 w}{\partial y^2}\right)\frac{\partial^2 w^*}{\partial x \partial t}\right] - \frac{1}{2}\mathrm{Re}\left[D(1 - \nu)\frac{\partial^2 w}{\partial x \partial y}\frac{\partial^2 w^*}{\partial y \partial t}\right] \tag{3.79}$$

$$q_y = \frac{1}{2}\,\mathrm{Re}\left[D\frac{\partial}{\partial y}\left(\frac{\partial^2 w}{\partial y^2} + \frac{\partial^2 w}{\partial x^2}\right)\frac{\partial w^*}{\partial t} - D\left(\frac{\partial^2 w}{\partial y^2} + \nu\frac{\partial^2 w}{\partial x^2}\right)\frac{\partial^2 w^*}{\partial y \partial t}\right] - \frac{1}{2}\mathrm{Re}\left[D(1 - \nu)\frac{\partial^2 w}{\partial y \partial x}\frac{\partial^2 w^*}{\partial x \partial t}\right] \tag{3.80}$$

Plate displacement equation

The governing differential equation of motion for a plate subject to a uniformly distributed harmonic force is given by Eq. (3.81).

$$D\,(1 + i\eta)\nabla^4 w - m\,\omega^2\,w = F(x, y, t) \tag{3.81}$$

As in the derivation of the displacement equation for the beam, the first step is to obtain a Fourier series representation of the force. Following a similar procedure outlined for the

beam, it can be shown that a uniformly distributed force bounded by the rectangular area X_1 to X_2 and Y_1 to Y_2 is expressed as shown by Eq. (3.82).

$$F(x,y) = \sum_{m=1}^{\infty}\sum_{n=1}^{\infty}\frac{4F}{mn\pi^2}\left[\cos\frac{m\pi x_1}{a} - \cos\frac{m\pi x_2}{a}\right]\left[\cos\frac{n\pi y_1}{b} - \cos\frac{n\pi y_2}{b}\right]\sin\frac{m\pi x}{a}\sin\frac{n\pi y}{b} \quad (3.82)$$

For a simply supported plate assume the solution to Eq. (3.81) is given by Eq. (3.83).

$$w(x,y) = \sum_{m=1}^{\infty}\sum_{n=1}^{\infty} w_{mn}\sin\frac{m\pi x}{a}\sin\frac{n\pi y}{b} \quad (3.83)$$

Substituting Eq. (3.83) into Eq. (3.81), and using the orthogonality relationship it can be shown that w_{mn} in Eq. (3.83) is given by Eq. (3.84) where the natural frequencies ω_{mn} are given by Eq. (3.85).

$$w_{mn} = \frac{\frac{4FD}{\rho hmn\pi^2}\left[\cos\frac{m\pi x_1}{a} - \cos\frac{m\pi x_2}{a}\right]\left[\cos\frac{n\pi y_1}{b} - \cos\frac{n\pi y_2}{b}\right]}{D(1+i\eta)\omega_{mn}^2 - \frac{D}{\rho h}m\omega^2} \quad (3.84)$$

$$\omega_{mn} = \pi^2\left[\left[\frac{m}{a}\right]^2 + \left[\frac{n}{b}\right]^2\right]\sqrt{\frac{D}{\rho h}} \quad (3.85)$$

Substituting Eq. (3.84) into Eq. (3.83), and rearranging the denominator the displacement of the plate can be expressed as shown by Eq. (3.86).

$$w(x,y) = \sum_{m=1}^{\infty}\sum_{n=1}^{\infty}\frac{\frac{4F}{\rho hmn\pi^2}\left[\cos\frac{m\pi x_1}{a} - \cos\frac{m\pi x_2}{a}\right]\left[\cos\frac{n\pi y_1}{b} - \cos\frac{n\pi y_2}{b}\right]\times}{\left[\omega_{mn}^2 - \omega^2\right]^2 + \eta^2\omega_{mn}^4} \quad (3.86)$$
$$\left[\omega_{mn}^2 - \omega^2 - i\eta\omega_{mn}^2\right]\sin\frac{m\pi x}{a}\sin\frac{n\pi y}{b}$$

The velocity is obtained by multiplying Eq. (3.86) by $i\omega$ as shown by Eq. (3.87).

$$\dot{w}(x,y) = \sum_{m=1}^{\infty}\sum_{n=1}^{\infty}\frac{\frac{4F}{\rho hmn\pi^2}\left[\cos\frac{m\pi x_1}{a} - \cos\frac{m\pi x_2}{a}\right]\left[\cos\frac{n\pi y_1}{b} - \cos\frac{n\pi y_2}{b}\right]\times}{\left[\omega_{mn}^2 - \omega^2\right]^2 + \eta^2\omega_{mn}^4} \quad (3.87)$$
$$\left[i\left(\omega_{mn}^2 - \omega^2\right) + \eta\omega_{mn}^2\right]\sin\frac{m\pi x}{a}\sin\frac{n\pi y}{b}$$

Substituting the expressions for the force, Eq. (3.82), and the velocity, Eq. (3.87), into the power equation given by Eq. (3.33) results in an expression for the power as shown by Eq. (3.88). Equation (3.88), represents the discrete form of the injected power equation and can be used to compute the power at any x and y position in the structure.

$$P(x,y) = \frac{8F^2\eta\omega\omega_{mn}^2}{\rho h\pi^4}\sum_{m=1}^{\infty}\sum_{n=1}^{\infty}\frac{1}{m^2n^2}$$
$$\frac{\left[\cos\left[\frac{n\pi X_1}{a}\right] - \cos\left[\frac{n\pi X_2}{a}\right]\right]^2\left[\cos\left[\frac{n\pi Y_1}{b}\right] - \cos\left[\frac{n\pi Y_2}{b}\right]\right]^2 \sin^2\left[\frac{m\pi x}{a}\right]\sin^2\left[\frac{n\pi y}{b}\right]}{\left[\left(\omega_{mn}{}^2 - \omega^2\right)^2 + \left(\eta\omega_{mn}{}^2\right)^2\right]} \quad (3.88)$$

To compute the total power injected into the plate Eq. (3.88) is integrated over the boundaries of the distributed force as shown by Eq. (3.89).

$$P(x,y) = \frac{8F^2\eta\omega\omega_{mn}^2}{\rho h\pi^4}\int_{X_1}^{X_2}\int_{Y_1}^{Y_2}\sum_{m=1}^{\infty}\sum_{n=1}^{\infty}\frac{1}{m^2n^2}\sin^2\left[\frac{m\pi x}{a}\right]\sin^2\left[\frac{n\pi y}{b}\right]$$
$$\frac{\left[\cos\left[\frac{n\pi X_1}{a}\right] - \cos\left[\frac{n\pi X_2}{a}\right]\right]^2\left[\cos\left[\frac{n\pi Y_1}{b}\right] - \cos\left[\frac{n\pi Y_2}{b}\right]\right]^2}{\left[\left(\omega_{mn}{}^2 - \omega^2\right)^2 + \left(\eta\omega_{mn}{}^2\right)^2\right]}\,dy\,dx \quad (3.89)$$

This concludes the theoretical development of the power equations. The developments presented in this chapter are now used to compute the power in both beams and plates based on simulated laser data.

Chapter 4

Laser Simulated Power-Flow Results

The purpose of this chapter is to validate the ESPF theoretical development discussed in Chapter 3. This is done by comparing the results from three different methods of power computation. The first two methods are derived from a purely analytical representation of the power. The third method uses computer simulated laser data to solve for the velocity field from which the ESPF method computes the power. The ESPF method will be validated by showing that all three power methods provide similar results.

This chapter first describes the three methods used in the validation process. The results of the validation process are then presented for both a beam and a plate.

4.1 ESPF Beam Validation

This section first describes in detail the particular beam setup used in the validation procedure. The three methods used to compute the power in the beam are presented and the results are compared.

4.1.1 Beam Setup and Parameters

The beam setup consisted of a uniform simply supported beam with a uniform harmonic force applied over a small length of the beam at the mid-span. Figure 4.1 shows the setup of the beam model and the parameters used.

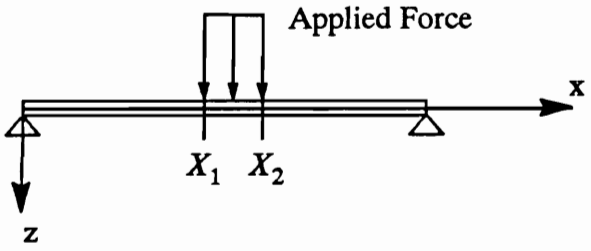

Model Parameters	
Youngs Modulus	2.040 x 10^{11} Pa
Damping Factor	0.001
Length	1.000 m
Width	0.050 m
Thickness	0.002 m
Force Magnitude	5.000 N/m
Forcing Frequency	4.500 Hz
Mass / Length	0.7869 kg/m
X_1	0.490 m
X_2	0.510 m

Figure 4.1. Beam setup and model parameters

4.1.2 Method 1, Analytical Injected Power

Method 1 consisted of computing the power injected into the beam from an analytical equation. The time-averaged power injected into the beam through the uniformly distributed force F acting over the area between X_1 and X_2 can be computed by integrating Eq. (3.64).

4.1.3 Method 2, Derivative-Based Analytical Power

The second method used to compute the power consisted of using Eq. (3.62) as the velocity field. The derivatives required to compute the power as shown by Eq. (3.49) were computed directly from derivatives of Eq. (3.62). This method represents a pure analytical power-flow method that is based on a displacement approach. Units of watts are obtained directly from the formulation used in this method.

4.1.4 Method 3, ESPF Power Using Simulated Laser Data

The third method used to compute the power in the beam consisted of developing a computer code which would create simulated laser data. The ESDM technique was used to solve for the 3-D velocity field from the simulated laser data. The simulator was developed such

that an equation which represents the velocity field over the structure is sampled in the same manner the laser samples the velocity field of a real structure. In this case, Eq. (3.62) was used from which simulated laser samples were computed. The structural coordinates, parametric coordinates, direction cosines from the structure to the laser, the real and imaginary velocity magnitudes, and the signal processing statistics were all computed as if the data was actually acquired by the SLDV. The simulator has the distinct advantage that experimental noise in the system can be completely controlled. The idea behind this case is to verify that given ideal data the ESPF method can accurately compute both the magnitude and spatial location of the power injected into the beam.

4.1.5 Validation Procedure and Results

The first validation test consisted of verifying the derivative approach of computing power in a structure. This was done by comparing the results of the power injected into the system as computed by Methods 1 and 2. Theoretically, the sum of the power at X_1 and X_2 computed by Method 2, plus the power dissipated between X_1 and X_2 due to structural damping, should equal the total injected power computed by Method 1. However, if the distance between X_1 and X_2 is relatively small and if the material exhibits low structural damping, the power dissipated between X_1 and X_2 is small, and can be neglected as was done in these computations.

The percent difference between Methods 1 and 2 was computed as shown by Eq. (4.1).

$$Percent\ Error = \left[\frac{Method2 - Method1}{Method1}\right] \times 100 \tag{4.1}$$

Figure 4.2 illustrates the percent difference in the injected power computed by Methods 1 and 2 over the frequency range of 0 to 200 Hz. It is shown that the maximum difference over the frequency range investigated was approximately 4.0%. The solid straight lines in Fig. 4.2 represent the natural frequencies of the beam. It is noted that a zero crossing of the residual error occurs near each resonance frequency. This is due to the fact that at a resonance

frequency, one term in the infinite series is the dominant term and the other terms are considerably smaller in magnitude. At an off-resonance frequency, several terms in the series are required to represent the true response. Therefore, a greater possibility of error is introduced due to the number of terms that have a significant impact on the summation in the off-resonance frequency cases compared to the near-resonance frequency cases. In off-resonance cases the effect of the finite summation of terms in the series is particularly easy to see in Fig. 4.2.

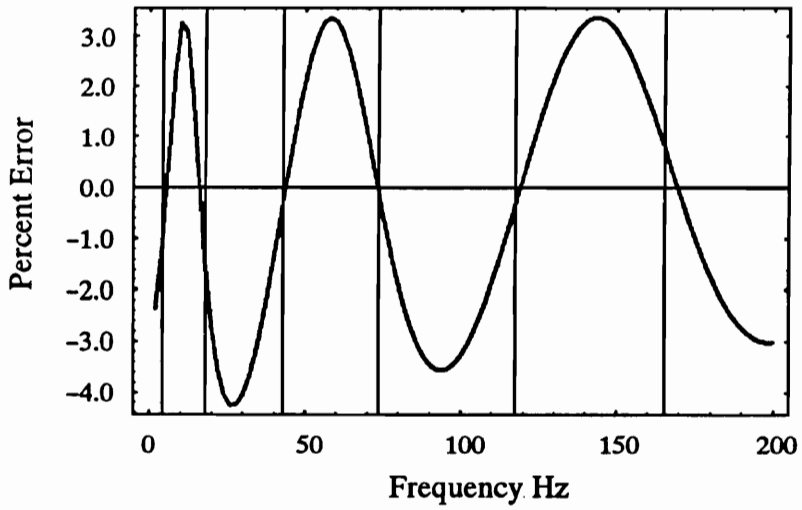

Figure 4.2. Percent error in injected power between Methods 1 and 2

The differences in the injected power computations between these two methods are due to several factors. The first is the fact that infinite sums were only approximated in the force, velocity, and power per unit length computations by using 500 terms in the series. This effect is aggravated by taking higher spatial derivatives. The second is that the power integral of Eq. (3.64) was computed discretely, as a sum, instead of a true integral. The third is that some of the power injected over the X_1, X_2 interval is dissipated due to structural damping before it arrives at the X_1, X_2 points where Method 2 was used to compute the power. Considering these possibilities for which error could be introduced, it was determined that the derivative

method of computing power in beams is certainly valid and one can show that the injected power is conserved.

The second test consisted of comparing the power results from Methods 2 and 3. The purpose of this test was to show that the ESPF approach in which the velocity field is solved for using the ESDM technique is capable of conserving the injected power.

The real and imaginary components of the velocity fields acquired by Methods 2 and 3 are shown in Fig. 4.3. The prescribed velocity obtained directly from Eq. (3.62), is shown as the analytical representation. In Method 3, three mesh densities were investigated as shown in Fig. 4.3. At this plot resolution it is impossible to visually detect any variation in the 4 models. The components of interest that are discussed in this section were computed and compared at 101 points along the beam.

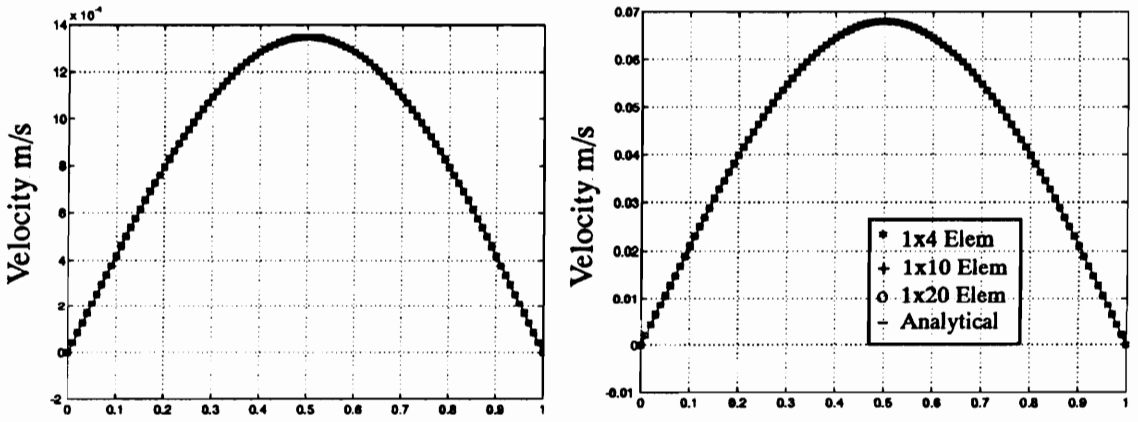

Figure 4.3. Real and imaginary velocities at 4.5 Hz

Figure 4.4 shows a plot of the real and imaginary velocity residuals between Method 2 and the 1x10 element model of Method 3. The residuals for the real and imaginary velocity components do not appear to be completely random. However, the residuals have a differ-

ence of 5 orders of magnitude in the worst case which occurs in the imaginary velocity representation.

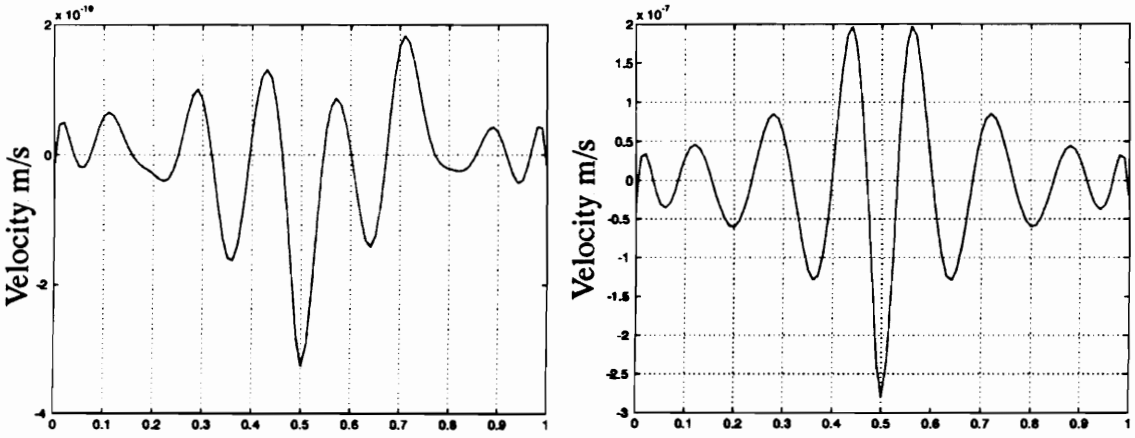

Figure 4.4. Residuals of the real and imaginary velocities between the 1x10 element ESPF model and the analytical model at 4.5 Hz

The real components of the bending moment and shear force are shown in Fig. 4.5. The same four models are plotted in these figures. Variation between the four models in the moment representations can not be visually detected. However, at the center and near the ends of the beam a small variation in the real shear force representations can be identified.

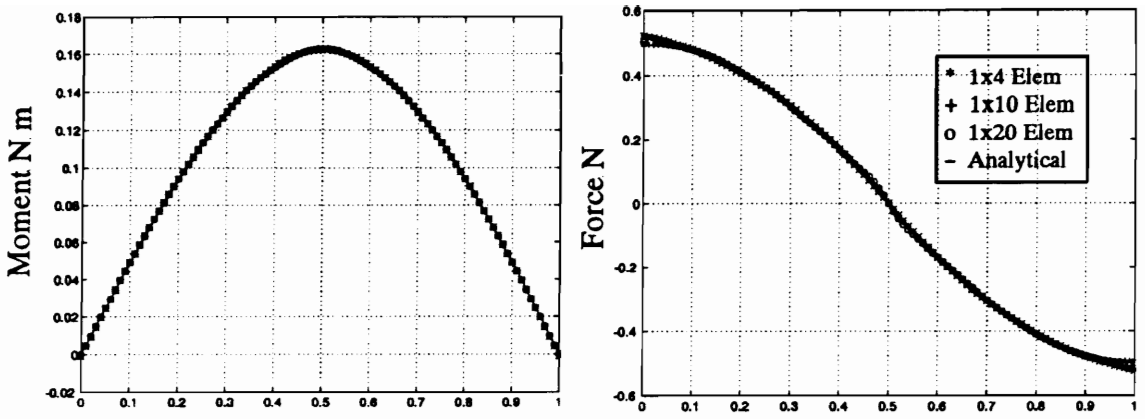

Figure 4.5. Real bending moment and shear force component

Figure 4.6 illustrates the imaginary bending moment and shear force components which were also computed for the same four models. Again, variation is not visually detected in the imaginary bending moment representation and only slight variation near the ends of the beam is detected in the imaginary shear force representation.

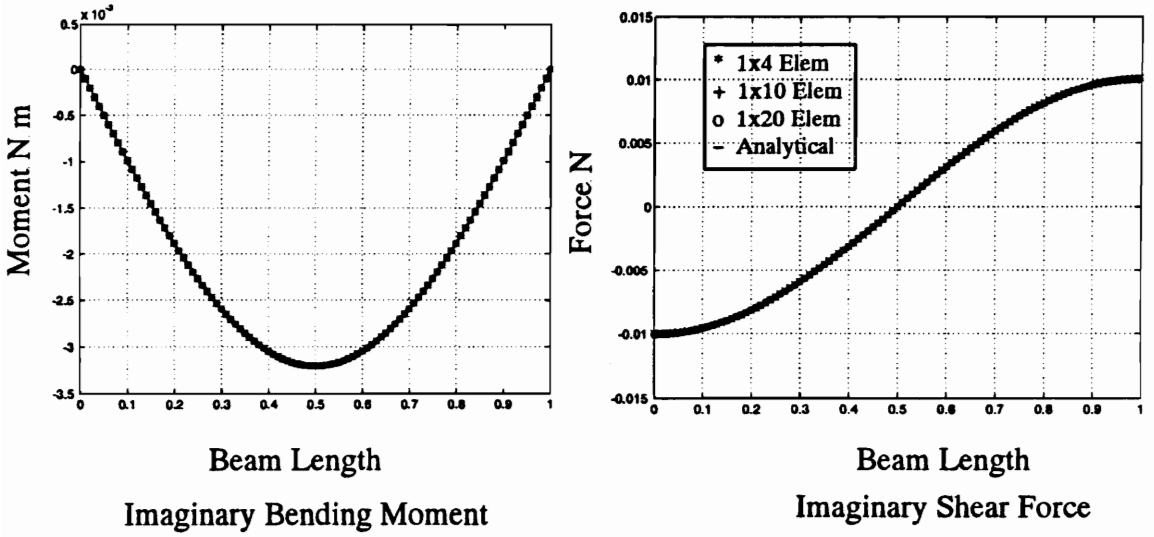

Figure 4.6. Imaginary bending moment and shear force components

Figures 4.7 and 4.8 illustrate the bending moment and shear force residuals computed between the prescribed (Method 2) and the 1x10 element model of Method 3. These figures illustrate that at the center of the beam and near the ends is where the largest differences in the models occur.

The maximum residual in the real bending moment represents a value of 0.125% of the maximum bending moment value. The maximum residual in the real shear force represents a value of 2.80% of the maximum shear force value. The maximum residual in the imaginary bending moment is 0.006% of the maximum bending moment value and the maximum residual in the imaginary shear force is 1.3% of the maximum shear force value. These percentages indicate that extremely accurate models of the generalized forces have been obtained. It is further noted that a significant increase in error is obtained by computing the third derivative in the shear force as compared to the second derivative in the bending moment.

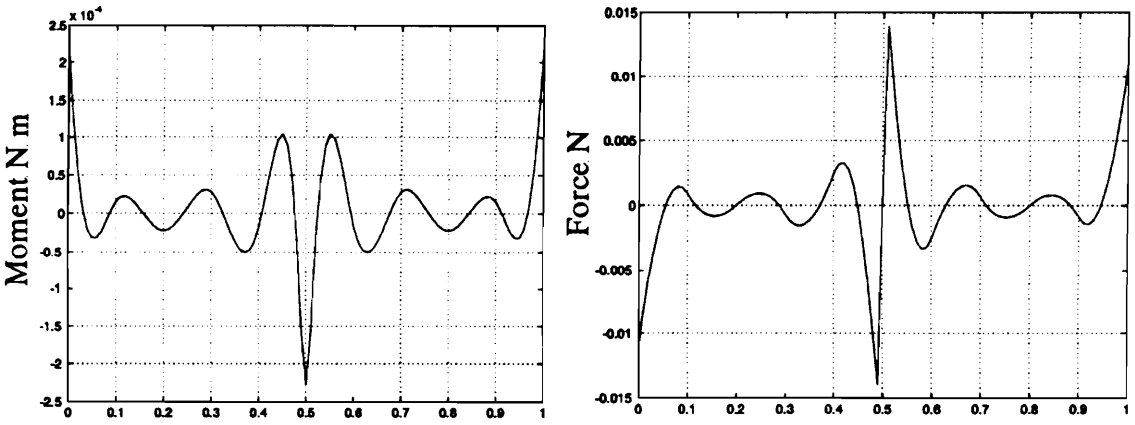

Figure 4.7. Residuals for the real bending moment and shear force components between the 1x10 ESPF model and the analytical model at 4.5 Hz

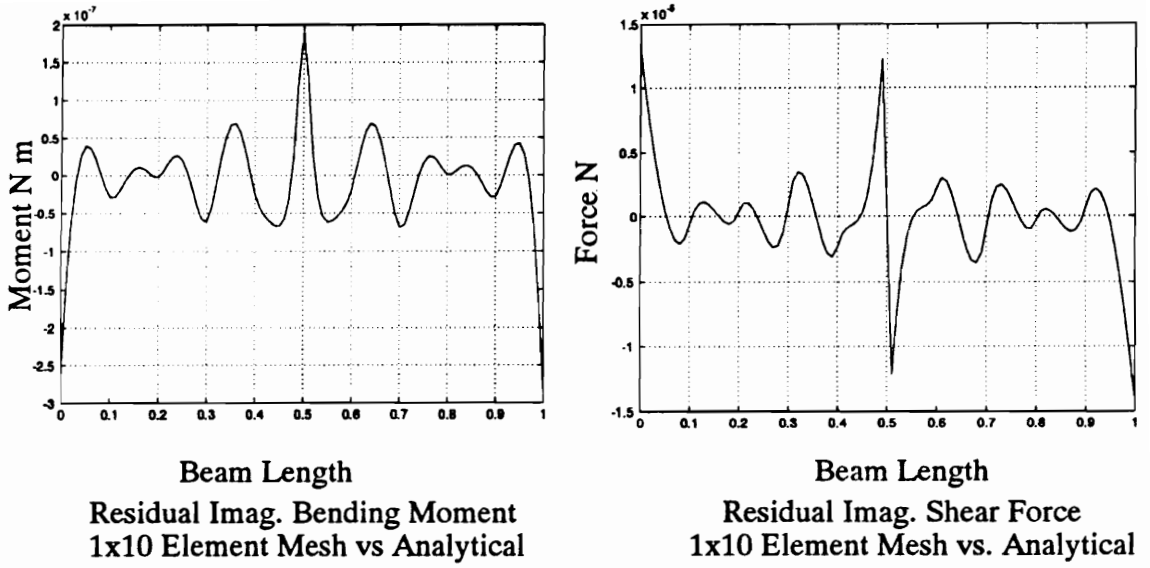

Figure 4.8. Residuals for the imaginary bending moment and shear force components between the 1x10 element ESPF model and the analytical model at 4.5 Hz

Figure 4.9 shows a plot of the power computed by Methods 2 and 3. The solid horizontal line near the top of the plate represents one half of the power entering the system through the shaker as computed by Method 1. Ideally half of the energy entering the system computed by Method 1 would equal the maximum power computed by Methods 2 and 3. The one half comes in because the beam is forced exactly at the mid-span so half of the energy should flow towards the left end of the beam and the other half should flow towards the right end. Figure 4.9 shows that a very good comparison was obtained by the 1x10 and 1x20 element models. The 1x4 element model is not adequate to represent the sharp change in the power at the injection point. The 1x4 element model shows the general trend of decreasing power but does not have real physical significance when it drops below the zero line and then rises back above the zero line. This implies that energy is being generated at the simply supported boundary which is not possible in this model. This plot also clearly shows the importance of converging the power model.

The error between Method 1 and Method 2 at the maximum power location was 1.65%. The error between the maximum power computed by method 1 and the 1x20 element model of method 3 was -6.67%.

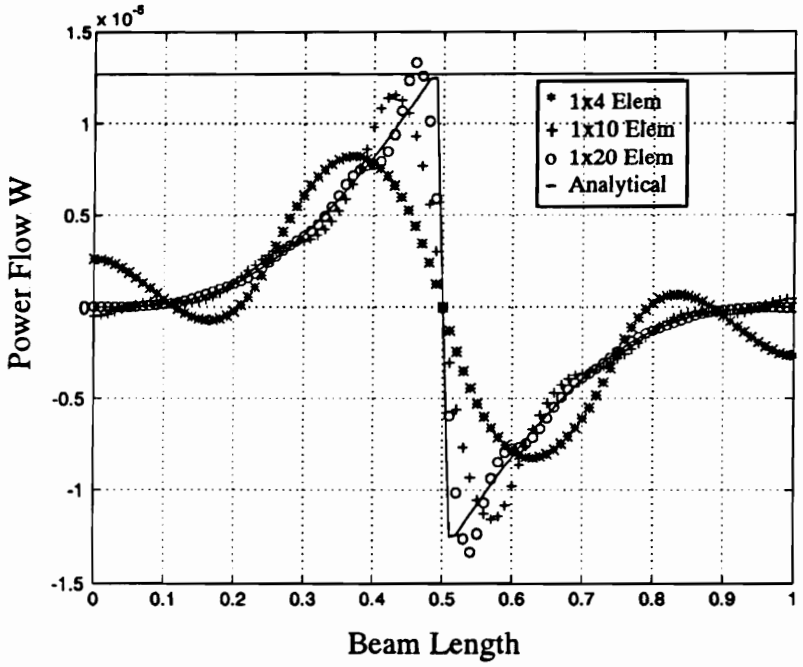

Figure 4.9. Power comparison of 1x4, 1x10, and 1x20 element models

Figure 4.10 illustrates the power residuals between the analytical model (Method 2) and the 1x10 element mesh. It is shown that near the source, significant differences in the power methods exist. However within a length of approximately 0.05 m the results are within about 10%. It is further shown that the simply supported boundary condition of zero velocity at the ends of the beam removes the effects of the larger residuals obtained in the shear force computations at these locations.

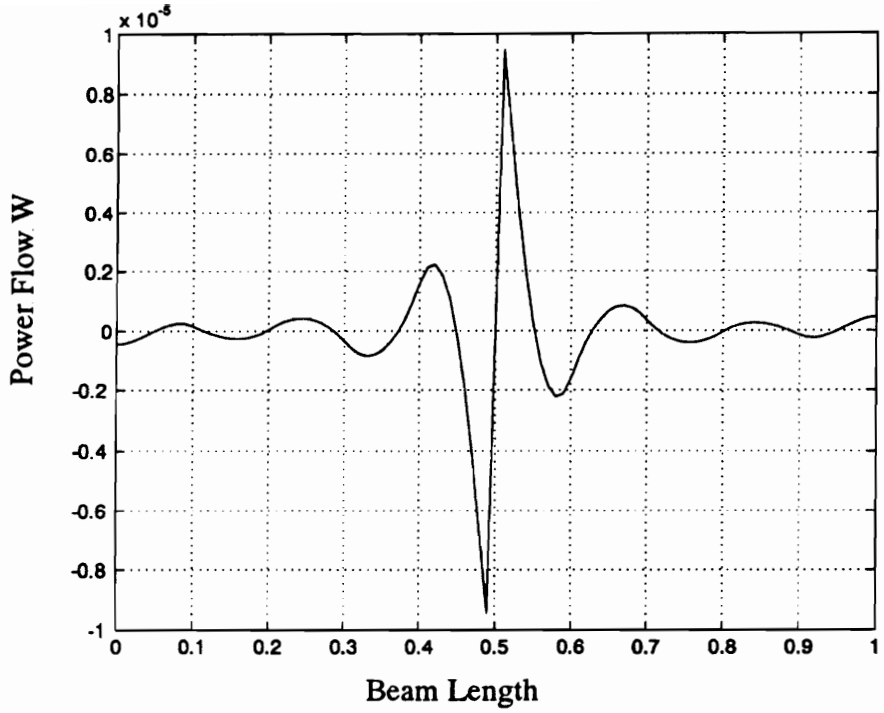

Figure 4.10. Residual power using a 1x10 element model

Table 4.1 summarizes the standard deviation and mean values of the residuals which were computed for each component in the power equation and then for the total power in the structure. The maximum absolute prescribed values for all the components are also listed in the table. The statistics in Table 4.1 can be somewhat misleading and the need for a different error criteria which includes the position along the beam should somehow be included. The values indicate that a real significant improvement in the power computation is not obtained by increasing the number of elements from 4 to 20. However, by spatially plotting the results as shown in Fig. 4.9, significant improvements in the power model were indeed obtained.

Table 4.1. Power component residual statistics for the beam power models

Power Comp.	1x4 Element Model		1x10 Element Model		1x20 Element Model		Max. Abs. Pres. Value
	Std.	Mean	Std.	Mean	Std.	Mean	
Real Velocity (m/s)	5.3e-9	1.8e-10	9.2e-11	-5.0e-12	8.9e-11	1.5e-11	0.0014
Imag. Velocity (m/s)	6.9e-7	-1.3e-8	8.6e-8	-7.4e-10	7.2e-9	-7.2e-9	0.0679
Real Moment (N m)	2.2e-4	-4.8e-5	6.0e-5	7.0e-6	1.4e-5	-2.4e-7	0.1629
Imag. Moment (N m)	1.6e-6	3.6e-7	6.2e-8	8.4e-9	1.7e-8	-1.1e-10	0.0032
Real Shear Force (N)	6.9e-3	-1.5e-5	3.6e-3	2.0e-6	1.6e-3	2.1e-4	0.5006
Imag. Shear Force (N)	4.1e-5	2.9e-8	3.7e-6	-2.7e-8	1.6e-6	-3.6e-8	0.0101
Power (W)	3.2e-6	3.3e-11	1.9e-6	-6.4e-11	1.1e-6	-5.4e-11	1.25e-5

In summary, the results of three independent methods of computing the power in a simply supported beam were compared. Method 1 computed the power entering the beam through the applied force by integration of the injected power. Method 2 computed analytical derivatives of the velocity equation from which the components of the power were computed. In Method 3, the ESDM technique used simulated laser data to solve for the velocity field. The ESPF method was then used to compute the power.

It was shown that a significant number of elements in Method 3 were required in order to match the spatial location of the input power computed from Methods 1 and 2. However, away from the source it was shown that as few as 10 elements in a 1 m beam provide a very

good power model. It can further be concluded that the ESPF method is capable of both computing the magnitude and the spatial locations of any sources or sinks in a simply supported beam. With the high quality of the results obtained from beam models the next step is to investigate power in plates.

4.2 ESPF Plate Validation

The purpose of this section is to show that the ESPF method is capable of accurately computing the power in plates. First the plate setup and parameters will be presented followed by the results of the validation process. The same validation process performed in the previous section for beams is presented in this section for plates.

4.2.1 Plate Setup and Parameters

The plate setup consisted of a uniform rectangular simply supported plate which was forced at the center with a magnitude of 5.0 N/m^2 at a frequency of 12.0 Hz. The general setup of the plate and the model parameters are shown in Fig. 4.11. The small square shaded area on the plate represents the area over which the uniformly distributed harmonic load was applied.

Simply Supported Plate On All Sides

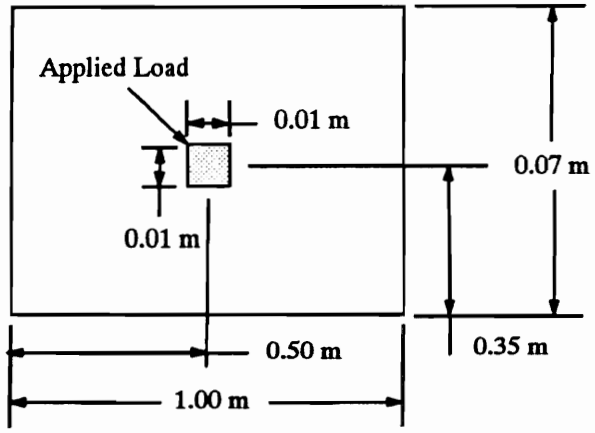

Model Parameters

Young's Modulus	2.040×10^{11} Pa
Damping Factor	0.001
Length	1.000 m
Width	0.700 m
Thickness	0.002 m
Force Magnitude	5.0 N/m^2
Frequency	12 Hz
Density	7869.0 kg/m^3
X_1	0.490 m
X_2	0.510 m
Y_1	0.340 m
Y_2	0.460 m

Figure 4.11. Plate setup and model parameters

4.2.2 Validation Methods

The same three methods used in the beam validation process were used to validate the ESPF method for plates. Method 1 consisted of a purely analytical power computation as defined by Eq. (3.89). Method 2 was based on derivatives of the velocity field given by Eq. (3.87). Method 3 was based on the ESDM velocity solution obtained from simulated laser data.

4.2.3 Method Comparison

The first test compared the injected power computed from Eq. (3.89) to the analytical power computed from the derivative approach of Method 2. The theory behind this test is that the power injected over an area, should equal the power that is leaving the area minus the power that is dissipated in the area. If the area over which the power is injected is small, and if structural damping is small, the amount of power dissipated in the forced area would also be small, and would result in very slight differences if neglected when the two power computations are compared. The goal of this test was to verify that the power method of com-

puting the generalized forces from spatial derivatives of the displacement field is valid for plates.

The power injected into the plate, using the derivative approach to compute the power was performed by computing the power at 10 points along each side of the rectangular applied load which is shown by the shaded area in Fig. 4.11. The power at these points was summed to give the total power crossing the boundary on each side of the force. Due to this discretization, and the fact that Method 1 computes an exact integral, some difference between the results from Methods 1 and 2 is expected. Also, as previously mentioned, neglecting the power dissipated over the area where the force is applied will cause some differences in the two results.

The series summation indices, m and n were each summed from 1 to 40 for a total of 1600 terms in the summation of Eq. (3.89) and in the summation required to compute the velocity field used in Method 2. It was verified that a significant number of terms was required in order to obtain a good approximation of the force over the given area.

Figure 4.12 shows a plot of the percent error between the power computed by these two methods. The largest percent error is shown to occur at a frequency of approximately 14 Hz. The resonance frequencies have been marked with solid straight lines and do not correspond to the peak differences in the power computations. It is further noted that the mean error is a positive value which implies that the power computed using the derivative formulation predicts a slightly higher value than the power computed from Eq. (3.89) at most frequencies. Considering the approximations mentioned, and the fact that the maximum error between the two methods was 2.1%, it was determined that computing the power from derivatives of the displacement field is a valid approach for plates.

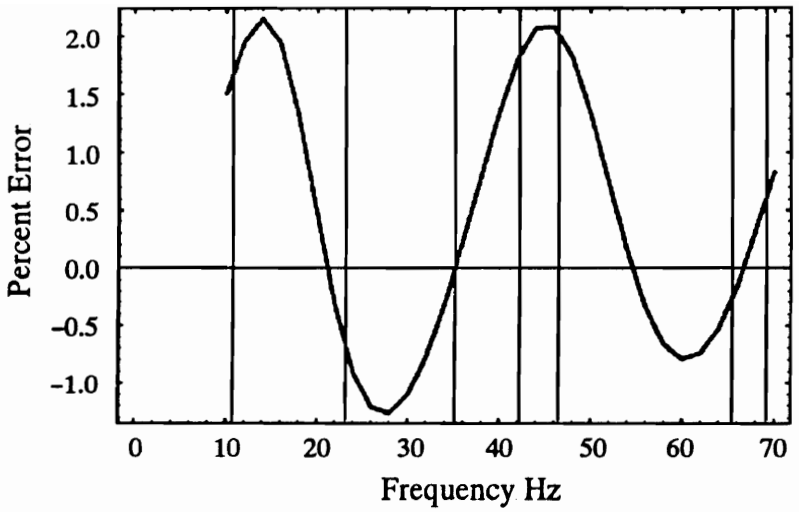

Figure 4.12. Percent error in injected power between Methods 1 and 2

A second test was performed after determining that Methods 1 and 2 provide very similar results of the power entering the system. The second test consisted of comparing the power model from the pure analytical case, (Method 2), in which the derivatives of the analytical solution were used to compute the power, to the power model obtained from using simulated laser data, (Method 3). To perform this test the same simply supported plate analyzed in the previous test was used.

To effectively compare Methods 2 and 3, it was determined that the main area of interest would be at a source or sink. Therefore, each of the two methods were used to compute the power normal to a circle, centered around the source. In other words, the net power crossing the circular control volume, centered at the source, was computed. This control volume was then incrementally enlarged and the power crossing the control volume at each increment was computed.

As previously mentioned, the force on the plate was applied over the area between 0.49 m and 0.51 m in the x direction and between 0.34 m and 0.36 m in the y direction. Figure 4.13 illustrates the spatial relation of the control volumes or rings to the area over which the

force is applied. The area over which the force is applied is shown by the lightly shaded rectangular area in Fig. 4.13. Figure 4.13 indicates that the first two control volumes are inside the forced area. This implies that if more power is being injected into the system than is being dissipated over the forced area, theoretically, the power should continue to increase up to the third control volume. The power was computed at 72 points in each control volume resulting in an angular increment of 5 degrees between each point. A total of 69 control volumes at radial increments of 5.0 mm were used. This covered a radial distance of 0.345 m which is nearly the entire width of the plate. Only the first 5 control volumes are shown in Fig. 4.13.

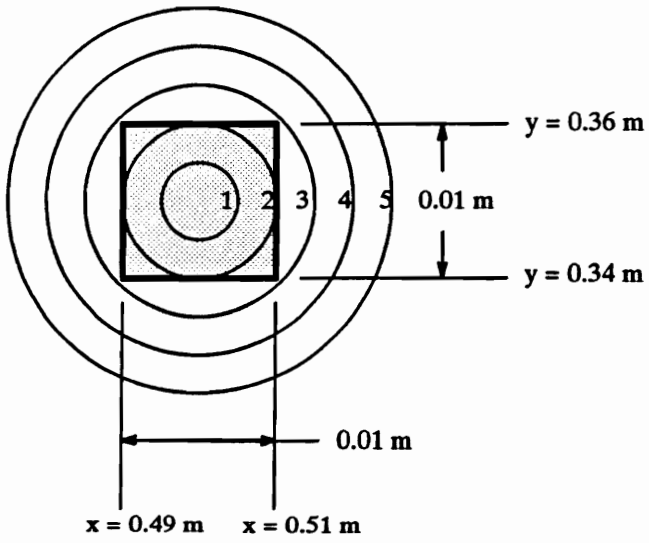

Figure 4.13. Sketch of forced area and control volume locations

Figure 4.14 shows two plots of the power computed for this test. The first figure illustrates the purely analytical case and the second figure illustrates the simulated laser data case with a 12x12 element mesh. These plots were made on the same scale.

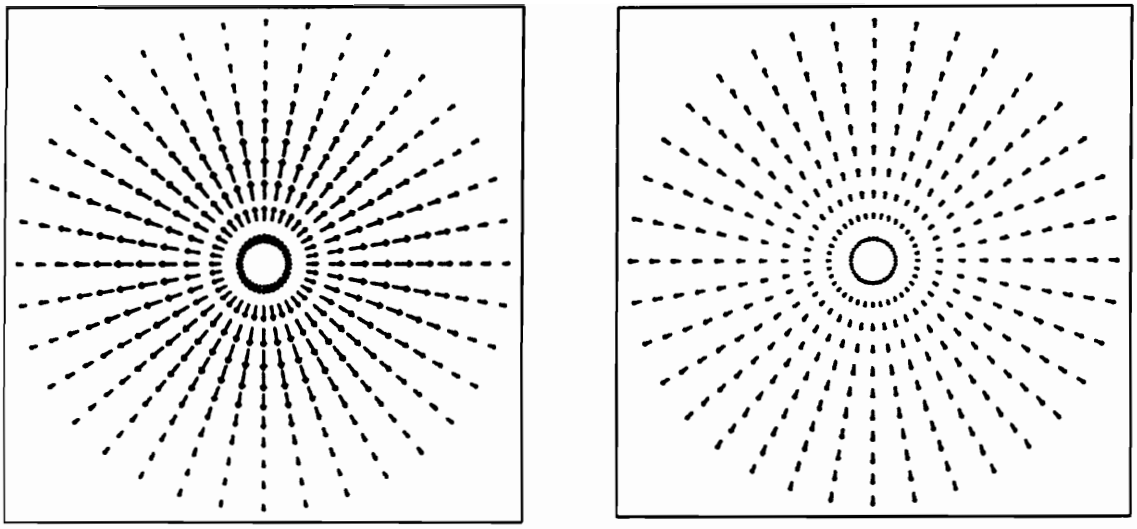

Prescribed Power Flow (Method 2) Simulated Power Flow (Method 3)

Figure 4.14. Concentric power rings

Each control volume (ring) in Fig. 4.14 represents a radial increment of 0.005 m. Since 11 rings are shown in each figure the outer diameter of the rings shown represents a length of 0.11 m. By visually comparing the two models in Fig. 4.14 it is shown that more power is in the first 7 or 8 rings in the prescribed power model than in the simulated power model. However, in the outer rings shown in Fig. 4.14, the simulated power model indicates more energy compared to the outer rings in the prescribed power model.

To better illustrate the difference between these two methods the total energy in each ring was computed. This was done by summing up the power normal to the control volume at 72 equally spaced points. This sum was then divided by the number of points in the sum (i.e. 72) and multiplied by the ring circumference. This gave the total power in each ring in units of watts.

Figure 4.15 illustrates the power in each ring for 4 different power models. The 4 models consist of the prescribed analytical case (Method 2), a 4x4, a 10x10, and a 12x12 element model using the simulated laser data approach of Method 3. This plot indicates that the maxi-

mum power in the prescribed, 10x10 element, and 12x12 element models compared very closely in magnitude. The percent error between the maximum power computed by the 12x12 element model and the analytical model was 1.33%. The 4x4 element model computed a maximum power approximately 10% lower than the other models.

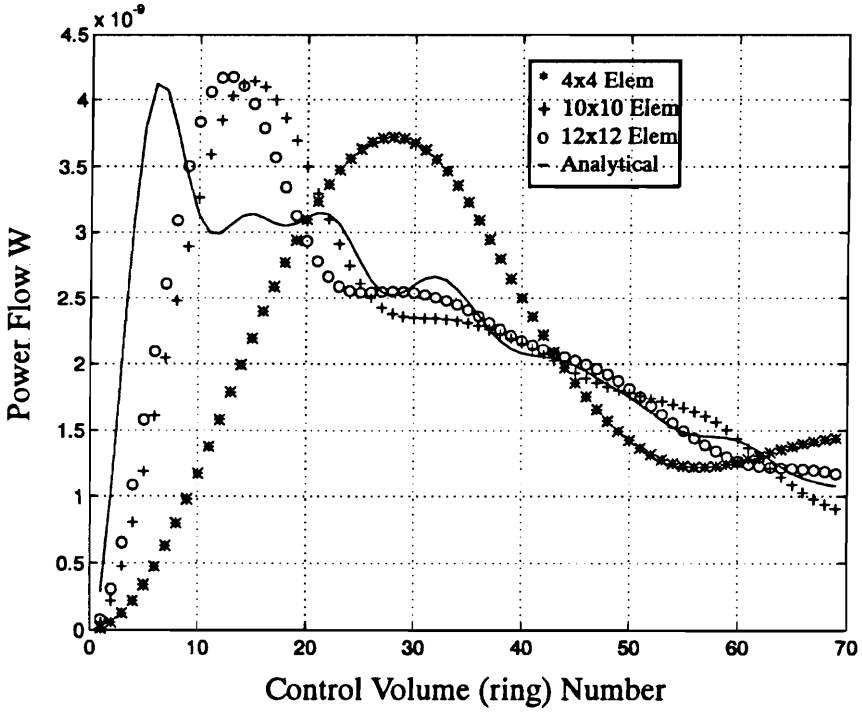

Figure 4.15. Power in each control volume

The largest differences between the four power representations are the spatial locations in which the maximum power is computed. It is shown by the prescribed model that the maximum power is reached relatively quickly (ring 5) and then begins to dissipate as the distance from the force is increased. In the simulated laser data models of Method 3, the location of maximum power is reached considerably further away from the source (ring 11) as compared to the analytical case. This is explained by the different representations of the force between the two models. In Method 2, a purely analytical representation of the force is obtained. This results in a very sharp, almost discontinuous representation of the shear force. In Method 3,

using simulated laser data to solve for the velocity field, from which derivatives were taken to obtain the shear force, results in a smoother shear force representation. Therefore, it appears as though the source acts over a larger area than is actually the case. This gives rise to some concern to the methods of representing the velocity field and hence the shear forces in the plate. Other methods of representing the velocity field such as cubic B-splines and higher order polynomials have been investigated. However, none of these methods were shown to yield a better representation of the shear force. The direct dynamic stiffness method is another possible method for representing the velocity field which has not been fully investigated.

The decrease in power, after the maximum power has been reached, is not due to an increase in the area because a flux is not being computed. The decrease is due solely to a dissipation in the material by structural damping. Other typical loss factors such as acoustic radiation are not modeled in either Method 2 or 3 and therefore do not account for any of the power loss.

In the analytical model, it is shown that immediately after the peak, the power levels off for about 10 ring increments before beginning a steady decline. By looking closely at the 10x10 and 12x12 element models this same phenomena is also detected. Finally, it is noted that at approximately the twentieth ring increment which corresponds to a radial distance from the source of 0.100 m the analytical model and the 10x10 and 12x12 element models become very close.

In summary of test 2 for the plate, it can be concluded that by using a significant number of elements in the model, the magnitude of the power converges to the pure analytical model. It was further shown that as the number of elements is increased the model converges to the analytical case. However, near the source, the ESPF method used in Method 3 results in significant error in the spatial representation of the maximum power.

The third test used for validating the ESPF method consisted of computing the residuals between the pure analytical model (Method 2) and the simulated laser data model (Method 3) with a 10x10 element mesh. Again the same simply supported plate used in the previous 2 tests was used. From the previous 2 tests it was illustrated that "good" power results could be obtained using the ESPF method with a uniform mesh except near a power source or sink. The goal of this test was to investigate the ability of the ESPF method to compute the power over the entire surface of the structure with the understanding that near a source or sink significant error could be present.

Figure 4.16 shows plots of the residuals between the real and imaginary velocity fields of the two models. These plots clearly show significant differences in a narrow strip in the middle of the plate in the x direction and a slightly less obvious difference in a narrow strip in the middle of the plate in the y direction. These differences are due to the Fourier series representation used in both methods. This figure clearly indicates that the force representation as seen by the analytical model of Method 2 and the simulated laser data model of Method 3 are significantly different. It is further noted that apparently very good results were obtained along the boundary of the plate. The maximum absolute real and imaginary transverse velocity components were 3.38x10–6 m/s and 2.06x10–4 m/s respectively.

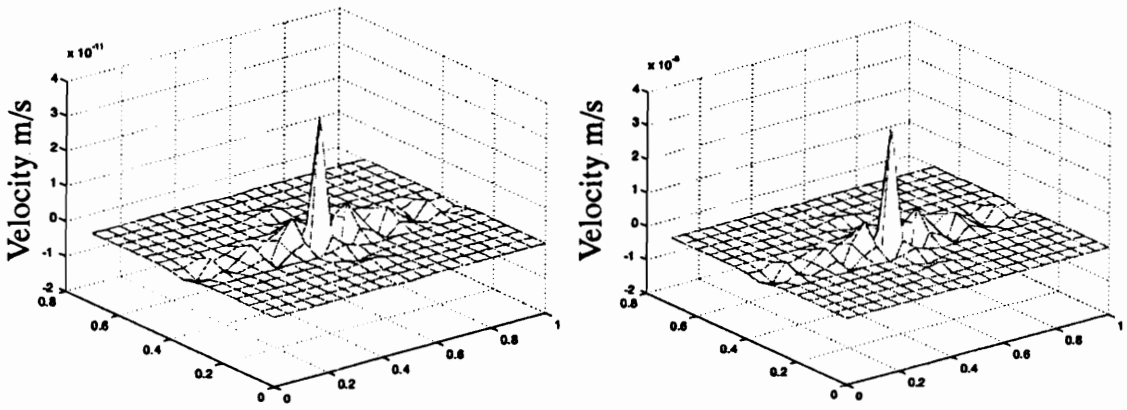

Real Velocity Component Imaginary Velocity Component

Figure 4.16. Real and imaginary velocity residuals between Methods 2 and 3

Figure 4.17 shows residual plots for the real and imaginary shear force in the x-z direction. Again the differences in the two models, due to the representation of the force, is made evident. It is also noted that at the boundaries of the plate the representation is not as good as it appeared to be in Fig. 4.16.

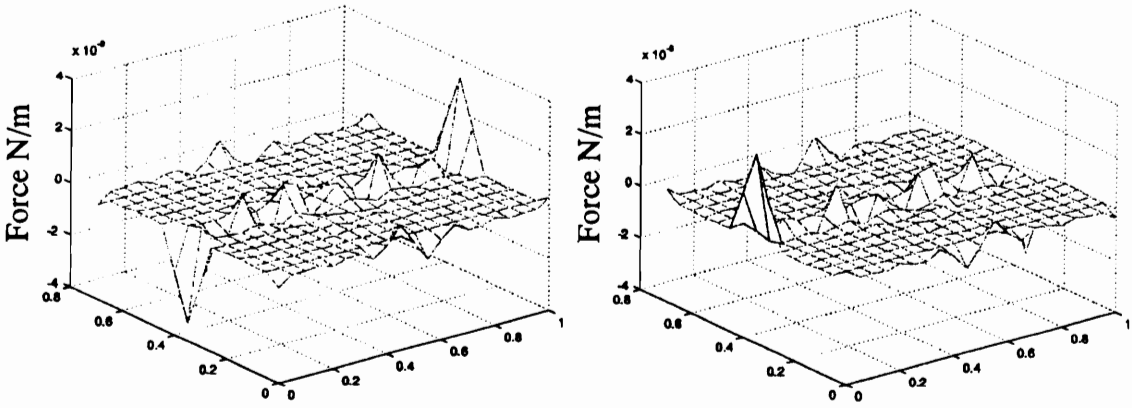

Real Shear Force

Imaginary Shear Force

Figure 4.17. Real and imaginary shear force residuals in the xz direction between Methods 2 and 3

Figure 4.18 represents the pure analytical model of the power as computed by Method 2. and the 10x10 element model obtained by Method 3. The location of the source is clearly identified in both figures. The ESPF solution illustrates a more symmetric distribution of the power around the source. In other words, the 8 power vectors surrounding the source appear to be much more uniform in size than the 8 power vectors surrounding the source in the analytical model of Fig. 4.18. This difference develops due to the ability of the pure analytical model to obtain a better representation of the force and boundary conditions. In Method 2, the boundary conditions are hard coded into the power solution, and hence, due to the geometry of the plate, Method 2 predicts that more energy will flow along the longer dimensions (i.e. the length) of the plate as opposed to the shorter dimensions (i.e. the width). It can be thought of as Method 2 being able to see the potential down stream for power dissipation and

reacting accordingly by sending more power to the areas of greater dissipation potential. This is somewhat similar to a heat conduction type problem where more heat flow is obtained in areas of greater temperature difference or potential. On the other hand, the ESPF method computes a more uniform representation of the power because the boundary conditions have not been hard coded into the solution, they are solved for by the ESDM technique. In this case, the boundary conditions do not effect the power solution as strongly and results in a more smooth power representation.

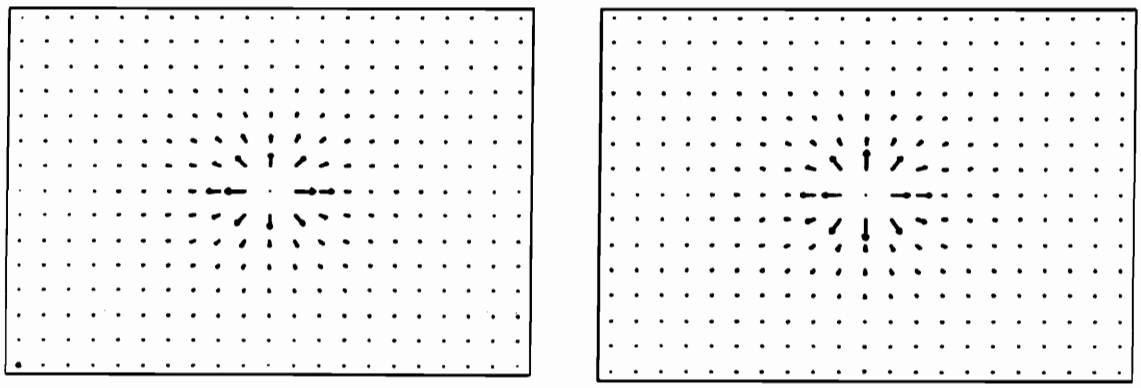

Prescribed Power Flow (Method 2)

Simulated Power Flow (Method 3)

Figure 4.18. Power-flow vector plot of the entire plate

At first, the inability of the ESPF method to determine the boundary conditions to very high precision appears to be a drawback. However, under real test conditions, the true boundary conditions are unknown and can not be hard coded into a solution. Therefore, some form of representing the field must be used, and as shown by the residuals represented in Figs 4.16 and 4.17 the quintic B-spline representation used in this research performs very well.

Figure 4.19 shows the residuals between the two power-flow vector plots of Fig. 4.18. A magnification factor of 4 was used to magnify the residual error in the plot as compared to the scale in Fig. 4.18. Again in this residual plot, the effects of the finite series representation of the force are apparent. The two strips of high residual error in the center of the plate

in both the x and y directions can be identified. The large residuals near the boundaries of the plate that were obtained in the shear force representation shown in Fig. 4.17, have been nullified in the power-flow computations due to the zero velocity at the boundary. However, in the center of the plate these errors are amplified due to the large velocities.

The maximum power values in Fig. 4.18 are 9.95x10–9 W/m and 1.11x10–8 W/m in the x and y directions respectively. The maximum residuals shown in Fig. 4.19 are 1.63x10–9 W/m and 3.73x10–9 W/m in the x and y direction respectively. The mean and standard deviations of the power residuals are respectively 2.88x10–15 W/m and 2.29x10–10 W/m in the x direction and 1.33x10–13 W/m and 4.03x10–10 W/m in the y direction.

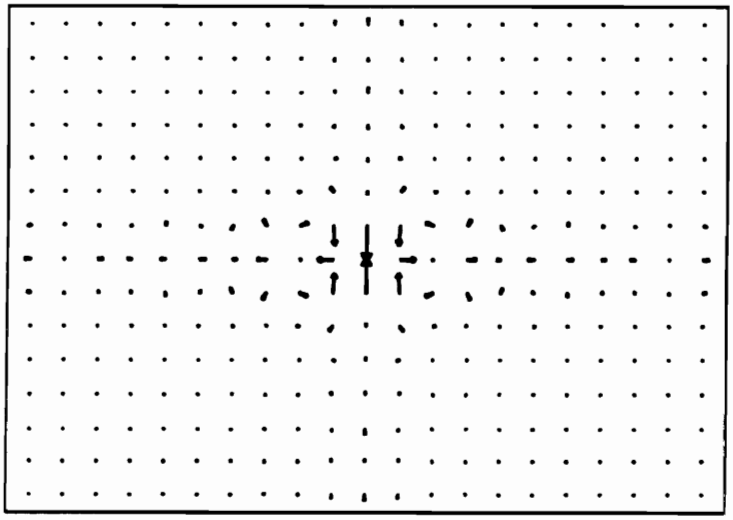

Figure 4.19. Residuals of the power-flow vector plot of the entire plate

Table 4.2, is a summary of the standard deviation and mean values of the residuals between Method 2 and Method 3 for all the components used to compute power in plates. The standard deviation and the mean of the residuals between the analytical model of Method 2 and the 4x4, 10x10, and 12x12 element models of Method 3 are listed. The maximum absolute values of the prescribed model are also presented to aid in the significance of the standard deviation and mean values.

Table 4.2. Statistics for plate power models

Power Component	4x4 Element Model		10x10 Elem. Model		12x12 Elem. Model		Max. Abs. Pres. Value
	Std.	Mean	Std.	Mean	Std.	Mean	
Imag. Ang. Vel. x (rad/s)	1.19e-6	-3.32e-11	1.59e-7	5.68e-12	8.10e-8	-7.34e-12	6.63e-4
Imag. Ang. Vel. y (rad/s)	6.77e-7	-2.88e-9	8.35e-8	1.73e-10	5.96e-8	-9.64e-11	9.36e-4
Imag. Mom. x (N)	3.54e-8	-2.12e-9	1.69e-8	1.45e-9	1.23e-8	-8.40e-10	5.27e-5
Imag. Mom. y (N)	3.50e-8	5.15e-9	1.34e-8	1.00e-9	9.24e-9	-8.95e-10	7.70e-5
Imag. Shear Force xz (N/m)	9.23e-7	-2.41e-12	5.97e-7	1.10e-10	3.88e-7	4.78e-11	3.13e-4
Imag. Shear Force yz (N/m)	1.05e-6	6.73e-9	6.61e-7	1.04e-9	4.92e-7	-1.21e-9	4.48e-4
Imag. Vel. z (m/s)	2.89e-8	-1.16e-9	4.37e-9	8.61e-11	2.83e-9	-1.42e-11	2.06e-4
Real Ang. Vel. x (rad/s)	8.12e-10	4.28e-14	1.59e-10	2.68e-14	8.10e-11	7.24e-14	1.06e-5
Real Ang. Vel. y (rad/s)	6.29e-10	3.94e-12	8.35e-11	2.17e-13	5.95e-11	-1.68e-13	1.51e-5
Real Mom. x (N)	4.80e-5	1.07e-5	1.69e-5	-1.40e-6	1.24e-5	8.57e-7	3.04e-3
Real Mom. y (N)	3.98e-5	8.97e-6	1.34e-5	-9.17e-7	9.45e06	9.23e-7	4.46e-3
Real Shear Force xz (N/m)	1.21e-3	2.99e-8	5.95e-4	-2.16e-8	3.89e-4	2.51e-8	1.97e-2
Real Shear Force yz (N/m)	1.22e-3	5.86e-6	6.57e-4	-9.25e-7	4.96e-4	8.87e-7	2.77e-2
Real Vel. z (m/s)	2.12e-11	-2.10e-14	4.36e-12	9.78e-14	2.83e-12	-6.06e-14	3.38e-6

In summary, it can be concluded that the theoretical development of the ESPF method has been rigorously tested and validated for both beam and plate models. From these analytical experiments a strong relation between the beam and plate results was noted. Using simulated laser data the ESPF method performed exceptionally well for beam models both in computing the magnitude and spatial location of the power along the beam. In the plate models, accurate representation of the power magnitudes were obtained but spatial error occurred primarily due to the differences in the representation of the force between the pure analytical model and the simulated laser data model. It appeared as though the ESDM solution for the velocity field results in a smoother representation. This is illustrated by the differences in the shear forces computed between the two models. The pure analytical model was able to represent the shear force as a sharp peak whereas in the ESPF approach, the shear force had a much smoother representation. This is expected for C^2 continuity of the shear force using quintic B-splines. It is further concluded from this analytical work that the ESPF method is capable of providing accurate power results and is in a state ready for experimental data.

Chapter 5

Experimental Results

5.1 Introduction

The goal of this chapter is to illustrate the capabilities of the ESPF method. It will be shown that the ESPF method provides an accurate spatial model of the power in the structure and that the power injected and absorbed by external sources is conserved. It will further be shown that the maximum power magnitudes computed by the ESPF method compare to within 20% of the injected power computed by two other methods. The two other methods only compute the power injected into the structure based on data obtained from the impedance heads. These two methods do not compute a spatial map of the power in the structure.

This chapter first describes the experimental setup of the approximated simply supported plate used in the experiment. The results obtained from the ESDM velocity-field solution and the ESPF method are then presented and discussed. The results at forcing frequencies of 79.0 Hz, 311.0 Hz, 909.0 Hz, and 1110.0 Hz will be investigated.

5.2 Experimental Setup

This section details the experimental setup of the approximated simply supported plate. The ESPF approach was applied to a 380 mm x 300 mm x 1.6 mm steel plate. It was assumed

that the plate had a Young's modulus of elasticity of 2.04×10^{11} Pa, structural damping factor of 0.001, and Poisson's ratio of 0.29. These are average values found in any table of material properties for mild steel.

The test plate was mounted to a rigid steel frame by thin steel shims as shown by Fig. 5.1. Five screws, equally spaced along each edge of the plate, were used to attach the plate to the shims. The plate was also glued to the shims to help support the screws. However, due to the brittle nature of the glued joints, some of the glued sections broke free, as will be indicated by the results.

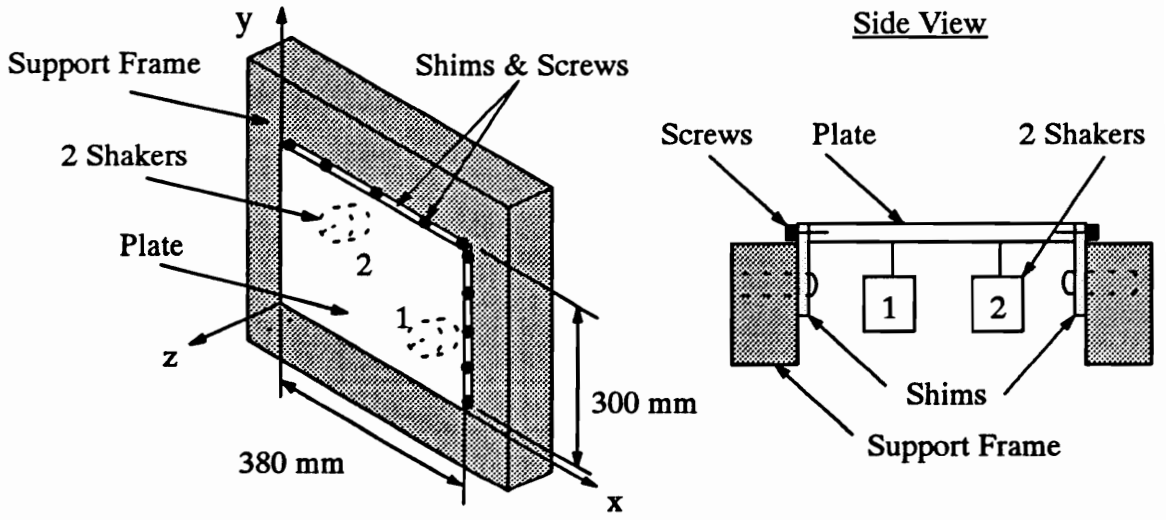

Figure 5.1. Simply supported plate design schematic

The test structure was designed to simulate a simply supported plate. However, this assumption is not made or required in any part of the ESPF modeling process as the boundary conditions are inherently modeled and solved for in the ESDM velocity solution based on the laser data. However, an assumed mechanics model which expresses the generalized forces in terms of the displacements is required. In this research Love-Kirchoff plate theory was assumed as discussed in Chapter 3.

The steel plate was harmonically excited with two electromagnetic shakers. The shakers were hung from bungee cords and connected to impedance heads. The shakers were freely hung from bungee cords to reduce any moment generation at the connection to the plate. Foam pads were placed along the sides of the shakers to prevent any swaying during the test.

Impedance heads were connected to the plate through 2.0 cm diameter mount plates which were glued to the plate. Shaker 1, was attached to the plate at x=290 mm ±2 mm, y=90 mm ±2 mm. Shaker 2 was attached at x=90 mm ±2 mm, y=210 mm ±2 mm. The accuracy to which these values are known will be shown to be extremely important in the 909.0 Hz case. The reason that these values could not be more precisely measured is that the actual mounting of the impedance heads took place after the plate had been connected to the shims and placed in the heavy steel support frame.

Figures 5.2 and 5.3 show the backside of the plate setup. In Fig. 5.2, the rigid steel frame and the hex screws which connect the shims to the rigid steel frame are shown. The PCB model U288C01 impedance heads are also shown. The measuring tape allows the relative positions of the mount plates to be roughly determined. Figure 5.3 shows the shakers as they are being shifted and aligned into place for testing.

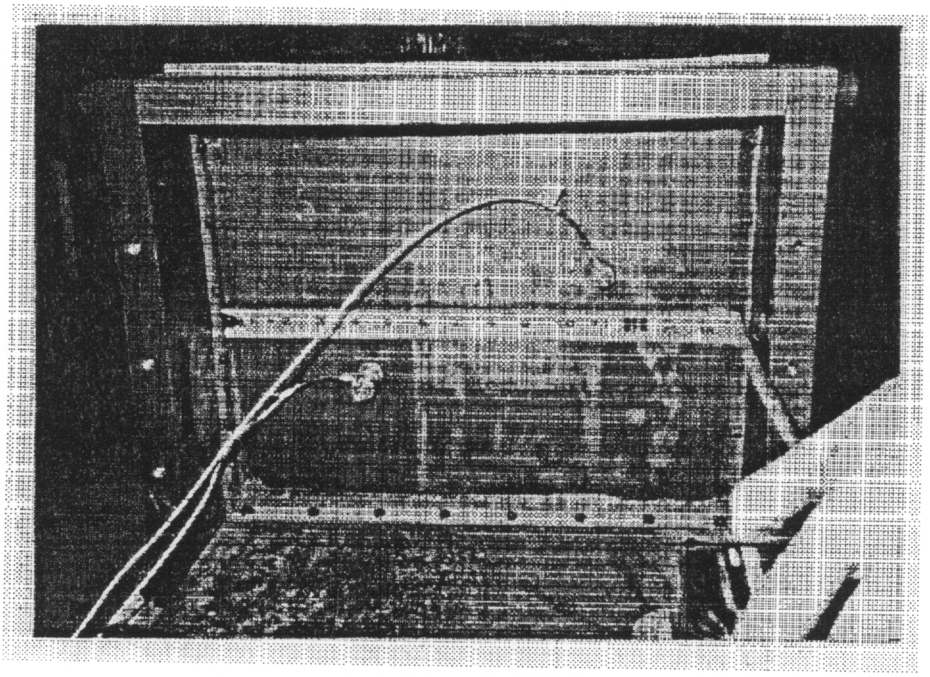

Figure 5.2. Photograph of the impedance head locations

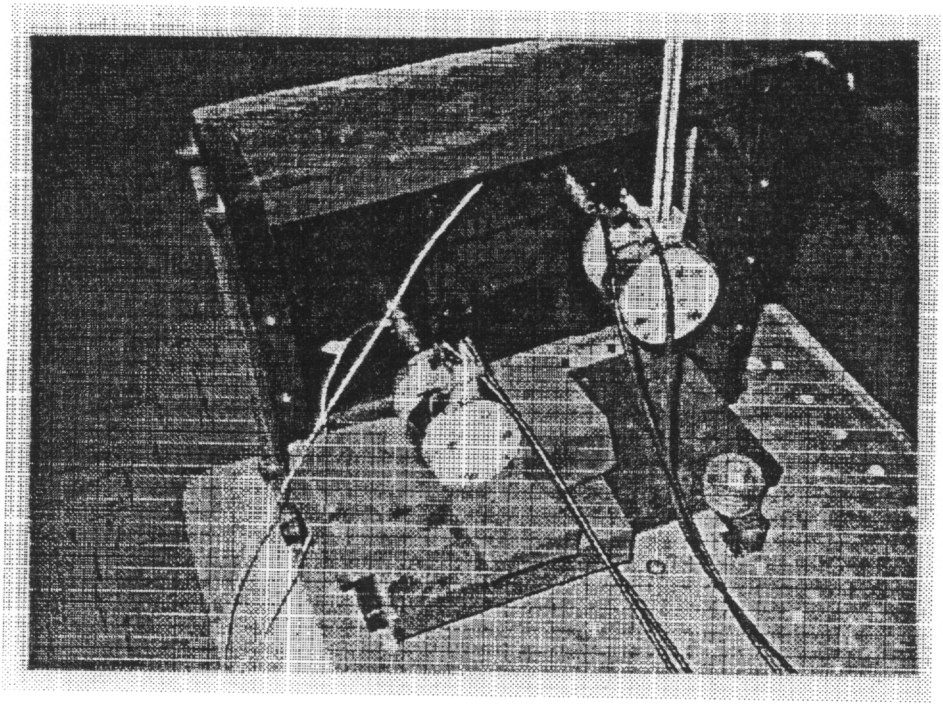

Figure 5.3. Photograph of the heavy steel frame and the shaker setup process

Figure 5.4 shows a 1/10 scale drawing of the plate and the impedance head mount plates. The registration points are not shown to scale as these points were marked as small as possible to improve the registration accuracy. The registration points were spread out near the edges of the plate to also help improve the laser registration results. The accuracy with which the registration points were measured was approximately ± 0.5 mm. The registration points were much easier to measure accurately compared to the impedance head mount plates because they are on the front side of the plate. All dimensions shown represent nominal values in millimeters and are measured from the lower left corner of the plate which has been defined as the origin of the structure coordinate system.

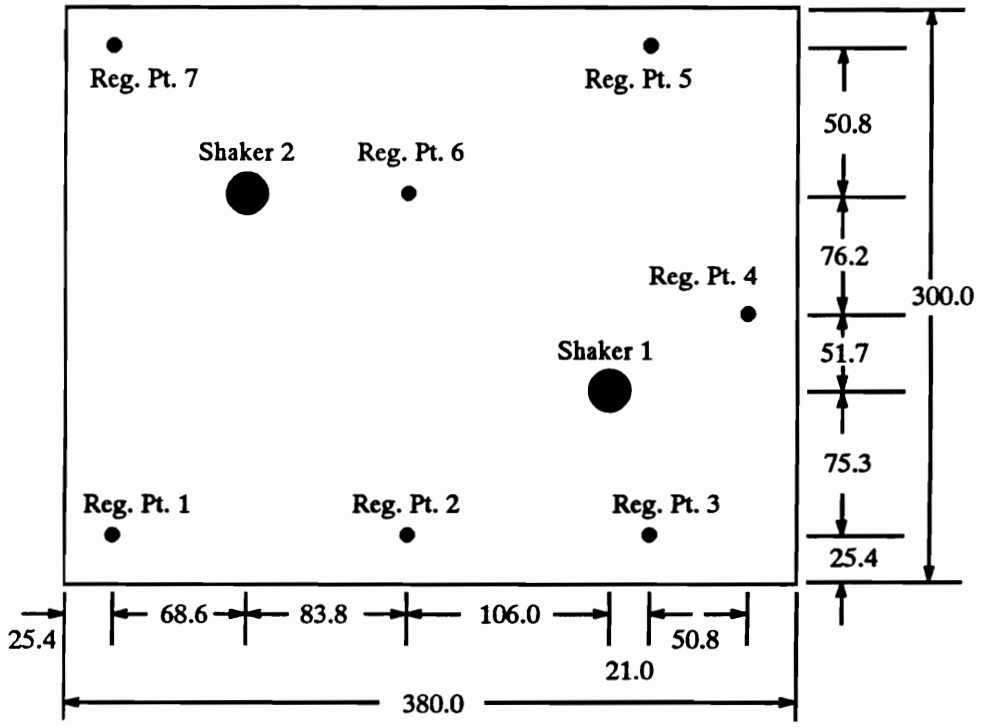

Note: All dimensions are in mm

Figure 5.4. 1/10 Scale drawing of shaker locations and registration points

5.3 Test Procedure

Three methods of computing the power in the plate were compared to validate the ability of the ESPF method to conserve energy and provide quantitative power results. This section presents the three methods and discusses the significance of comparing the results computed from these methods.

Method 1 consisted of using the ESPF approach. As previously mentioned, this entails scanning the structure with the SLDV, using the experimental data to solve for the velocity field, from which the generalized forces, and the power are computed.

Method 2 consisted of computing the power injected into the plate through the two shakers by collecting force and acceleration measurements from the two impedance heads during the scanning process. These signals were represented by the time signal model discussed in Chapter 3, and the injected power was computed as shown by Eq. (5.1) [51]. In Eq. (5.1), F_r,V_r, F_i, and V_i represent the real and imaginary components of the force and velocity time signal models respectively.

$$P_{injected\ Method2} = \frac{1}{2}\left[F_r V_r + F_i V_i\right] \tag{5.1}$$

Method 3 is a common technique and has been used extensively in the literature [26][54]. It consists of computing the power injected into the plate through the two shakers by computing the cross spectrum of the force and acceleration signals from the impedance heads as shown by Eq. (5.2) [55]. In Eq. (5.2), ω is the forcing frequency, and $\mathrm{Im}\left\{G_{fa}\right\}$ is the imaginary component of the cross spectrum of the force and acceleration.

$$P_{injected\ Method3} = \frac{\mathrm{Im}\left\{G_{fa}\right\}}{\omega} \tag{5.2}$$

Given the same input, it was verified that Methods 2 and 3 produce identical results. However, in this experiment, the signals in Method 2 were filtered and sampled using an Iotech ADC488/8S A/D converter and a Silicon Graphics workstation. In Method 3, the data was fed directly into an HP 35665A Dynamic Signal Analyzer. The data for Method 2 was acquired during the scanning process, while the data used in Method 3 was acquired after the scanning process had been performed to show repeatability of the experiment. Since the data acquisition methods of Methods 2 and 3 are completely independent and the data was collected at different times it should be realized that slight differences in the results will occur.

All three methods are based on different transducers or data acquisition processes which will inevitably cause some differences in the results. It is further noted that the ESPF method takes into account measured values of the material properties (i.e. Young's modulus of elasticity and Poisson's ratio), the structural damping factor, and the geometry of the plate directly. These factors are inherently measured in Methods 2 and 3. Errors in these values can significantly effect the results. For example, a 1.0% error in the thickness of the plate will result in an error of approximately 3.0% in the power. The relationship between Young's modulus of elasticity and the power is such that a 1.0% error in Young's modulus would cause a 1.0% error in power. In the two shaker test setup used in this dissertation, the structural damping factor will have very little effect on the results, and even a significant error in the structural damping factor estimate will cause little error in the power computation. This is because a significant amount of energy is being transmitted between the two shakers and the amount of power lost due to structural damping is small compared to the total power being transmitted. Even though these factors can cause significant error, great care was exercised in obtaining the values to minimize the effects. With the understanding that slight differences will

occur due to these factors the power results computed by these three methods can be compared and used to validate or invalidate each other.

5.4 Experimental Results

The three power computation methods described in Section 5.3 were applied to the simply supported plate described in Section 5.2. The power results, as well as the fundamental results which lead to the power results, will be presented and discussed in this section. Four frequencies of interest will be investigated. These are 79.0 Hz, 311.0 Hz, 909.0 Hz, and 1110.0 Hz.

5.4.1 79.0 Hz Case

In the 79.0 Hz case the two shakers were phased such that shaker 2, as indicated in Fig. 5.4, lagged shaker 1 by 174.6 degrees and had a voltage magnitude of 89% of shaker 1. These values were determined by plotting the magnitude and phase of the frequency response of the two input signals (output voltages leaving the signal generator into the power amplifier). The input signals were tuned such that the shakers had a relative phase slightly off of 180 degrees to ensure that a significant amount of active power in the plate would exist [31].

The plate was scanned from five different laser positions. In structure-to-laser coordinates the x, y, and z positions of the laser for the five scans are shown in Table 5.1 in units of meters. It was previously determined that to more accurately extract the in-plane velocity measurement, which also leads to a more accurate representation of the total velocity field solution, the structure should be scanned at high angles of incidence. Scans 4 and 5 represent the same laser position but different scan areas. These two scans were taken at a relatively high angle of incidence as indicated by the coordinates. Table 5.1 also indicates the scan den-

sity which represents the number of data points acquired by the SLDV during the indicated scan.

Table 5.1. Laser positions and scan densities for the five scans at 79.0 Hz

	x coord. (m)	*y* coord. (m)	*z* coord. (m)	Scan Density
Scan 1	-1.298	0.859	2.533	100 x 120
Scan 2	0.225	1.185	1.903	100 x 120
Scan 3	1.555	0.081	2.158	100 x 120
Scan 4	1.844	0.088	0.974	60 x 120
Scan 5	1.844	0.088	0.974	60 x 120

The 79.0 Hz frequency corresponds closely to the first resonance frequency of the plate. The real and imaginary velocity components in m/s at this frequency using an 8x8 quintic B-spline mesh are shown in Fig. 5.5. The relative magnitudes of these plots indicate that 79.0 Hz is close to the first resonance frequency of the plate because the response is mostly due to the real component. Although difficult to detect, the slight variation from the simply supported boundary condition should be noted at the corners of the plate. The magnitude of the velocity field is shown in Fig. 5.6, and again the slight deviations from a truly simply supported plate can be detected.

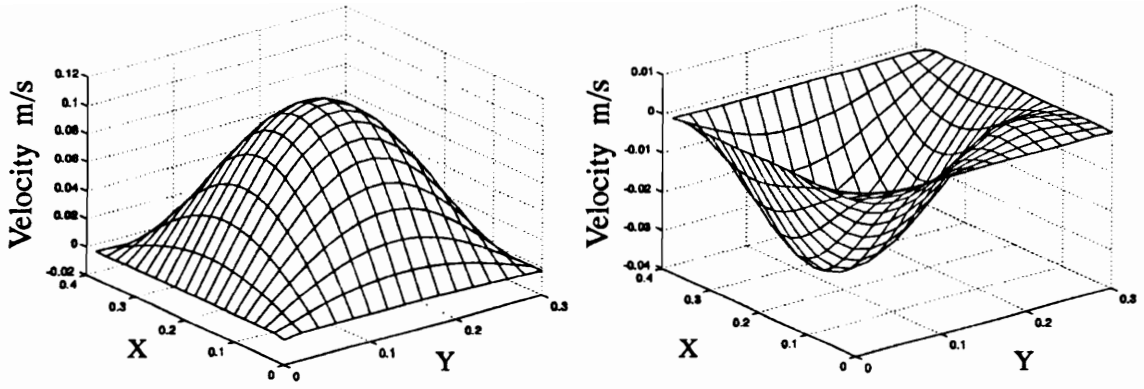

Real Velocity Component Imaginary Velocity Component

Figure 5.5. Real and imaginary velocity components at 79.0 Hz

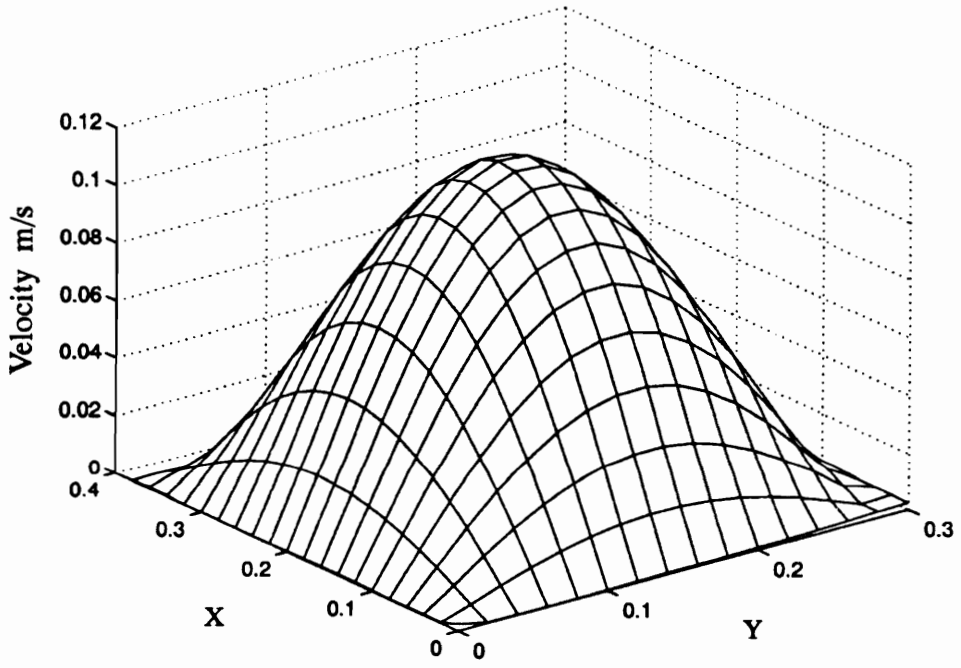

Figure 5.6. Velocity magnitude at 79.0 Hz

As discussed in Chapter 3, the velocity model from which the power is computed is based on a finite element approach. The "best" models of the velocity field and the power field can be obtained through mesh convergence. Convergence of the velocity-field model is determined by comparing the residuals between the laser data and the ESDM model. The

best converged model is the model in which the residuals are minimized. In the 79.0 Hz case several mesh densities were investigated. The mesh densities compared in this section consist of a 4x4, 5x5, 6x6, 8x8, 10x10, and a 12x12 quintic B-spline element model.

The residual plots of the real velocity component for all 6 mesh configurations are shown in Fig. 5.7. Again, this residual is computed by taking the difference between the actual laser data scan points and the ESDM velocity solution. The horizontal axis in these figures is shown in units of 10,000 samples as indicated and the vertical axis is in units of m/s.

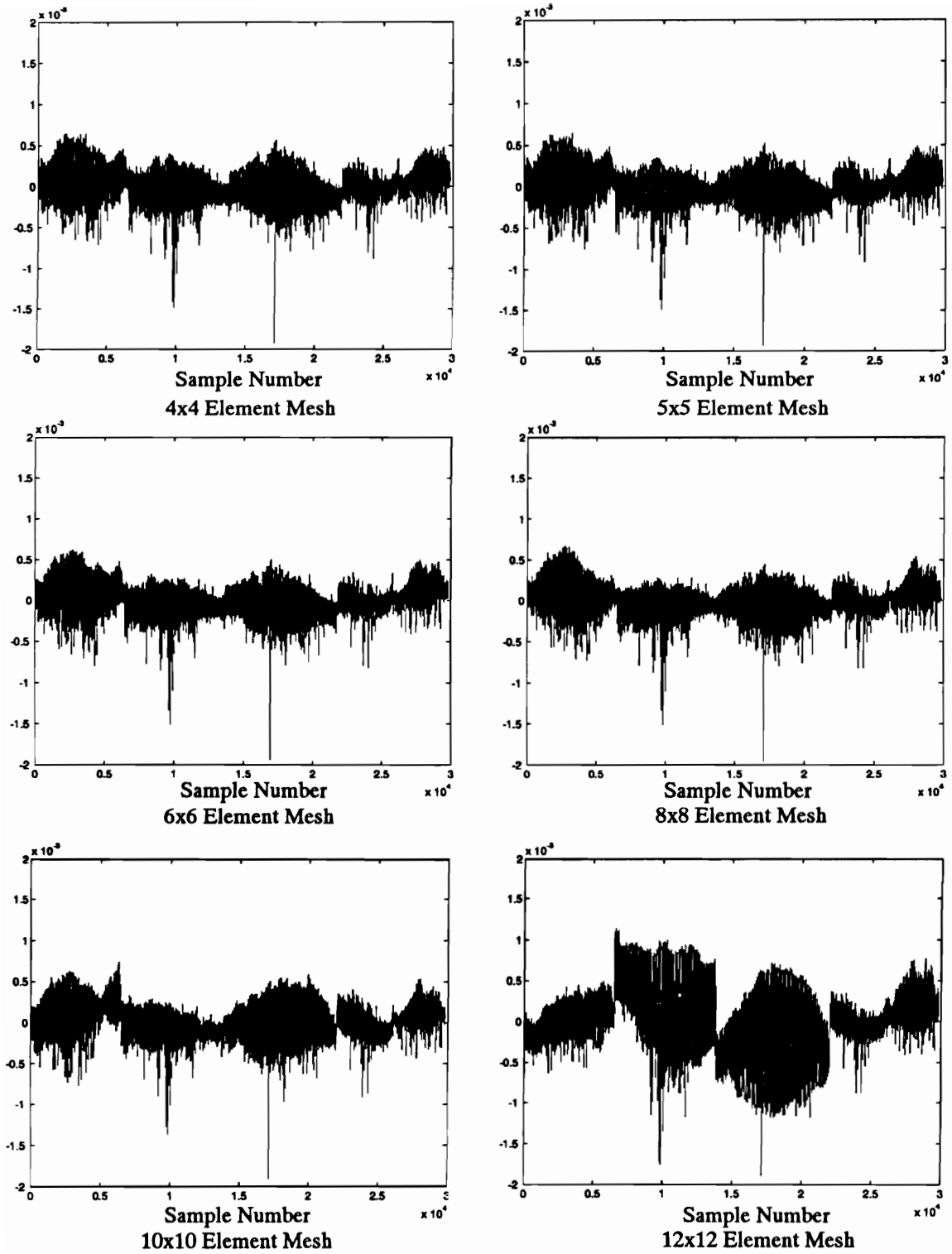

Figure 5.7. Residuals of the real velocity (m/s) component at 79.0 Hz for mesh configurations of 4x4, 5x5, 6x6, 8x8, 10x10, and 12x12

The number of samples along the horizontal axis does not directly correspond to the number of samples indicated by the scan density in Table 5.1. This is because several of the samples represent data which were taken off the structure to ensure complete coverage of the plate. Also, several points were omitted from the solution due to a statistical cut off which was placed on the data. This cut off required a 95% correlation between the time-series model and the actual laser data.

As shown by Fig. 5.7 only slight differences exist between the 4x4, 5x5, 6x6, and 8x8 element models. This implies that a 4x4 mesh and possibly even a lower number of elements is sufficient to represent the velocity field. The maximum residuals between the actual laser data and the ESDM velocity solution in these four models represent approximately 0.5% of the real velocity component. In the 10x10 and the 12x12 element models the residuals begin to increase. This is partly due to resolving power of the quintic B-spline elements. In these models, where the number of elements is higher, the quintic B-spline elements begin to fit any noise on the signal from the laser. This results in a less accurate representation of the true velocity field.

Complete randomness in the residuals does not exist in the velocity models as the data from each scan can be visually separated by the increase and the decrease in the residuals. This is most prevalent in the 12x12 mesh. These somewhat nonrandom results are most likely due to a poor laser registration.

The residuals appear to be somewhat proportional to the velocity field in that the largest residuals occur at the peak velocities. It is possible that this occurs due to the large movement of the speckle on the photo-diode as the signal is being detected [1].

Figure 5.8 illustrates the residuals for the imaginary velocity component. The maximum residuals indicate a difference of approximately 2.5% between the data and the ESDM velocity solution. Again, the first four models are shown to provide the most accurate results, while the last two models begin to provide too much resolving power.

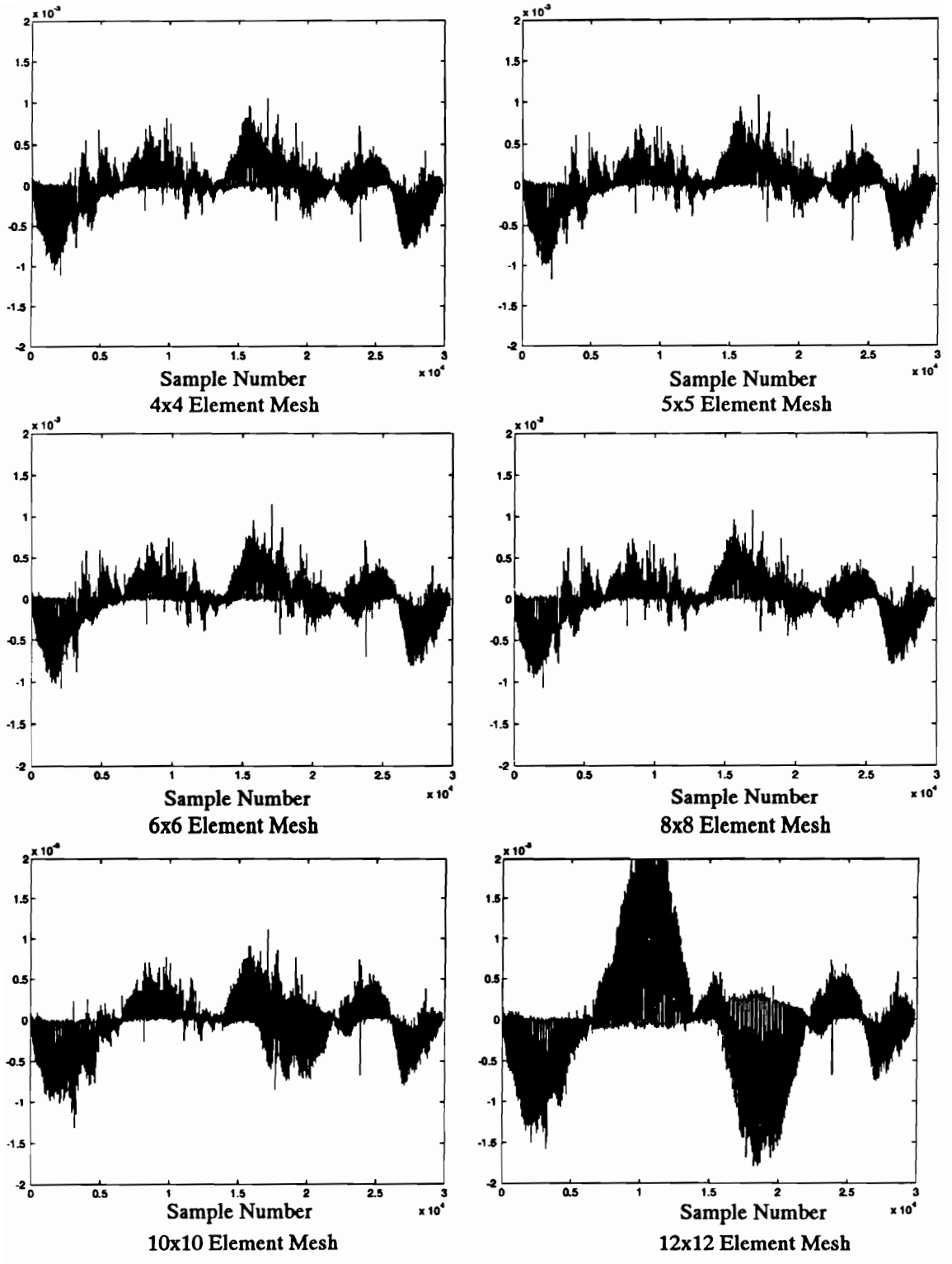

Figure 5.8. Residuals of the imaginary velocity (m/s) component at 79.0 Hz for mesh configurations of 4x4, 5x5, 6x6, 8x8, 10x10, and 12x12

Table 5.2 summarizes the mean and standard deviation for each residual plot as well as the residuals of the velocity magnitude. These results indicate that the 6x6 element mesh provides the "best" representation of the velocity field in that the mean and standard deviation of the residuals of the velocity magnitude are minimized for this mesh. Even though the residuals did not appear to be completely random, due to the relatively small magnitudes of these residuals it was determined that a very good model of the velocity field was obtained. The "best" mesh representation for the velocity field will not necessarily be the "best" mesh for the power. This is because the power is based on derivatives of the velocity field and hence should converge at a slower rate.

Table 5.2. Summary of the velocity residual statistics for the 79.0 Hz case

Mesh	Real Velocity Component		Imaginary Velocity Component		Velocity Magnitude	
	Mean	Std.	Mean	Std.	Mean	Std.
4x4	-8.015e-6	1.658e-4	9.422e-6	2.341e-4	2.307e-4	1.710e-4
5x5	-8.085e-6	1.644e-4	9.208e-6	2.307e-4	2.279e-4	1.687e-4
6x6	-7.522e-6	1.622e-4	9.146e-6	2.305e-4	2.266e-4	1.680e-4
8x8	-8.262e-6	1.619e-4	9.003e-6	2.326e-4	2.232e-4	1.751e-4
10x10	3.817e-6	1.864e-4	-2.527e-5	2.767e-4	2.724e-04	1.944e-4
12x12	4.339e-7	3.262e-4	-3.730e-6	6.877e-4	5.823e-4	4.902e-4

After the velocity field has been represented, the angular velocities, bending moments, twisting moments, and shear forces are computed by taking spatial derivatives of the velocity and displacement fields as discussed in Chapter 3. This section continues by investigating the generalized force and velocity representations as well as the contribution to the total power for each of these components. Only the results for the 8x8 quintic B-spline mesh will be presented with the understanding that the 4x4, 5x5, and 6x6 element models provide very similar results.

The first power components to be investigated are due to the bending moments and the associated angular velocities. The power due to this component is computed as shown by Eqs. (5.3) and (5.4) where $q_{x\,bend}$ represents the power due to bending in the x direction and $q_{y\,bend}$ represents the power due to bending in the y direction. The angular velocities and the bending moments about the x and y axes are given by $\dot{\theta}_x$, $\dot{\theta}_y$ and M_y, M_x respectively. The structural damping factor is represented by η.

$$q_{x\,bend} = 0.5\left[\mathrm{Re}[M_x]\,\mathrm{Re}\left[\dot{\theta}_y\right] + \mathrm{Im}[M_x]\,\mathrm{Im}\left[\dot{\theta}_y\right]\right] + 0.5\,\eta\left[\mathrm{Re}[M_x]\,\mathrm{Im}\left[\dot{\theta}_y\right] - \mathrm{Im}[M_x]\,\mathrm{Re}\left[\dot{\theta}_y\right]\right] \tag{5.3}$$

$$q_{y\,bend} = 0.5\left[\mathrm{Re}[M_y]\,\mathrm{Re}\left[\dot{\theta}_x\right] + \mathrm{Im}[M_y]\,\mathrm{Im}\left[\dot{\theta}_x\right]\right] + 0.5\,\eta\left[\mathrm{Re}[M_y]\,\mathrm{Im}\left[\dot{\theta}_x\right] - \mathrm{Im}[M_y]\,\mathrm{Re}\left[\dot{\theta}_x\right]\right] \tag{5.4}$$

Figure 5.9 illustrates the real and imaginary bending moment representations about both the x and y axes. These components have been computed by taking two spatial derivatives of the displacement field as shown by Eqs. (3.74). The moments are computed in terms of moment per element width and, hence, have units of newtons. Figure 5.9 indicates that the real bending moments about the x and y axes are close to the same magnitude. It is further shown that the imaginary component has a larger magnitude than the real component. The largest bending moments are shown to occur in the center of the plate as expected. Theory predicts that for a simply supported plate the bending moments at the boundary are zero. Figure 5.9 illustrates that the bending moments are the smallest at the boundary but that they are not zero. This is primarily due to two reasons. The first is that the simply supported plate conditions are not perfect in this experimental case and that indeed the bending moments are not exactly zero. The second reason is due to the effects of taking derivatives of experimental data. Taking derivatives magnifies any errors or differences while integration is a smoothing

process. It is therefore, expected that the generalized force models will not be as smooth and exact as the velocity model. One drawback of this representation as well as any other experimental model is that it is impossible to determine if the error is in the modeling or if these moments actually exist.

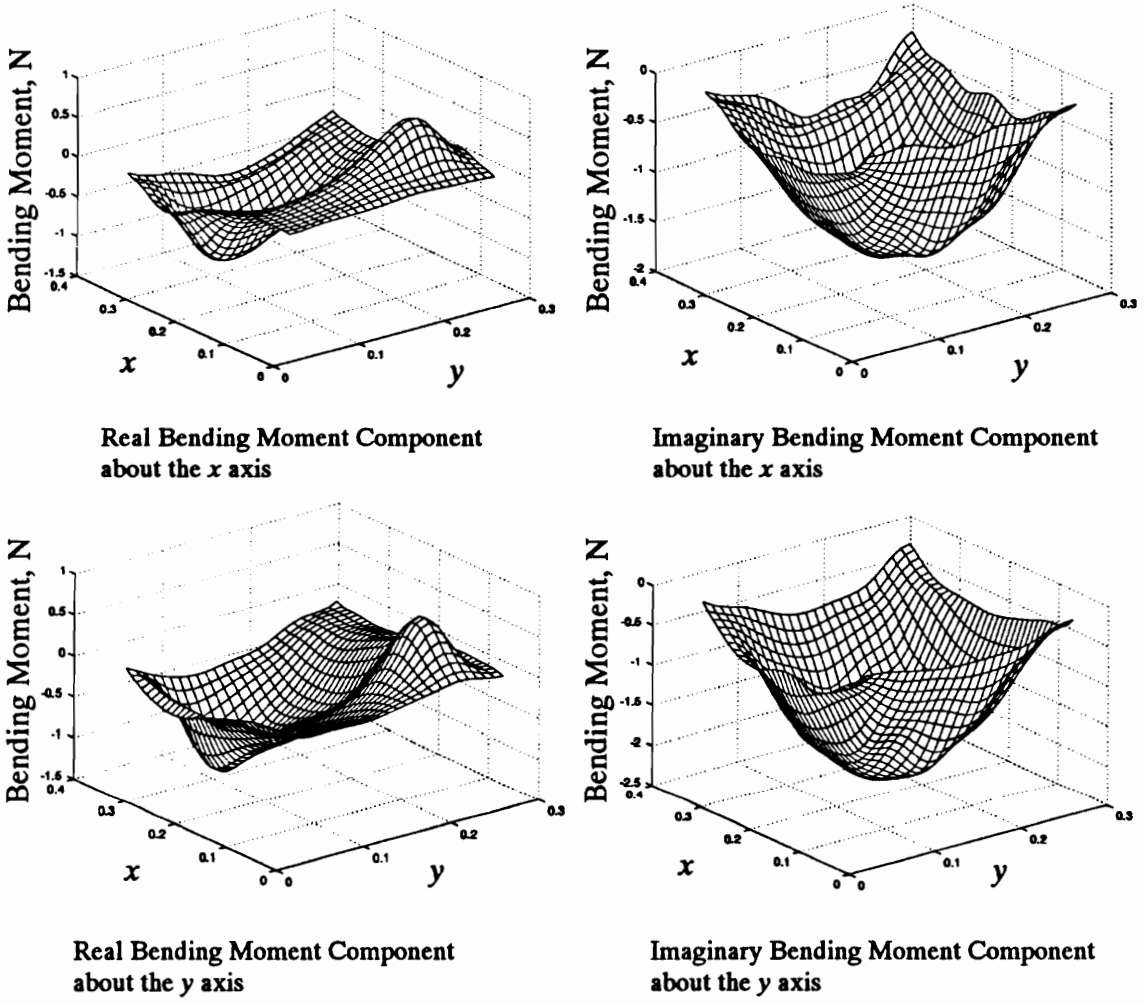

Real Bending Moment Component about the x axis

Imaginary Bending Moment Component about the x axis

Real Bending Moment Component about the y axis

Imaginary Bending Moment Component about the y axis

Figure 5.9. Real and imaginary bending moment in the x and y directions

The angular velocities associated with these bending moments are computed by taking the first spatial derivative of the velocity field. Figure 5.10 shows plots of the angular velocity fields. Except in the corners of the plate, where significant distortion is already beginning to develop after the first derivative, these plots appear to closely follow the

expected theory. It should be noted that the boundary element in each figure is shown to drastically change slope. Taking subsequent spatial derivatives of this representation will propagate this error even further into the plate.

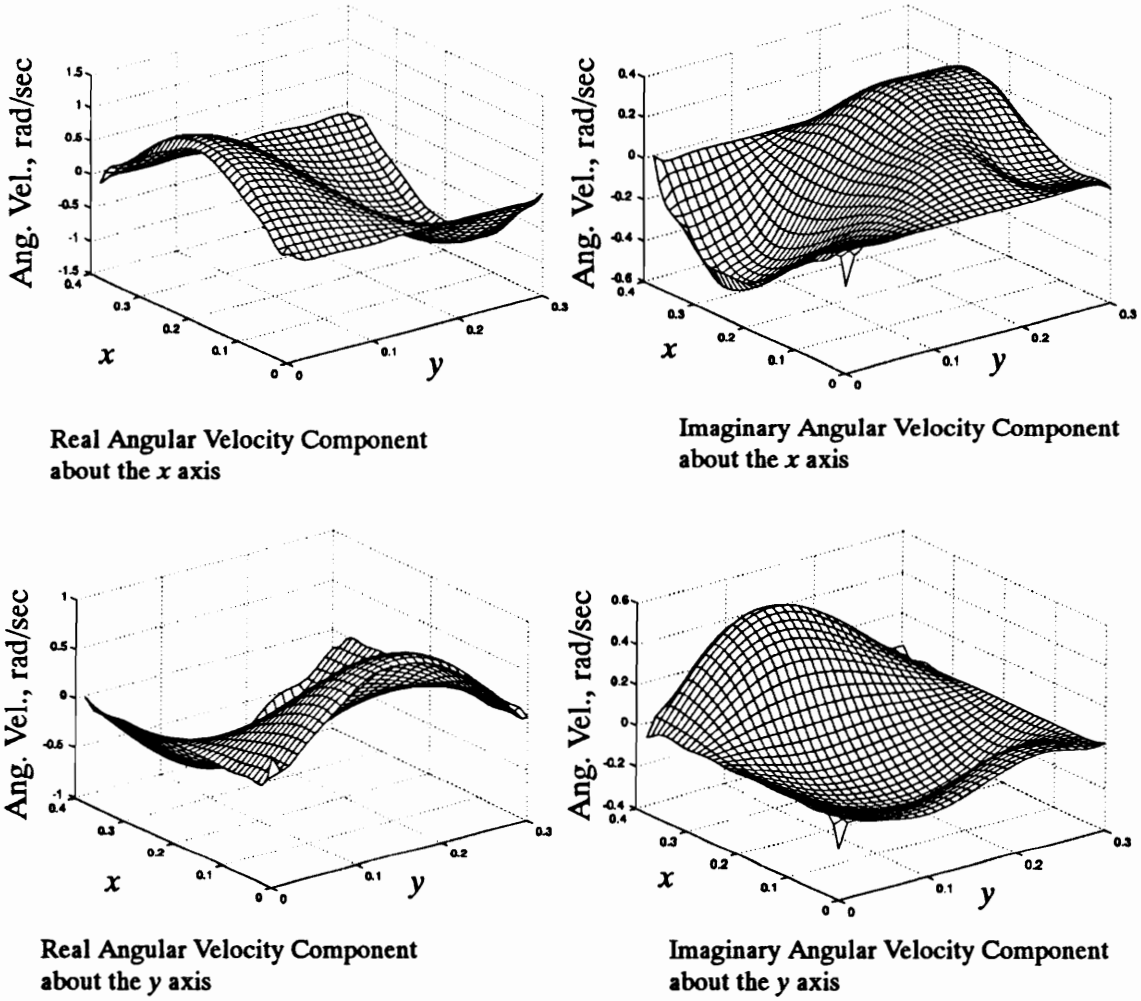

Figure 5.10. Real and imaginary angular velocities about the *x* and *y* axes

The power due to the bending moments, as defined by Eqs. (5.3) and (5.4) is shown in Fig. 5.11. The large power vectors on the top and bottom horizontal boundaries are due to the propagation of error in the derivative computation process of the bending moments. The large power vectors shown to occur in the *y* direction are due to the $q_{y\,bend}$ component

and more specifically the non-zero bending moment about the y axis (M_x) along the x axis boundary. The error that develops in the ESPF method is mainly contained on the boundaries of the structure. This is due to the discontinuities that occur in the B-spline mesh and the fact that less data is used to solve for the governing control points on the plate boundaries. It is, therefore, strongly suggested that when taking data, a larger area than the exact area of interest should be scanned with the laser. It is not suggested that these are the correct values or representation of the bending moments at the boundaries. However, the power vectors inside the boundaries of the plate do appear to follow the theory and accurately represent the power. The largest power vector excluding the power vectors on the boundary of the plate represents a magnitude of 0.7102 W/m. It will be shown that this is approximately 23% of the total power in the structure.

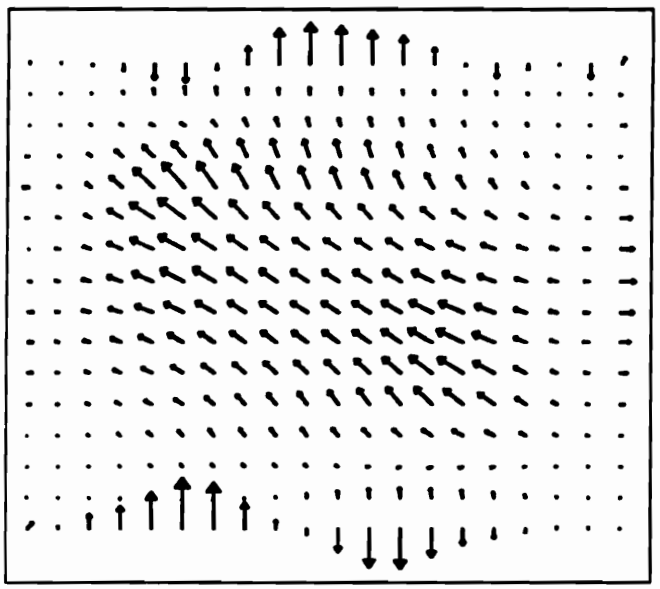

Figure 5.11. Power component due to bending moments only

The next power component of interest is due to the twisting moments and can be expressed as shown by Eqs. (5.5) and (5.6).

$$q_{x\,twist} = 0.5\Big[\mathrm{Re}\big[M_{xy}\big]\mathrm{Re}\big[\dot{\theta}_x\big] + \mathrm{Im}\big[M_{xy}\big]\mathrm{Im}\big[\dot{\theta}_x\big]\Big] + 0.5\,\eta\,\Big[\mathrm{Re}\big[M_{xy}\big]\mathrm{Im}\big[\dot{\theta}_x\big] - \mathrm{Im}\big[M_{xy}\big]\mathrm{Re}\big[\dot{\theta}_x\big]\Big] \tag{5.5}$$

$$q_{y\,twist} = 0.5\Big[\mathrm{Re}\big[M_{yx}\big]\mathrm{Re}\big[\dot{\theta}_y\big] + \mathrm{Im}\big[M_{yx}\big]\mathrm{Im}\big[\dot{\theta}_y\big]\Big] + 0.5\,\eta\,\Big[\mathrm{Re}\big[M_{yx}\big]\mathrm{Im}\big[\dot{\theta}_y\big] - \mathrm{Im}\big[M_{yx}\big]\mathrm{Re}\big[\dot{\theta}_y\big]\Big] \tag{5.6}$$

Plots of the twisting moments are shown in Fig. 5.12. In Chapter 3 it was discussed that the bending moments M_{xy} and M_{yx} are equal and Fig. 5.12 is used to represent them both. The angular velocities associated with these twisting moments were previously illustrated in Fig. 5.10.

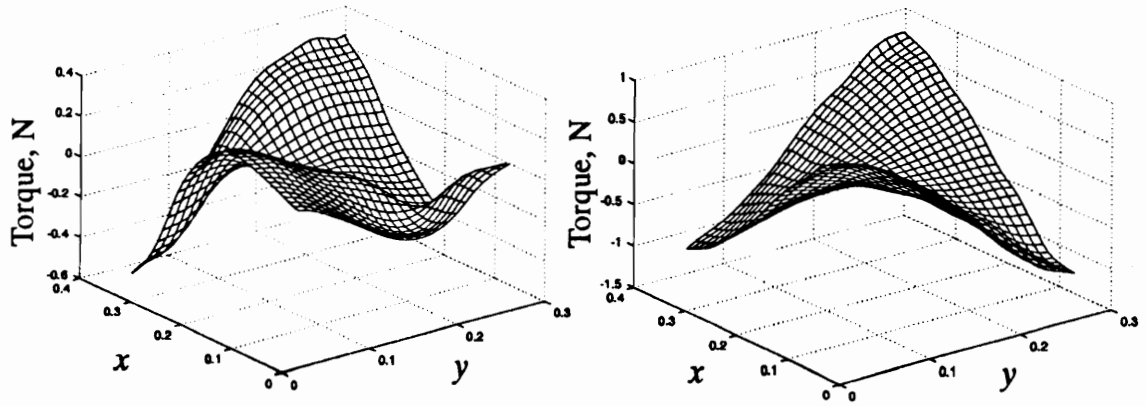

Real Twisting Moment Component

Imaginary Twisting Moment Component

Figure 5.12. Real and imaginary twisting moment

The power due to the twisting moments as computed by Eqs. (5.5) and (5.6) is shown in Fig. 5.13. Excluding the two large vectors in the corners of the plate the largest power vector in Fig. 5.13 has a magnitude of 0.2768 W/m. This is 39% of the power contribution due to the bending moment and 9% of the total power in the structure.

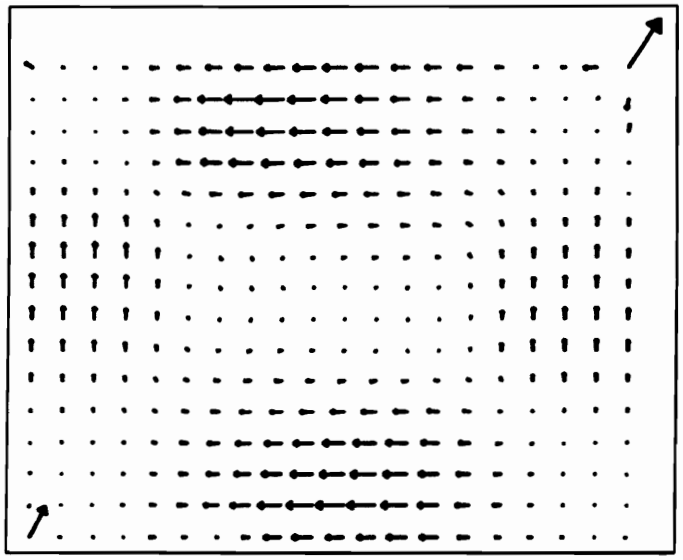

Figure 5.13. Power component due to twisting moments only

The final power component is due to the shear forces and is computed as shown by Eqs. (5.7) and (5.8).

$$q_{x\,shear} = 0.5[\mathrm{Re}[Q_x]\,\mathrm{Re}[\dot{w}] + \mathrm{Im}[Q_x]\,\mathrm{Im}[\dot{w}]] + 0.5\,\eta\,[\mathrm{Re}[Q_x]\,\mathrm{Im}[\dot{w}] - \mathrm{Im}[Q_x]\,\mathrm{Re}[\dot{w}]] \tag{5.7}$$

$$q_{y\,shear} = 0.5\left[\mathrm{Re}\left[Q_y\right]\mathrm{Re}[\dot{w}] + \mathrm{Im}\left[Q_y\right]\mathrm{Im}[\dot{w}]\right] + 0.5\,\eta\left[\mathrm{Re}\left[Q_y\right]\mathrm{Im}[\dot{w}] - \mathrm{Im}\left[Q_y\right]\mathrm{Re}[\dot{w}]\right] \tag{5.8}$$

The shear force computation requires a third spatial derivative computation which will propagate significant error around the boundaries of the plate. Figure 5.14 illustrates the real and imaginary components of the shear forces in the *xz* and *yz* directions. By comparing the magnitudes of these plots to the other generalized forces, it is clearly shown that the shear force is the dominate generalized force in the plate. Although somewhat difficult to see in Fig. 5.14 the large shear forces near the shaker locations can be detected. To better illustrate the forces inside the plate boundary, the boundary values were not plotted.

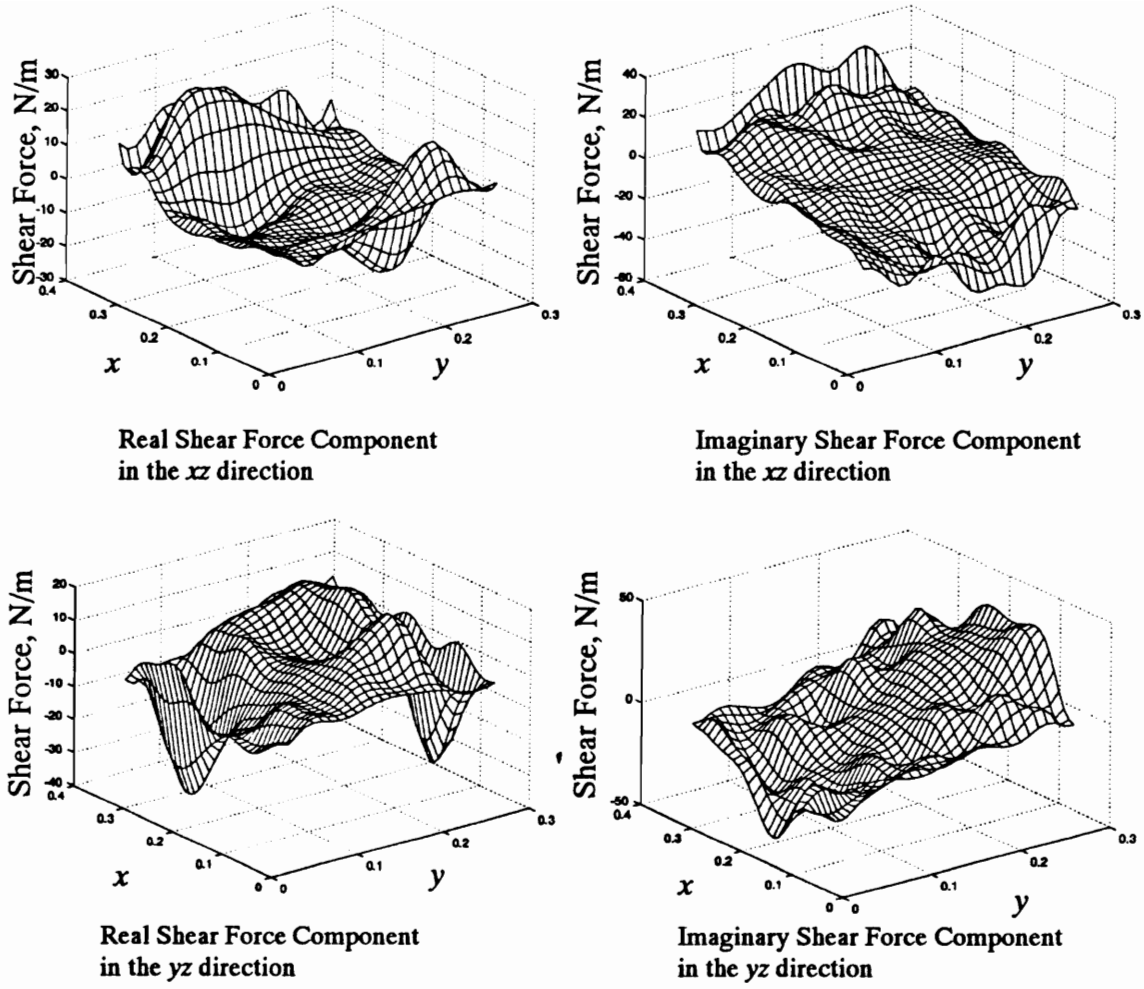

Figure 5.14. Real and imaginary shear force in the *xz* and *yz* directions

A significant result of Fig. 5.14 is that the shear forces are not shown to be perfect representations of small distributed loads. The shear forces are shown to be represented much smoother than actual theory would predict. For example, a point force would appear as a single spike in a perfect representation. However, using the ESDM velocity representation to compute the point-force representation it would appear more like a dome. This phenomena will be further discussed later in this section.

The velocities associated with these shear forces were previously illustrated in Fig. 5.5. The power due to the shear force component is shown in Fig. 5.15. Figure 5.15 clearly

illustrates a flow of power from the source (shaker 1) to the sink (shaker 2). Again, neglecting the large vector in the upper corner of the plate, the largest power vector represents a magnitude of 2.1268 W/m. This represents a value approximately 300% larger than the bending moment component, 770% larger than the twisting moment component, and 68% of the total power in the structure.

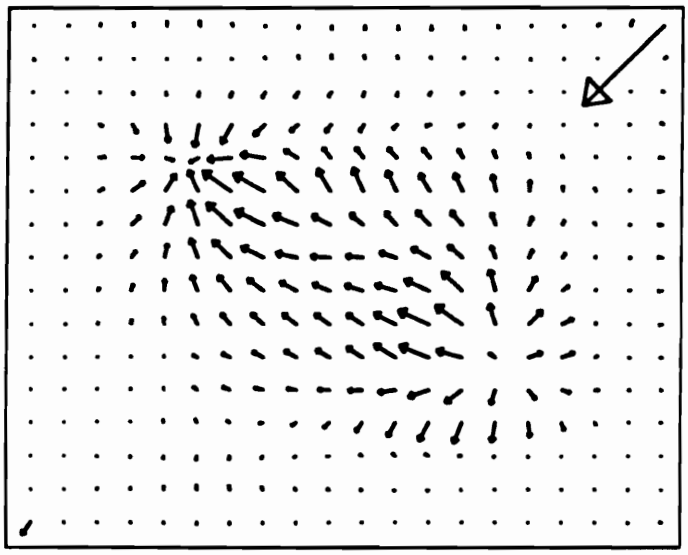

Figure 5.15. Power component due to the shear forces only

It was shown that significant error at the boundaries developed in the shear force representations. However, when multiplying the shear forces by the velocities to obtain the power, the boundary problems disappear due to the small transverse velocities which exist on the simply supported plate boundaries. This is not the case for the power components due to the bending and twisting moments because the angular velocities are actually maximized on the plate boundaries in this case. Hence, most of the error on the boundary in the power model is due to the bending moment component.

By combining the three power components, the total power in the plate can be computed as shown by Fig. 5.16. The magnitude of the velocity field indicating the operating shape of the plate is also superimposed on the power-flow vector plot. The darker areas of

the velocity-field representation indicate areas of high velocity. The 2 large black dots on the plate represent the relative size and location of the shaker and impedance head mount plates while the small black dots on the plate boundaries represent the screw locations as discussed in Section 4.2.

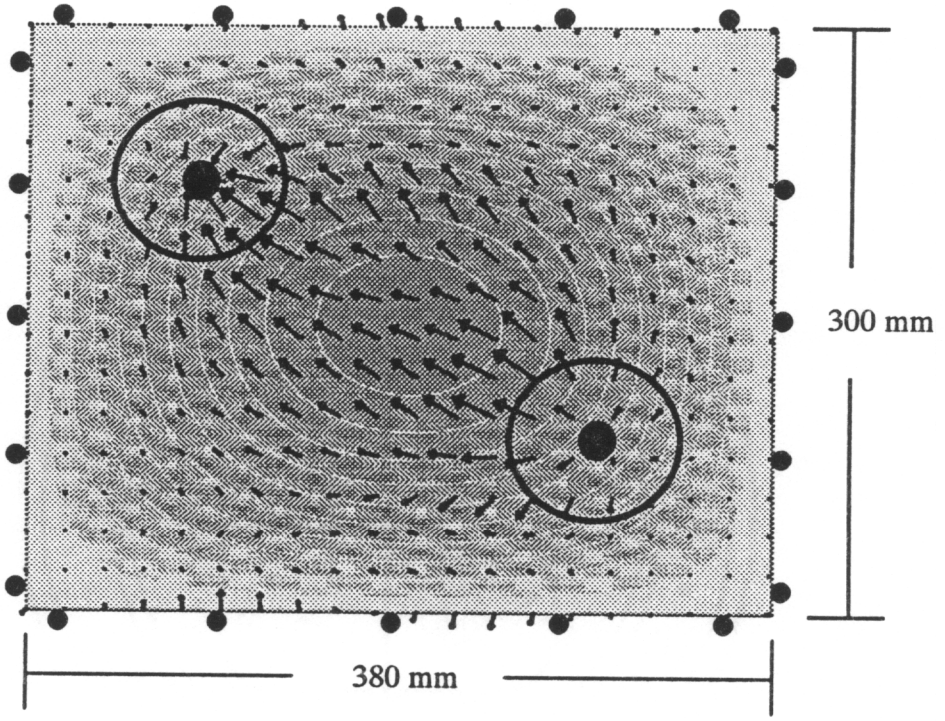

Figure 5.16. Power-flow vector plot and velocity field at 79.0 Hz

Figure 5.16 clearly indicates that under these conditions shaker 1 acts as a power source, shaker 2 acts as a power sink, and the main flow of power is in a direct path from shaker 1 to shaker 2. A significant amount of power is also shown to exist on both the top and bottom horizontal boundaries of the plate, while very little power is detected on the vertical boundaries. This implies, as expected, that the simply supported boundary conditions are not perfect.

This power model is based on approximately 30,000 laser samples. The time requirement to collect this data is approximately 3-4 hours depending on the number of scans. To compute the velocity field based on these 30,000 samples using the ESDM approach requires approximately 45 minutes. To compute the power at 1200 points requires approximately an additional hour. So the entire data processing from the raw laser data to the power model can be performed in approximately 2 hours.

Under ideal point force conditions, the largest power vectors would exist at the point source and then decrease in magnitude due to various loss mechanisms as the distance from the source is increased. In the extreme case of an ideal point force a discontinuity in the shear-force representation occurs. Many power-flow methods which derive the generalized forces from a representation of the velocity or displacement fields do not have the resolving power to accurately model sharp changes or discontinuities in the shear force. As a result, a smoother shear-force representation is obtained. When the power is computed using a smoother shear-force representation, the largest power vectors will not necessarily occur at the source but will appear slightly further away from the exact location of the excitation. The severity of the mis-representation of the power near the source or sink is dependant on the ability of the model to to accurately represent sharp changes or discontinuities in the shear-force representation.

In experimental testing, true point forces can only be approximated. In this case, with the 2.0 cm diameter impedance head mount plates, point force conditions are not assumed or expected. Under ideal conditions with a 2.0 cm diameter mount plate the maximum power should occur at a radius of 1.0 cm from the center of the mount plate. Figure 5.16 indicates that the largest vectors are shown to occur slightly further than 1.0 cm away from the center

of the mount plates. The large black ring surrounding the mount plate in Fig. 5.16 represents the circular control volume where the largest power in the plate is computed.

To further investigate this concern, the net power crossing a circular control volume, centered at the source, was computed. The control volume was then incrementally enlarged in the radial direction and the net power was again computed. The net power normal to each circular control volume was computed at 72 equally spaced points around each control volume. These 72 points were then used to compute the total power normal to the control volume. The total power in 30 control volumes at radial increments of 0.2 cm was computed for a total radial distance of 6.0 cm from the center of the mount plate. This same process was also performed for a set of control volumes centered at the sink. Various mesh densities were also analyzed to verify the convergence of the power field.

Figure 5.17 shows a plot of the net power crossing each circular control volume for the 30 control volumes centered around shaker 1. Five different mesh densities are shown in Fig. 5.17. The best model is determined by the quickest ramp up to the maximum power. As indicated the best model in the 79.0 Hz case was the 8x8 element mesh. Figure 5.17 clearly illustrates typical model convergence results. As the number of elements is increased from a 4x4 to a 6x6 and finally an 8x8 element model, the maximum power is shown to spatially converge closer to the actual source. However, the 10x10 and the 12x12 elements models provide too much resolving power and the models begin to diverge. The ability to converge the power model is one of the unique qualities of the ESPF method. Figure 5.17 illustrates that the 8x8 model had a maximum power of 0.1706 W at a radial distance of 4.4 cm from the center of the source. This is 3.4 cm away from where the maximum power should theoretically occur.

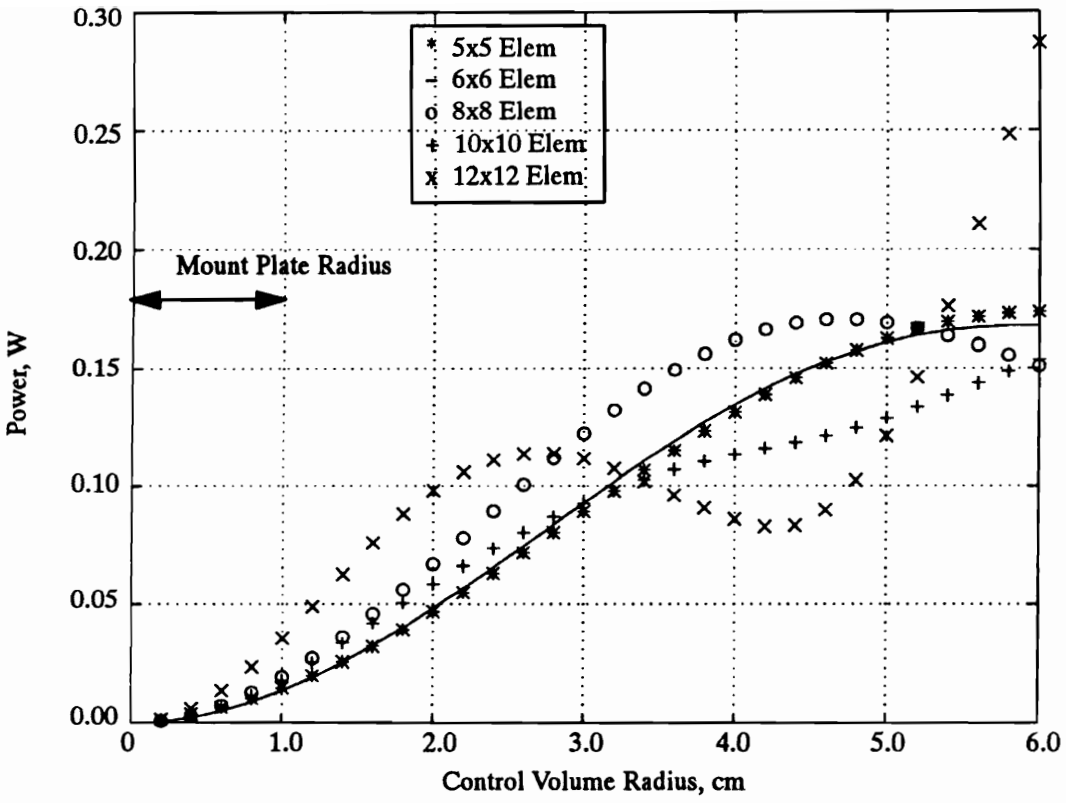

Figure 5.17. Net power in each control volume around shaker 1 at 79.0 Hz

This same type of control volume analysis was performed for shaker 2 at 79.0 Hz. The results are shown in Fig. 5.18. Again, the "best" model is shown to be the 8x8 element mesh. As expected the "best" power model does not correspond to the "best" velocity model and more elements are required to accurately represent the power.

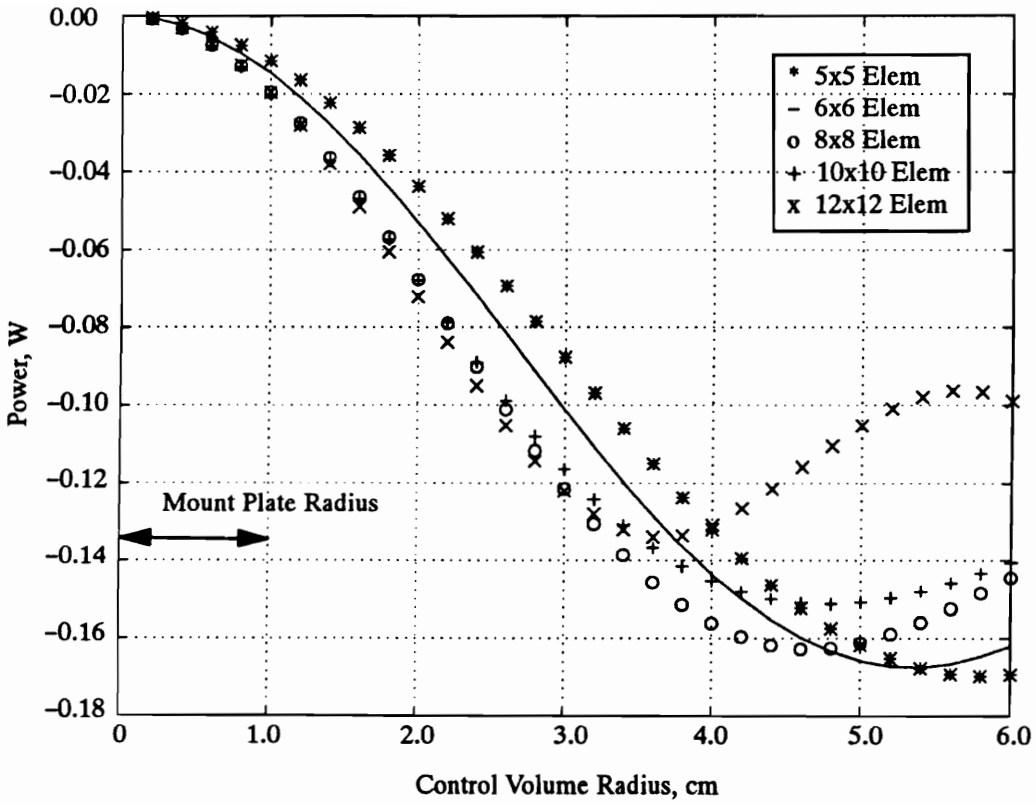

Figure 5.18. Net power in each control volume around shaker 2 at 79.0 Hz

In this power-flow model an 8x8 uniform quintic B-spline mesh was used to represent the velocity field. Using a more "locally" refined mesh around the locations of the source and sink could possibly decrease the radius at which the maximum power was obtained and improve the accuracy of the computed injected power.

To verify the maximum power values computed by the ESPF method, the control volume which contained the maximum power was compared to the injected power computations of Methods 2 and 3. It is expected that since the maximum power computed from the ESPF method does not occur exactly at the source that some difference between the comparison of the ESPF method and the injected power computations of Methods 2 and 3 will exist. It is further expected that the power values computed by the ESPF method will be slightly less

than the power values computed by Methods 2 and 3 due to the losses in power which occur in the plate from the center of the source to the control volume where the ESPF computes the maximum power.

The power injected into the plate by shaker 1 as computed by Method 2 was 0.1908 W with a standard deviation of 0.252 mW. The power absorbed from the plate by shaker 2 as computed by Method 2 was 0.1853 W with a standard deviation of 0.273 mW.

The power injected into the plate by shaker 1 as computed by Method 3 was 0.1845 W with a standard deviation of 0.107 mW. The power absorbed from the plate by shaker 2 as computed by Method 3 was 0.1692 W with a standard deviation of 0.154 mW.

Table 5.3 summarizes these results and lists the percent difference between the three methods. The values in Methods 2 and 3 were computed using the force gage calibration values shown in Table 5.4. The input power results computed from the three methods are as expected. The ESPF method predicts slightly less power than the power computed by Methods 2 and 3. It is also shown that Methods 2 and 3 produce very similar results. In the power out computations, Methods 2 and 3 are not as close as expected. The energy leaving through shaker 2 as computed by Method 2 is slightly higher than expected. This is most likely due to a change in the system which could have occurred between the two data acquisition processes. However, overall the comparisons between the three methods are very good. As discussed in Chapter 3, it was determined that the impedance heads used were torque sensitive and although great care was taken to appropriately calibrate these transducers at the specified torque slight error could have occurred. Slight laser calibration error could also account for some of the differences in the results. Other factors such as uncertainty in the plate dimensions, material properties, and misalignment in the force locations which affect the ESPF

results but do not affect the results from Methods 2 and 3 could also cause the results to be slightly different. Considering these possible experimental errors it was concluded that the percentage differences between the three methods were very good and that the ESPF method was able to conserve energy.

Table 5.3. Comparison of the maximum power computed by the ESPF method and the injected power and absorbed power computed by Methods 2 and 3 at 79.0 Hz

Power Measurement Location and comparison definition	ESPF Method Max. Power in C. V. 8x8 mesh	Method 2 Z-Head using Iotech and SGI system	Method 3 Z-Head HP Analyzer cross spec. technique
Shaker 1 (source) W	+0.1706	+0.1908	+0.1845
Shaker 2 (sink) W	–0.1626	–0.1853	–0.1692
% diff. compared to Method 1 (gage 1, gage 2)	------- -------	+11.84 +3.96	+8.15 +4.06
% diff. compared to Method 2 (gage 1, gage 2)	-10.59 +12.25	------- -------	+3.30 +8.69
% diff. compared to Method 3 (gage 1, gage 2)	-7.53 -3.90	+3.41 -9.51	------- -------

Table 5.4. Force gage calibration constants used to compute the values in Table 5.3

Transducer	Force Cal. Factor	Accel. Cal. Factor
Gage 1	125 mv/lb	102 mv/g
Gage 2	118 mv/lb	101 mv/g

5.4.2 311.0 Hz Case

The next frequency of interest was an off-resonance frequency of 311.0 Hz. The shakers were tuned such that shaker 2 lagged shaker 1 by 174.57 degrees and had a magnitude of 85.2% of shaker 1. The plate was scanned from 5 different positions for a total of 7 scans.

In structure-to-laser coordinates the x, y, and z positions of the laser relative to the plate in meters as well as the number of points acquired in each scan are shown in Table 5.5.

Table 5.5. Laser positions and scan densities for the seven scans at 311.0 Hz

	x coord. (m)	y coord. (m)	z coord. (m)	Scan Density
Scan 1	0.3272	0.1389	3.7511	102 x 125
Scan 2	1.7015	0.0888	1.0325	98 x 75
Scan 3	1.7015	0.0888	1.0325	101 x 72
Scan 4	-1.3131	1.0915	1.3301	91 x 63
Scan 5	-1.3131	1.0915	1.3301	92 x 61
Scan 6	1.4181	1.0016	3.0366	93 x 112
Scan 7	0.6148	1.1153	1.3994	86 x 101

The real and imaginary velocity components using a 15x15 element mesh are shown in Fig. 5.19. This figure verifies that 311.0 Hz is an off-resonance frequency. The magnitude of the velocity field is shown in Fig. 5.20.

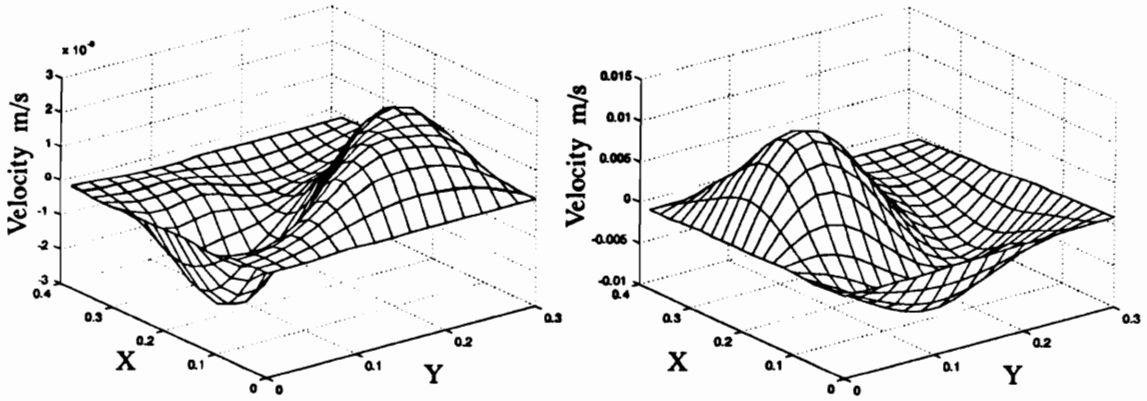

Real Velocity Component

Imaginary Velocity Component

Figure 5.19. Real and imaginary velocity components at 311.0 Hz

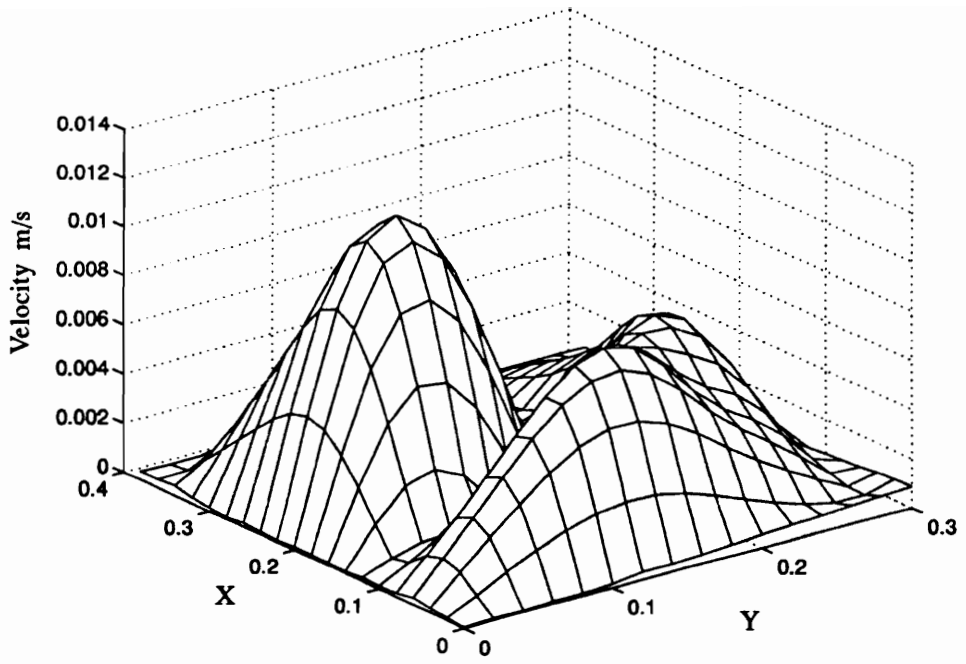

Figure 5.20. Velocity magnitude at 311.0 Hz

As in the 79.0 Hz case it is necessary to perform a velocity convergence process. For this slightly higher frequency it was assumed that more elements would be required to converge the model and accurately represent the velocity field. The residuals between the laser data and the ESDM solution of the velocity field for six different mesh configurations with units of m/s are shown in Figs. 5.21 and 5.22.

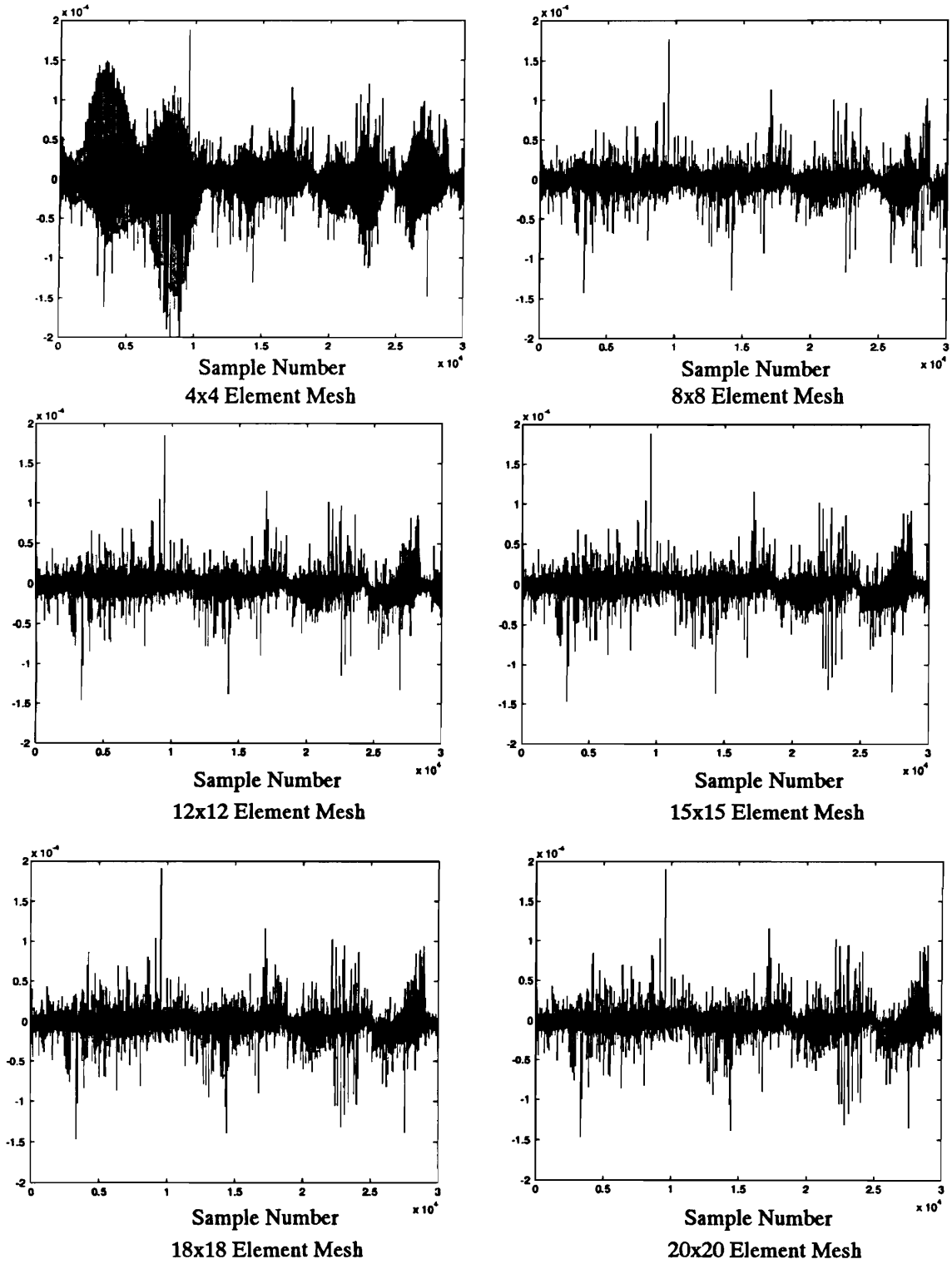

Figure 5.21. Residuals for the real velocity (m/s) component at 311.0 Hz and mesh configurations of 4x4, 8x8, 12x12, 15x15, 18x18, and 20x20

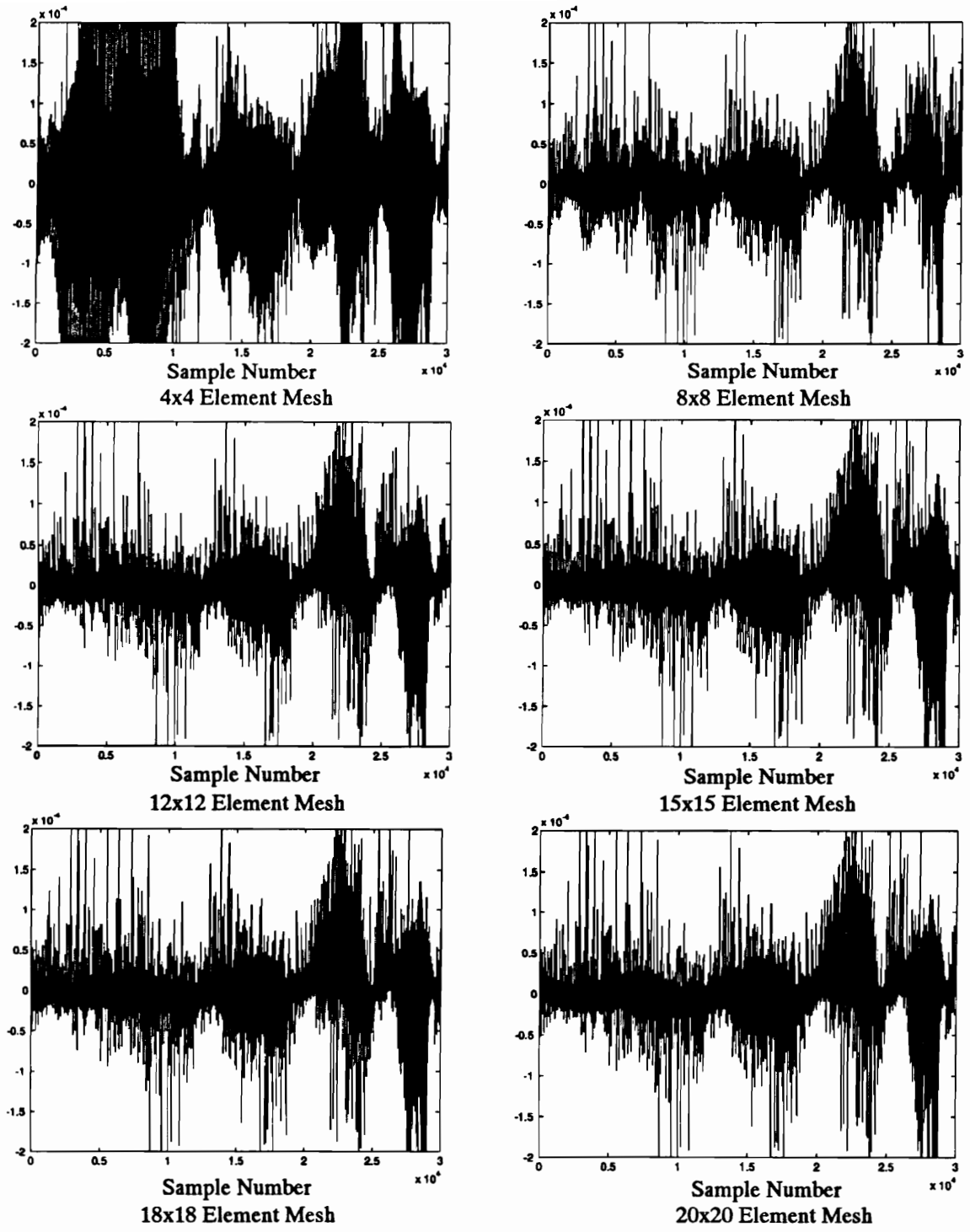

Figure 5.22. Residuals for the imaginary velocity (m/s) component at 311.0 Hz and mesh configurations of 4x4, 8x8, 12x12, 15x15, 18x18, and 20x20

By comparing these residuals it is obvious that the 4x4 element mesh is not dense enough to accurately represent the field. However, the remaining five mesh densities appear to compare very closely in both the real and imaginary velocity components. It should be further noted that even in the 20x20 element mesh the velocity field still appears to be represented quite accurately. This implies that very high quality experimental data was obtained. The residuals in the 311.0 Hz case also appear to be much more random in nature than in the 79.0 Hz case and it is more difficult to distinguish the individual scans.

The statistics for these residual plots are summarized in units of m/s in Table 5.6. This table indicates that although the last five models compare very closely the best model for the velocity-field representation is the 12x12 element mesh.

Table 5.6. Summary of the velocity residual statistics for the 311.0 Hz case

Mesh	Real Velocity Component		Imaginary Velocity Component		Velocity Magnitude	
	Mean	Std.	Mean	Std.	Mean	Std.
4x4	1.069e-6	2.950e-5	-4.121e-6	9.607e-5	7.284e-5	6.938e-5
8x8	6.674e-7	1.697e-5	-2.753e-6	4.720e-5	3.367e-5	3.729e-5
12x12	6.589e-7	1.671e-5	-2.771e-6	4.636e-5	3.179e-5	3.776e-5
15x15	6.717e-7	1.671e-5	-2.826e-6	4.697e-5	3.193e-5	3.853e-5
18x18	6.800e-7	1.718e-5	-2.853e-6	4.733e-5	3.202e-5	3.897e-5
20x20	6.777e-7	1.721e-5	-2.883e-6	4.751e-5	3.204e-5	3.919e-5

The total power in this case computed for a 15x15 element mesh is shown in Fig. 5.23. Figure 5.23 illustrates that the power flow for this case is not a direct flow from shaker 1 to shaker 2. The main power-flow path is shown to be in an "L" shaped pattern starting at shaker 1, flowing in the negative x direction and then in the positive y direction. A relatively weaker power-flow path is also shown to exist which first leaves shaker 1 flowing in a positive y direction and then in a negative x direction. Very little power flow through the center of the

plate is detected. This is because the energy will flow through the higher potential to the lower potential. In this representation, the velocity is the potential and hence the power will flow through the areas of high velocity. Again, as in the 79.0 Hz case, the top and bottom horizontal boundaries show significant power magnitudes compared to the vertical boundaries which is expected to be mainly caused by the bending moment power component.

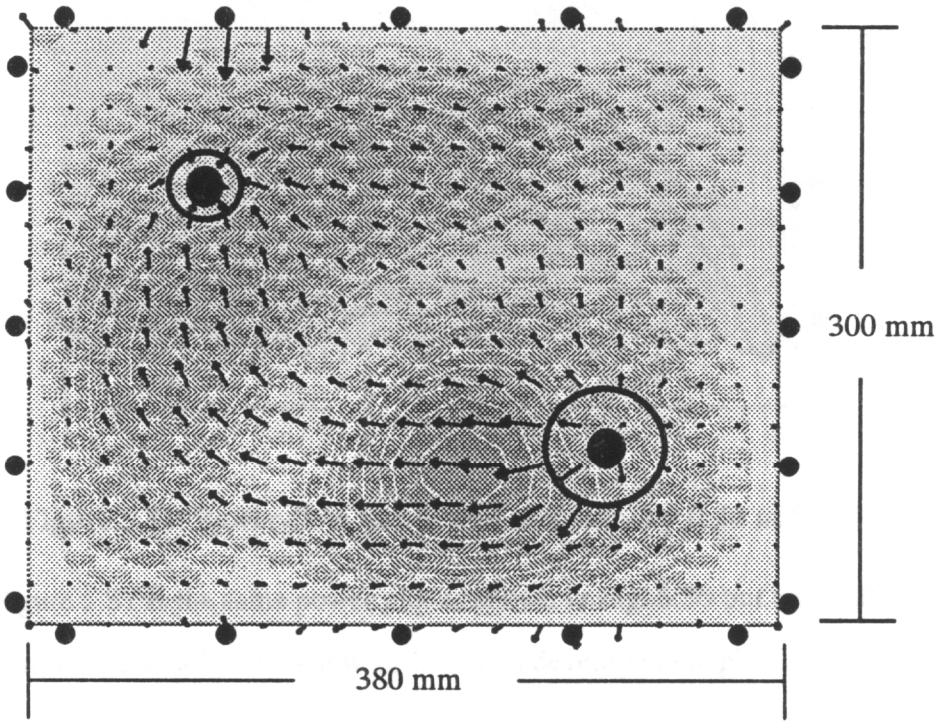

Figure 5.23. Power-flow vector plot and velocity field at 311.0 Hz

The same type of control volume study was performed for this case as was performed for the 79.0 Hz case. Figures 5.24 and 5.25 illustrate that the "best" power model under these conditions is given by the 15x15 element mesh. The power solutions are shown to continually converge up through the 15x15 element mesh and then they begin to diverge. The maximum power input is shown to be 0.7466 mW at a radial distance of 3.4 cm from the center of the source. Given the 2 cm diameter of the mount plates, this maximum power value has

a radial spatial error of 2.4 cm. The power model for this case appears to be much better than the 79.0 Hz case. This is due partly to several factors. The main factor is believed to be the improvement in the laser registration results. More scans were taken with the laser in this case which allows a higher statistical cut off to be applied to the points which were used to solve for the velocity field. In this particular case a 98% correlation between the laser data and the signal processing time-series model was used. It is also possible that the calibration of the electronics as discussed in Chapter 3 was more accurately performed for this case. The near resonance effects in the 79.0 Hz case could also cause more variability in the results due to the large displacements which can cause drop outs due to speckle shift in the velocity signal.

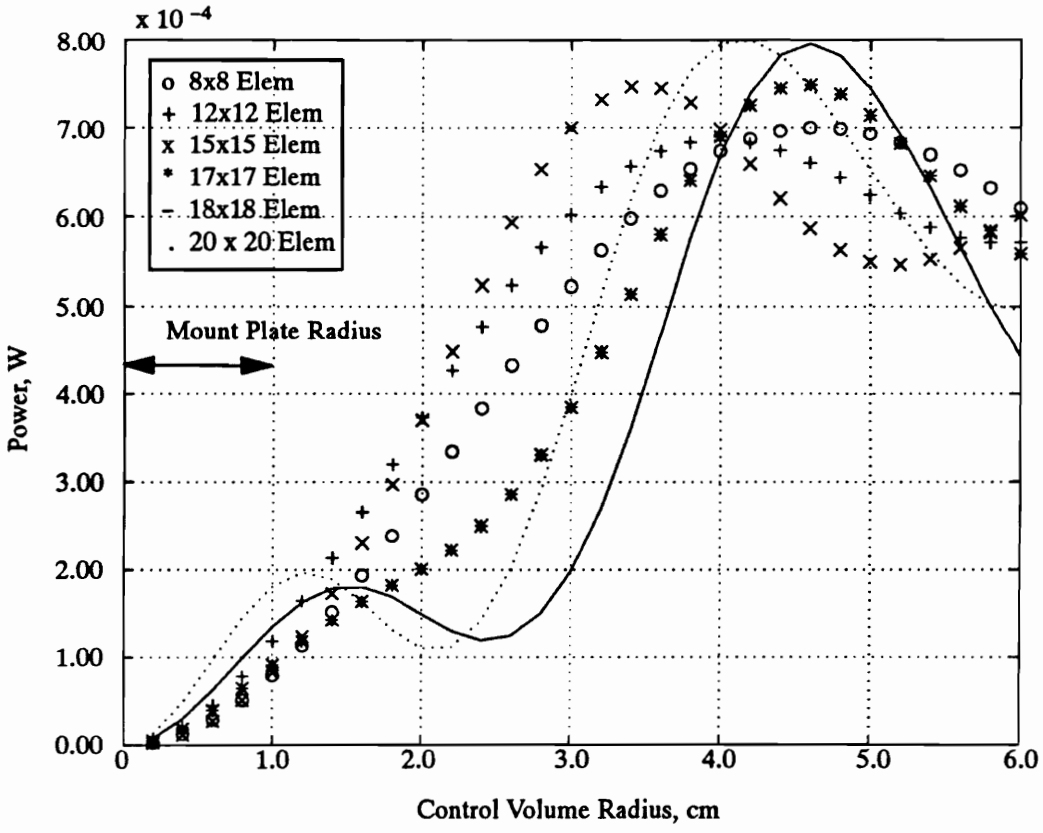

Figure 5.24. Power in each control volume around shaker 1 at 311.0 Hz

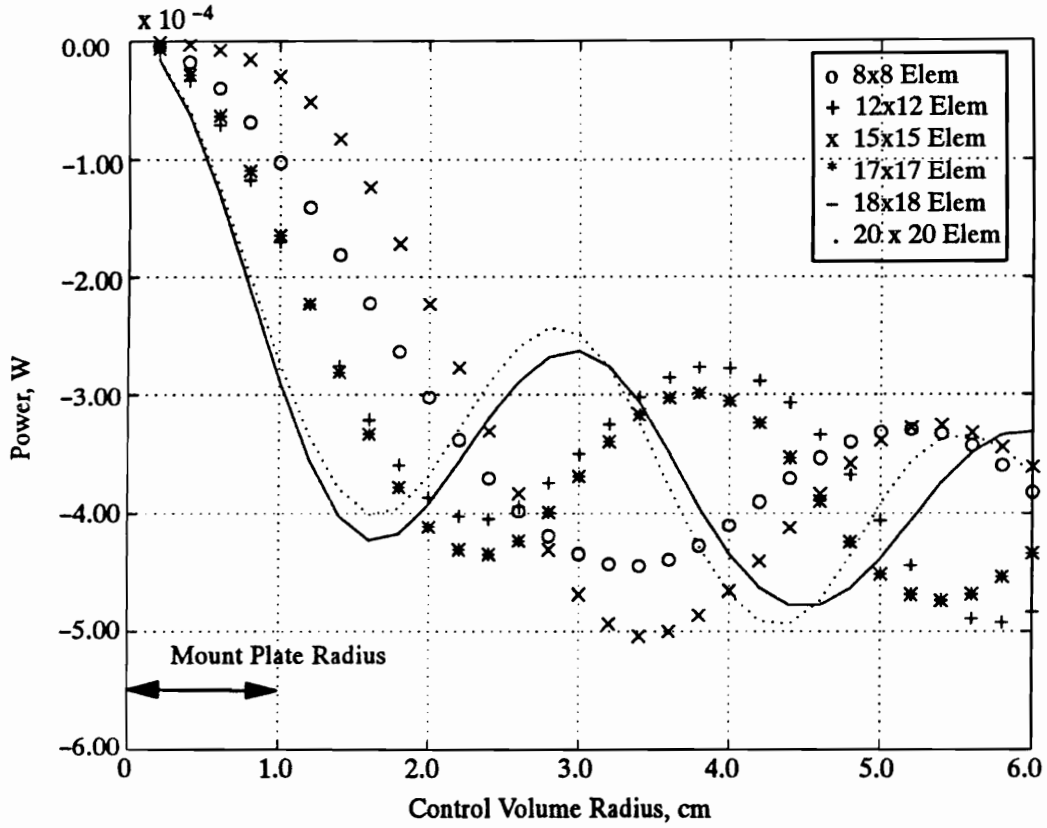

Figure 5.25. Power in each control volume around shaker 2 at 311.0 Hz

The same three methods used to compute the power in the 79.0 Hz case were again used to compute the injected power into the plate. The maximum magnitude computed by the ESPF method was 0.7466 mW. The power injected into the plate by shaker 1 as computed by Method 2 was 0.8102 mW with a standard deviation of 0.0056 mW. The power absorbed from the plate by shaker 2 as computed by Method 2 was 0.5159 mW with a standard deviation of 0.0055 mW.

The power injected into the plate by shaker 1 as computed by Method 3 was 0.7866 mW with a standard deviation of 0.0049 mW. The power absorbed from the plate by shaker 2 as computed by Method 3 was 0.4464 mW with a standard deviation of 0.0048 mW.

Table 5.7 summarizes these results and lists the percent difference between the three methods. These overall results compare closely to the results obtained for the 79.0Hz case. The only significant change is the large difference that occurs in the power absorbed by shaker 2 as computed by Method 3. This difference is most likely due to possible changes that occurred in the system between the scanning procedure and the time the data for Method 3 was acquired.

Table 5.7. Comparison of the maximum power computed by the ESPF method and the injected power and absorbed power computed by Methods 2 and 3 at 311.0 Hz

Power Measurement Location and comparison definition	ESPF Method Max. Power in C. V. 15x15 mesh	Method 2 Z-Head using Iotech and SGI system	Method 3 Z-Head HP Analyzer cross spec. technique
Shaker 1 (source) mW	+0.7466	+0.8102	+0.7866
Shaker 2 (sink) mW	-0.5041	-0.5159	-0.4464
% diff. compared to Method 1 (gage 1, gage 2)	------- -------	+8.52 +2.34	+5.36 -11.44
% diff. compared to Method 2 (gage 1, gage 2)	-7.85 -2.29	------- -------	-2.91 -13.47
% diff. compared to Method 3 (gage 1, gage 2)	-5.09 +12.90	+3.00 +15.56	------- -------

The impedance heads were removed and replaced between the 79.0 Hz and 311.0 Hz tests. During the replacement, the impedance heads were attached with slightly different torque values which caused slight changes in the calibration factors. The calibration factors used in the 311.0 Hz case are shown in Table 5.8.

Table 5.8. Force gage calibration constants used to compute the values in Table 5.7

Transducer	Force Cal. Factor	Accel. Cal. Factor
Gage 1	125 mv/lb	102.5 mv/g
Gage 2	114 mv/lb	100.5 mv/g

5.4.3 909.0 Hz Case

The 909.0 Hz case is another off-resonance case. The purpose for showing this case as well as the 1100.0 Hz case is to illustrate the ability of the ESPF method to map the power-flow path at higher frequencies.

The plate was scanned from three different locations for a total of five scans. Table 5.9 lists the laser position relative to the plate in structure-to-laser coordinates as well as the number of points taken in each scan. The coordinates are shown in meters.

Table 5.9. Laser positions and scan densities for the five scans at 909.0 Hz

	x coord. (m)	*y* coord. (m)	*z* coord. (m)	Scan Density
Scan 1	1.7565	0.0888	0.9922	103 x 68
Scan 2	1.7565	0.0888	0.9922	102 x 67
Scan 3	-1.2969	1.2251	1.1338	108 x 68
Scan 4	-1.2969	1.2251	1.1338	107 x 62
Scan 5	-1.4220	0.8563	2.8998	105 x 126

Figure 5.26 illustrates the real and imaginary velocity-field components and Figure 5.27 illustrates the velocity magnitude. The velocity fields in these figures were obtained by using an 18x18 element model. The boundary conditions in this case are clearly not perfectly simply supported. This result was also verified after the scanning process had been performed by physically touching the boundaries while the plate was being excited. While touching the plate at the boundaries a definite transverse vibration could be felt.

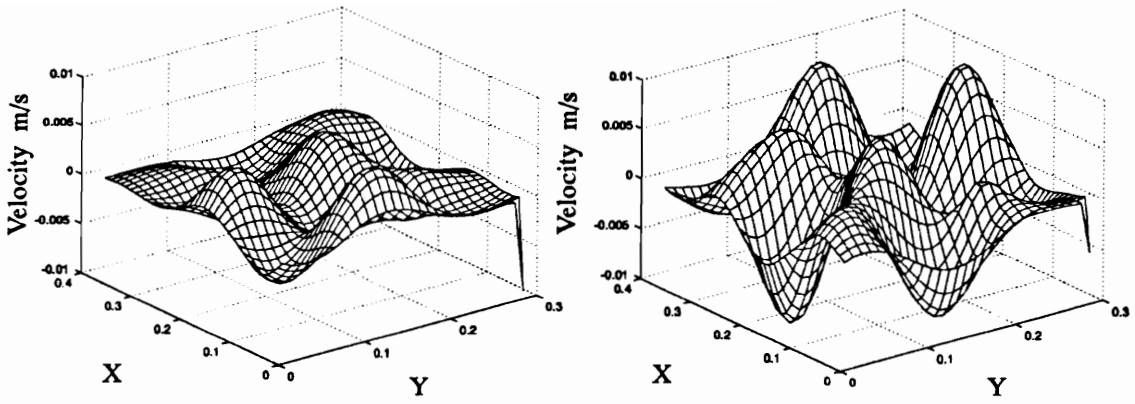

Real Velocity Component

Imaginary Velocity Component

Figure 5.26. Real and imaginary velocity components at 909.0 Hz

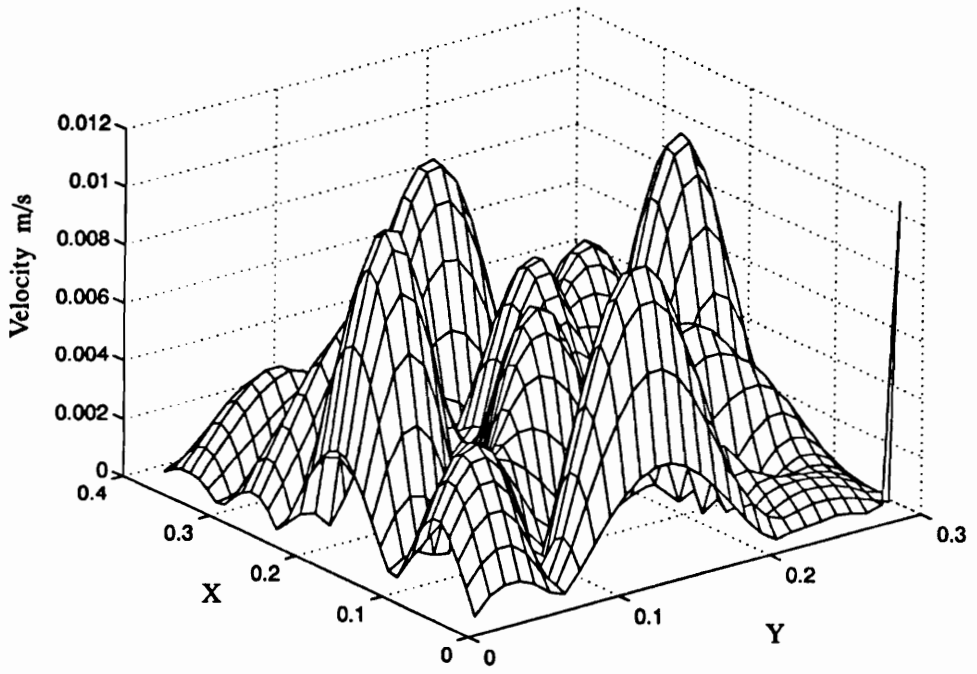

Figure 5.27. Velocity magnitude at 909.0 Hz

The residuals for the real and imaginary velocity components are shown in Figs. 5.28 and 5.29. In the previous two cases it was shown that several mesh densities provided very good results. However, these plots clearly indicate that the 15x15 element mesh provides the "best" representation of the velocity field.

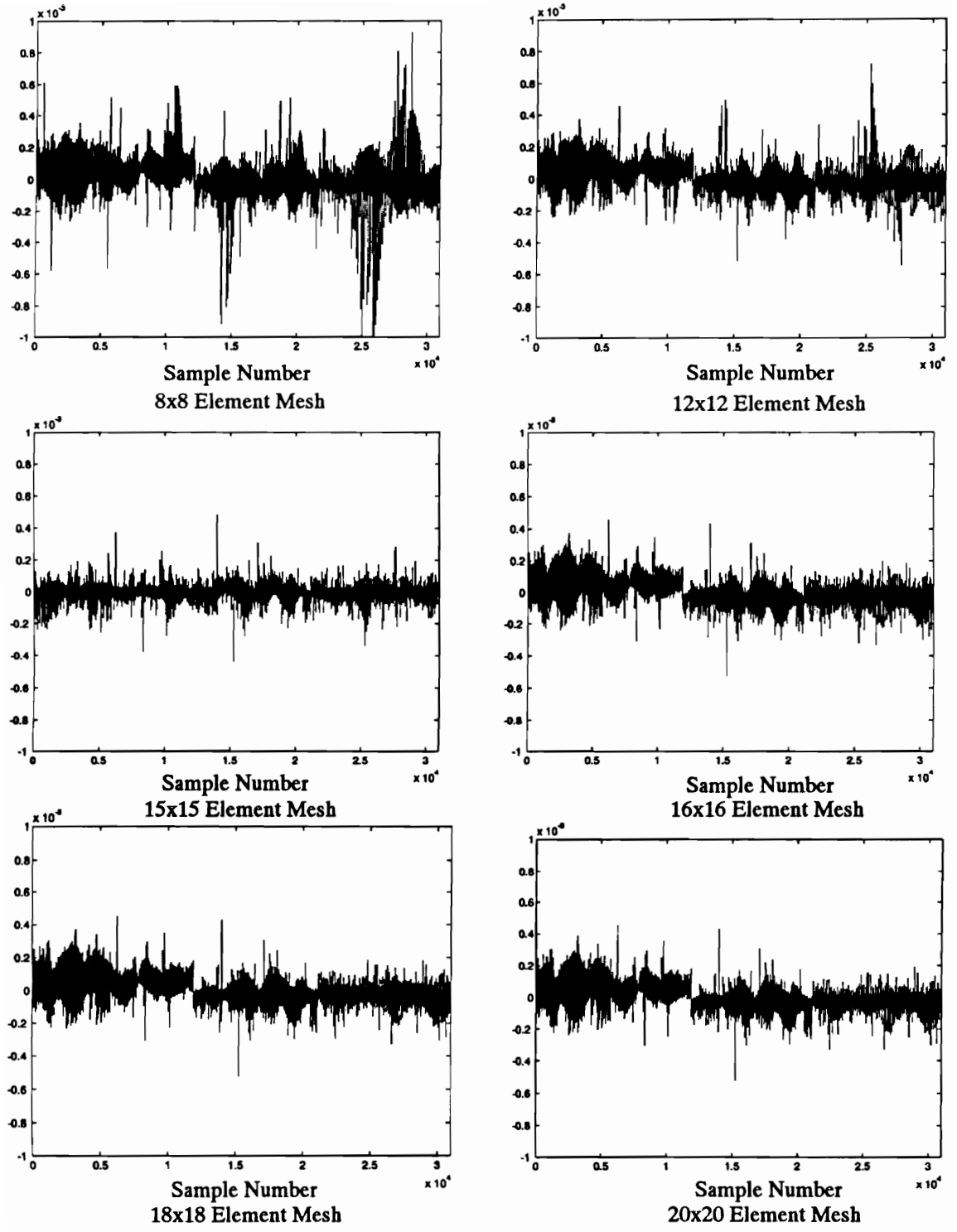

Figure 5.28. Residuals for the real velocity (m/s) component at 909.0 Hz and mesh configurations of 8x8, 12x12, 15x15, 16x16, 18x18, and 20x20

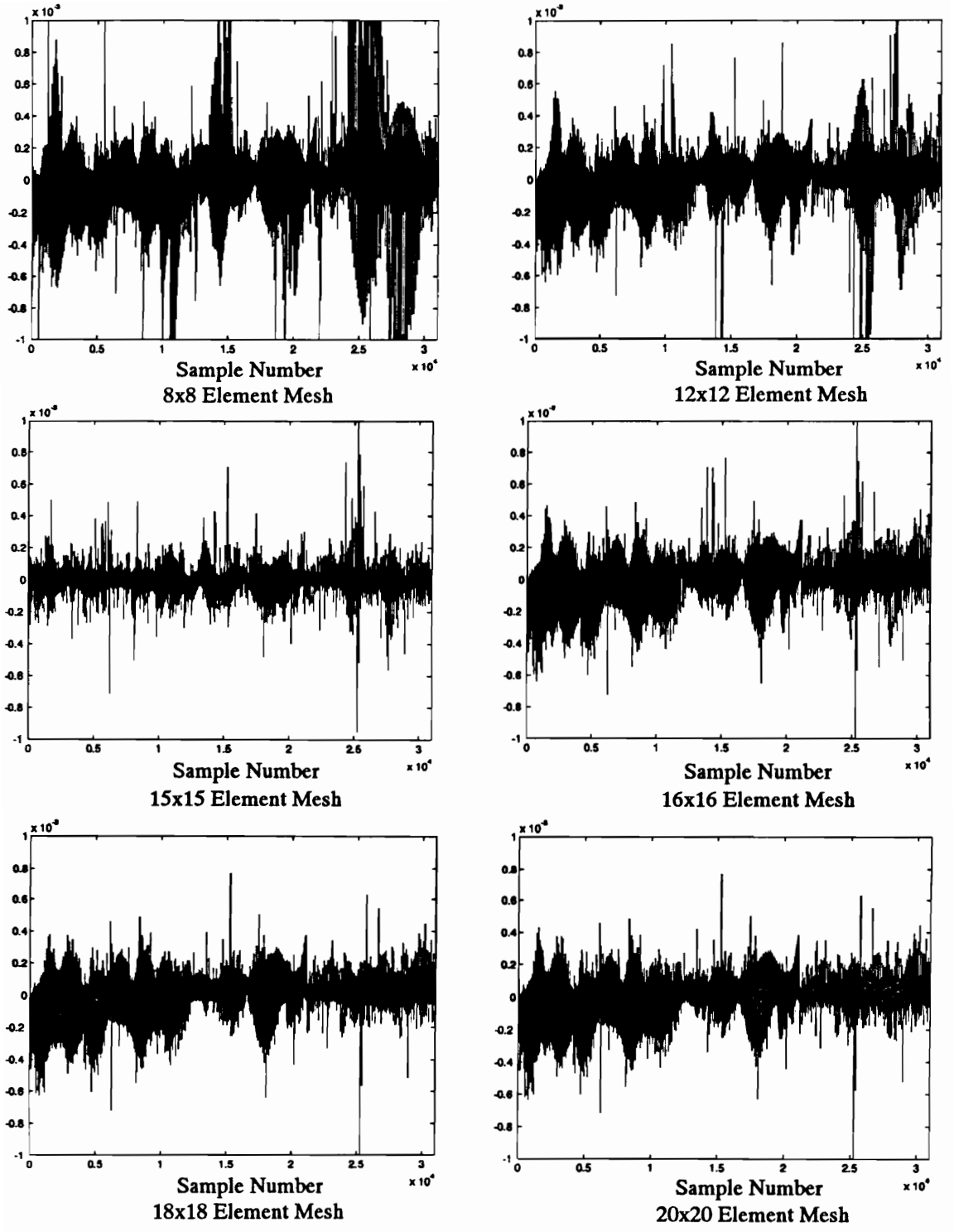

Figure 5.29. Residuals for the imaginary velocity (m/s) component at 909.0 Hz and mesh configurations of 8x8, 12x12, 15x15, 16x16, 18x18, and 20x20

Table 5.10 summarizes the results obtained from the residual computations. From this table it is clear that the 15x15 element mesh provides the "best" representation of the velocity field in that the residuals between the laser data and the ESDM velocity model are minimized.

Table 5.10. Summary of the velocity residual statistics for the 909.0 Hz case

Mesh	Real Velocity Component		Imaginary Velocity Component		Velocity Magnitude	
	Mean	Std.	Mean	Std.	Mean	Std.
8x8	1.874e-6	7.227e-5	-3.636e-6	1.612e-4	1.024e-4	1.44-e-4
12x12	1.756e-6	6.744e-5	-4.533e-6	1.237e-4	1.003e-4	9.910e-5
15x15	-1.370e-6	3.114e-5	6.118e-7	5.147e-5	3.745e-5	4.710e-5
16x16	1.218e-6	5.518e-5	-2.823e-6	9.586e-5	6.791e-5	8.736e-5
18x18	1.118e-6	5.199e-5	-2.704e-6	8.849e-5	5.977e-5	8.349e-5
20x20	1.003e-6	4.845e-5	-2.271e-6	8.297e-5	5.213e-5	8.075e-5

The total power component and the magnitude of the velocity field are shown in Fig. 5.30. This power-flow plot is much more complicated than the previous cases where the power was shown to be in a direct flow path from the source to the sink. In this case, it appears as though the shakers act as both a source and sink. In the areas near the two shakers where large power vectors appear to dead end into each other is where significant acoustic radiation is generated.

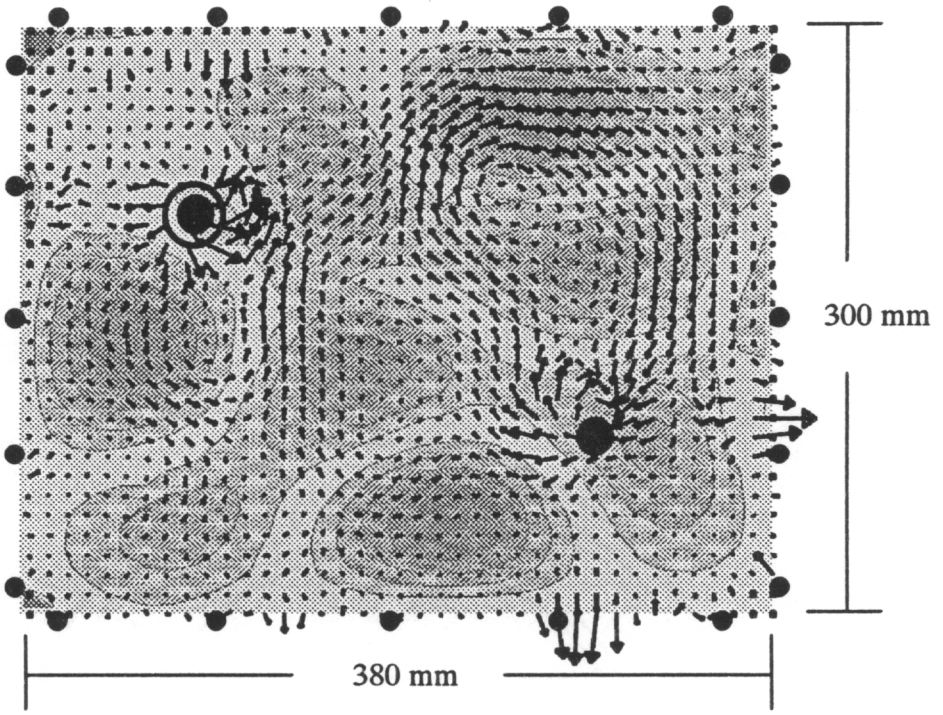

Figure 5.30. Power-flow vector plot and velocity field at 909.0 Hz

Figure 5.31 is the same power plot as shown in Fig. 5.30 but on a different scale to better illustrate the small power-flow paths which develop in the plate. The general flow of the power through the high points of the velocity field should be noted. It is further observed that the power-flow paths are continuous and that no unexplainable or interrupted power-flow paths are present. In this power model, several of the power vectors in the corners of the plate were set to zero as indicated by the small round black dots. These vectors became very large due to the velocity-field solution obtained on the plate boundaries.

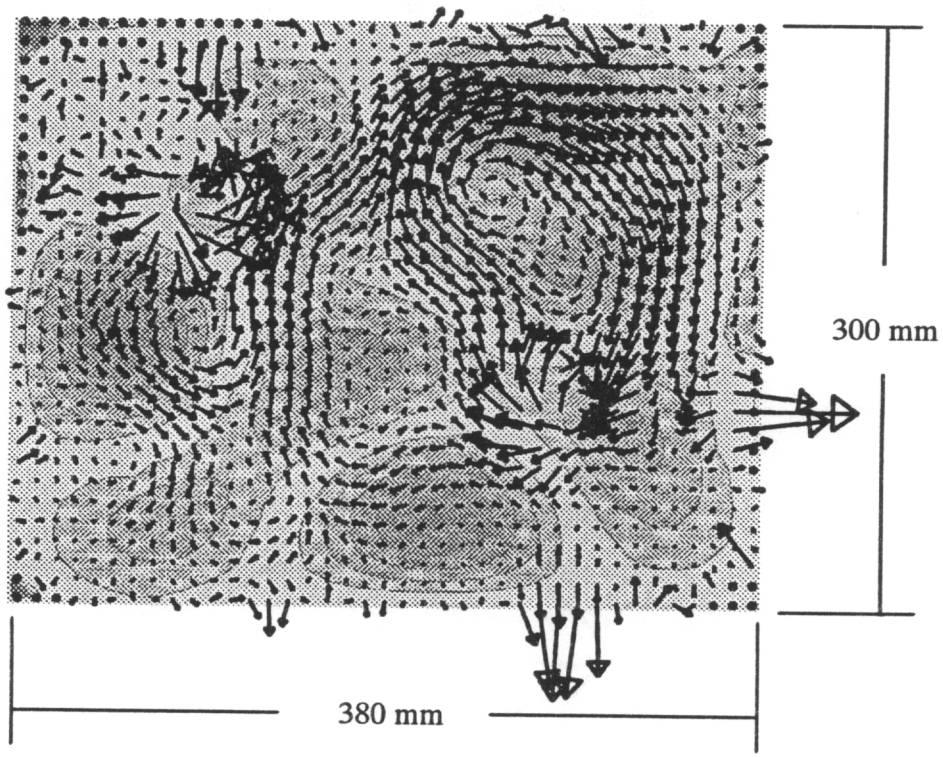

Figure 5.31. Enlarged power-flow vector plot and velocity field at 909.0 Hz

A similar convergence analysis was performed for the 909.0 Hz case as was performed for the previous two frequencies. The results are not as conclusive as the results from the other three cases. Figure 5.32 illustrates the convergence process for shaker 2 at 909.0 Hz. This figure shows that the model continues to converge both in magnitude and spatially up through the 18x18 element mesh. The 20x20 element mesh illustrates that the solution is starting to diverge and the resolving power in the model has become too great and noise in the model is beginning to be represented. The maximum power in the 18x18 element model is shown to occur at a radius of 1.5 cm from the center of the source. Given that the impedance head mount plates have a 1 cm radius it can be concluded that the maximum power was computed to within a radial distance of 0.5 cm. The circle surrounding shaker 2 in Fig. 5.30 represents the control volume where the maximum power was computed. This is an impressive result.

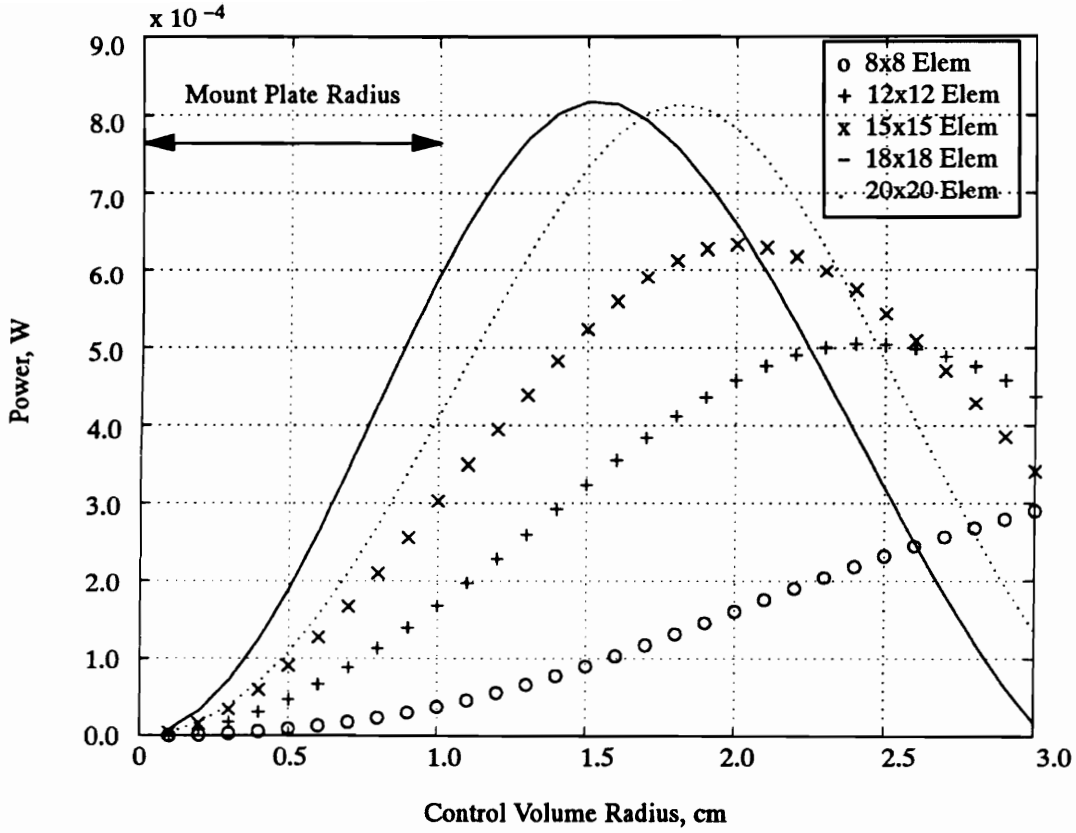

Figure 5.32. Power in each control volume around shaker 2 at 909.0 Hz

The magnitude of the power computed by the 18x18 element model was 0.817 mW. Table 5.11 summarizes the power magnitudes computed by all three methods. The maximum power values are shown in units of mW. The percent difference between these values are also listed in the table. The calibration factors used to compute the power in Methods 2 and 3 were the same as those used in the 311.0 Hz case and are given by Table 5.8.

Table 5.11. Comparison of the maximum power computed by the ESPF method and the injected power and absorbed power computed by Methods 2 and 3 at 909.0 Hz

Power Measurement Location and comparison definition	ESPF Method Max. Power in C. V. 18x18 mesh	Method 2 Z-Head using Iotech and SGI system	Method 3 Z-Head HP Analyzer cross spec. technique
Shaker 2 (sink) mW	+0.817	+0.685	+0.665
% diff. compared to Method 1 (gage 2)	-------	-16.16	-18.60
% diff. compared to Method 2 (gage 2)	+19.27	-------	-2.91
% diff. compared to Method 3 (gage 2)	+22.86	+3.01	-------

When performing the convergence analysis for the power around shaker 1 it was found that the results were extremely sensitive to the spatial location of the center of the control volumes. By reexamining Figs. 5.30 and 5.31 it is clearly evident that the location of the center of the control volumes around shaker 1 would have a large effect on the results due to the large power vectors which occur in all directions around the shaker. It can be understood that slight misplacement of the center of the control volumes could result in significant differences in the net power computed in each control volume. When comparing the power vectors surrounding shaker 1 and shaker 2, it is evident that shaker 2 appears much more like a regular source in that the power is projected in an outward direction all around the source. Around shaker 1 however, this does not occur.

To illustrate the variance in the results and the dependance on the x and y positions of the center of the control volumes, several control volumes at slightly different center locations were investigated. Table 5.12 summarizes the results by showing the x and y coordinates, the peak power computed, and the radial distance at which the peak power was computed. The x and y coordinates are shown in units of meters. The power is shown in units of mW, and the radial distances from the center of the control volumes are shown in cm. From

the results obtained from shaker 2 it would be expected that the maximum power would occur within approximately 1.5 to 2.0 cm from the center of the impedance head mount plates. However, the power results which closely correspond to the power results in magnitude obtained from Methods 2 and 3, indicate that this radius is actually around 3.0 cm. The first two positions shown in Table 5.12 show what would be expected for the radius where the maximum power occurs but the magnitudes are of the opposite sign from what would correspond to the results from Methods 2 and 3. From these results it is impossible to make any definite conclusions other than the fact the power magnitudes computed are mostly within 30% of the power computed by Methods 2 and 3. Again, The difficulties in computing the maximum power at shaker 1 are due to the inability of the ESPF method to compute the power right at a source or sink and the fact the power-flow path at 909.0 Hz corresponds to a complicated flow pattern which puts shaker 1 in the middle of the major power-flow path. Even though the power at shaker 1 could not be compared very effectively to the power computed by Methods 2 and 3, this power model is still determined to be a good representation due to the results obtained for the convergence around shaker 2.

Table 5.12. Control volume results for shaker 1 at 909.0 Hz

x coord. (m)	*y* coord. (m)	max. or min. power	radial distance (cm)
0.281	0.100	+0.35	1.6
0.285	0.101	+0.15	1.6
0.287	0.102	–0.3	3.0
0.287	0.107	–0.4	2.4
0.289	0.105	–0.37	3.0
0.290	0.106	–0.5	2.5
0.291	0.107	–0.54	2.0
0.293	0.110	–0.6	2.0

5.4.4 1100.0 Hz Case

The last frequency presented was an off-resonance frequency of 1100.0 Hz. The shakers were tuned such that shaker 2 lagged shaker 1 by 171.78 degrees and had a magnitude of 92.1% of shaker 1. The plate was scanned at five different laser positions for a total of eight scans. The laser positions in units of meters and the scan densities are shown in Table 5.13.

Table 5.13. Laser positions and scan density for the eight scans at 1100.0 Hz

	x coord. (m)	*y* coord. (m)	*z* coord. (m)	Scan Density
Scan 1	0.2329	0.6261	3.4772	110 x 135
Scan 2	1.8481	0.0892	1.0753	107 x 147
Scan 3	1.8481	0.0892	1.0753	109 x 68
Scan 4	-1.2955	1.1011	1.1778	103 x 172
Scan 5	-1.2955	1.1011	1.1778	102 x 73
Scan 6	1.4863	0.9827	3.2362	112 x 148
Scan 7	0.5891	1.1974	1.3781	62 x 122
Scan 8	0.5891	1.1974	1.3781	61 x 107

Figure 5.33 illustrates the real and imaginary velocity components and Figure 5.34 illustrates the velocity magnitude. The velocity fields in these figures were obtained by using a 15x15 element mesh. Again, the boundary conditions do not represent a perfect simply supported plate.

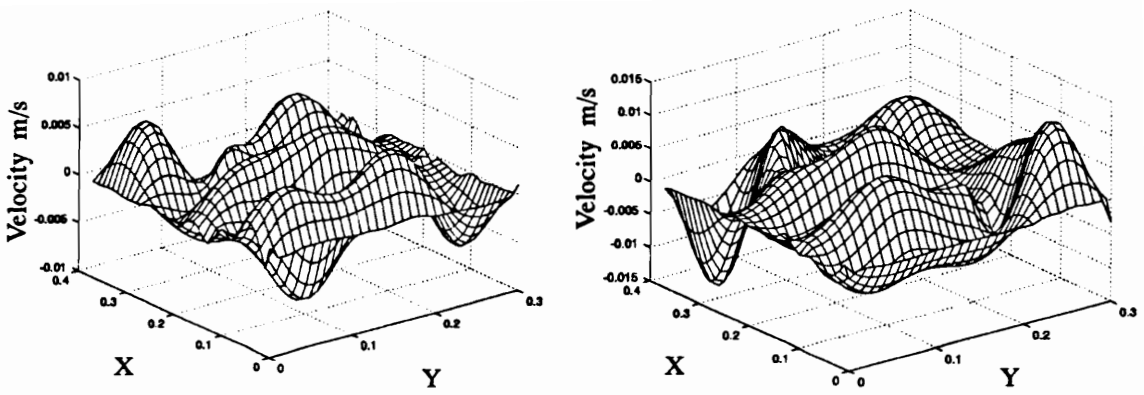

Real Velocity Component

Imaginary Velocity Component

Figure 5.33. Real and imaginary velocity components at 1100.0 Hz

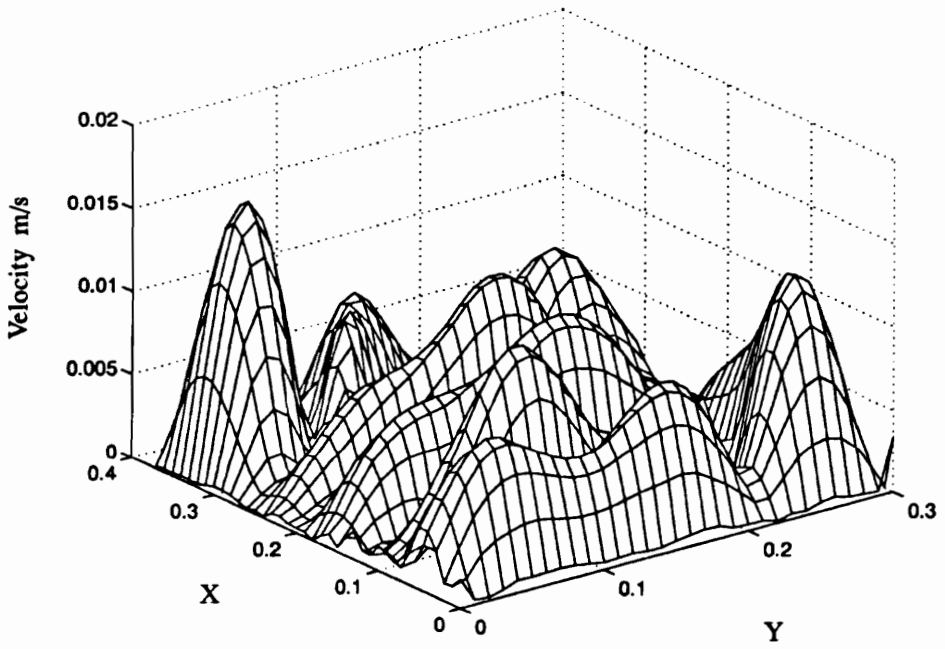

Figure 5.34. Velocity magnitude at 1100.0 Hz

The residuals of the real and imaginary velocity for an 8x8, 12x12, and a 15x15 element model are shown in Figs. 5.35 and 5.36. These figures indicate that the 8x8 element mesh does not represent a converged velocity field. However, the 12x12 and the 15x15 element models provide very similar results which indicate that a converged solution has been ob-

tained. Even though a considerable amount of laser data was acquired during the scanning process as indicated by Table 5.13, there was only sufficient coverage in the extreme corners of the plate to compute a 15x15 element model.

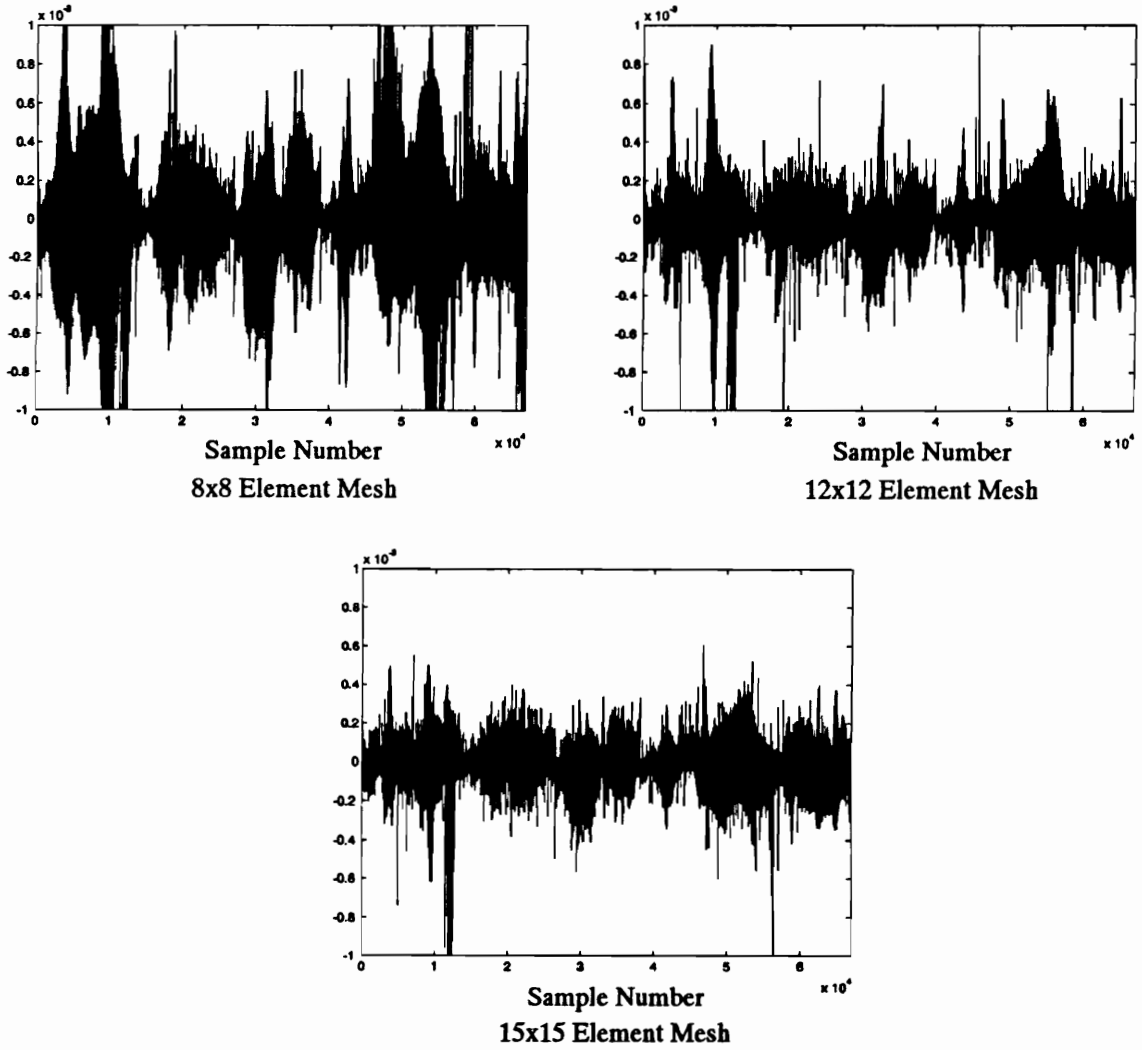

Figure 5.35. Residuals for the real velocity (m/s) component at 1100.0 Hz and mesh configurations of 8x8, 12x12, and 15x15

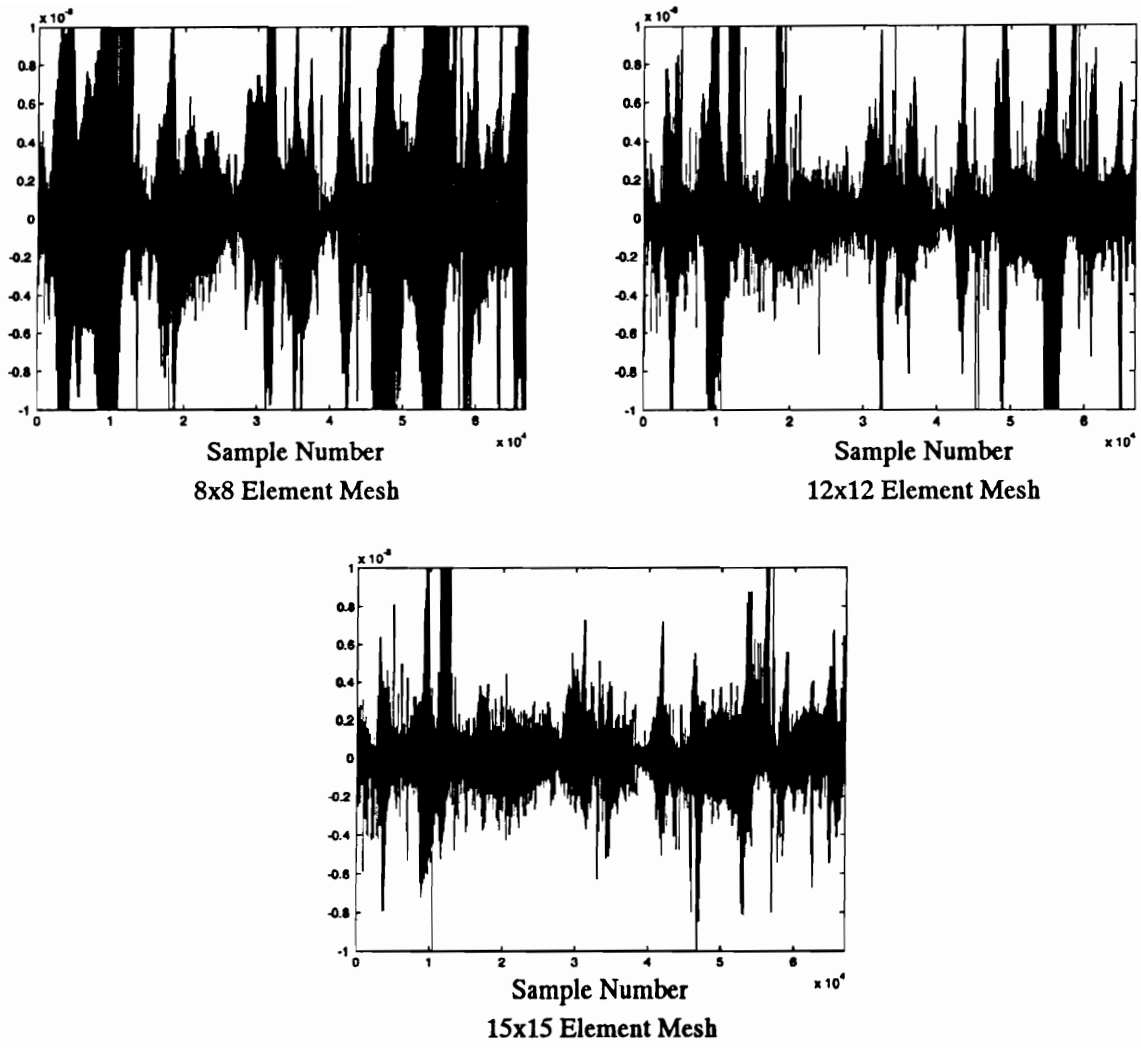

Figure 5.36. Residuals for the imaginary velocity (m/s) component at 1100.0 Hz and mesh configurations of 8x8, 12x12, and 15x15

A summary of the statistics of the velocity residuals is shown in Table 5.14. This table indicates that the 15x15 element mesh provides the "best" results on the basis that it is the model with the smallest residuals. It is expected however, that if more laser data had been acquired a higher order mesh density would have provided, as good and possibly even better results.

Table 5.14. Summary of the velocity residual statistics 1100.0 Hz

Mesh	Real Velocity Component		Imaginary Velocity Component		Velocity Magnitude	
	Mean	Std.	Mean	Std.	Mean	Std.
8x8	-1.090e-5	2.141e-4	1.462e-5	3.395e-4	2.582e-4	3.078e-4
12x12	-7.451e-6	1.195e-4	1.112e-5	1.938e-4	1.372e-4	1.821e-4
15x15	-5.788e-6	1.0244e-4	7.995e-6	1.472e-4	1.126e-4	1.399e-4

Figure 5.37 illustrates the power flow in the plate. The magnitude of the velocity field is again superimposed to give the operating shape of the plate at 1100.0 Hz. From this plot it is clearly evident that two sources of energy exist in the plate. It is further noted that the largest vectors appear very close to the actual location of the source. The black dots that indicate the relative size and location of the two shaker mount plates have been removed to improve the clarity. Figure 5.37 shows that most of the power from both shakers enters the plate, flows directly to the neighboring boundary, and is absorbed into the heavy steel frame used to support the plate. It is also noted that the large power vectors which occur on the boundaries near the shakers exist in both the 909.0 Hz case and the 1100.0 Hz case.

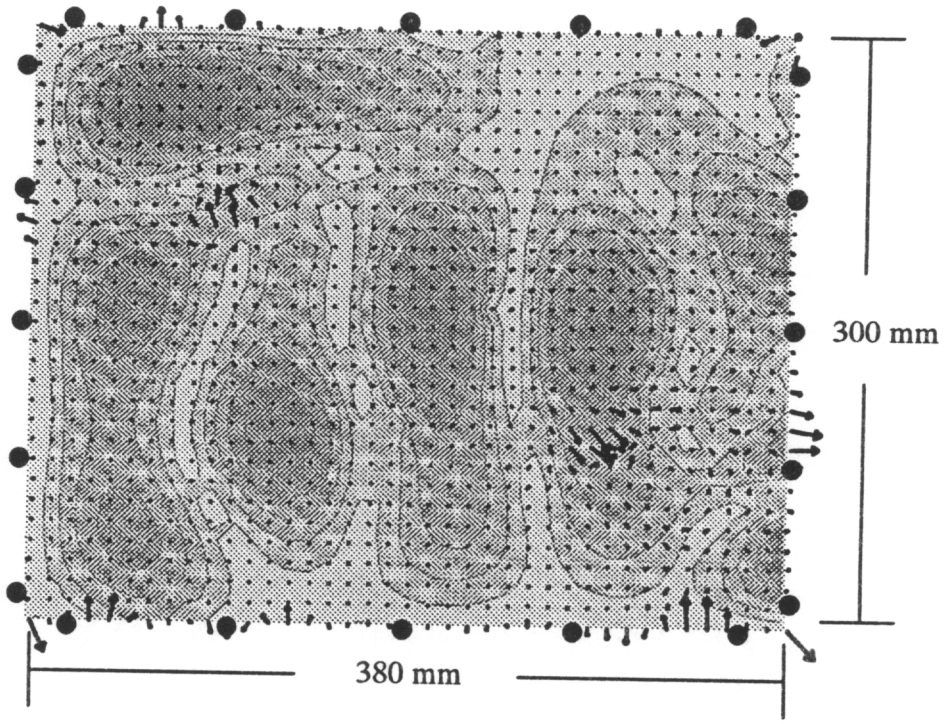

Figure 5.37. Power-flow vector plot and velocity field at 1100.0 Hz

To more clearly visualize the small energy paths which develop in the plate, the power was plotted using a larger scale factor as shown in Fig. 5.38. This figure indicates that a rather complex flow of power exists in the plate at this frequency. However, the flow is still shown to pass through the areas of high velocity potential.

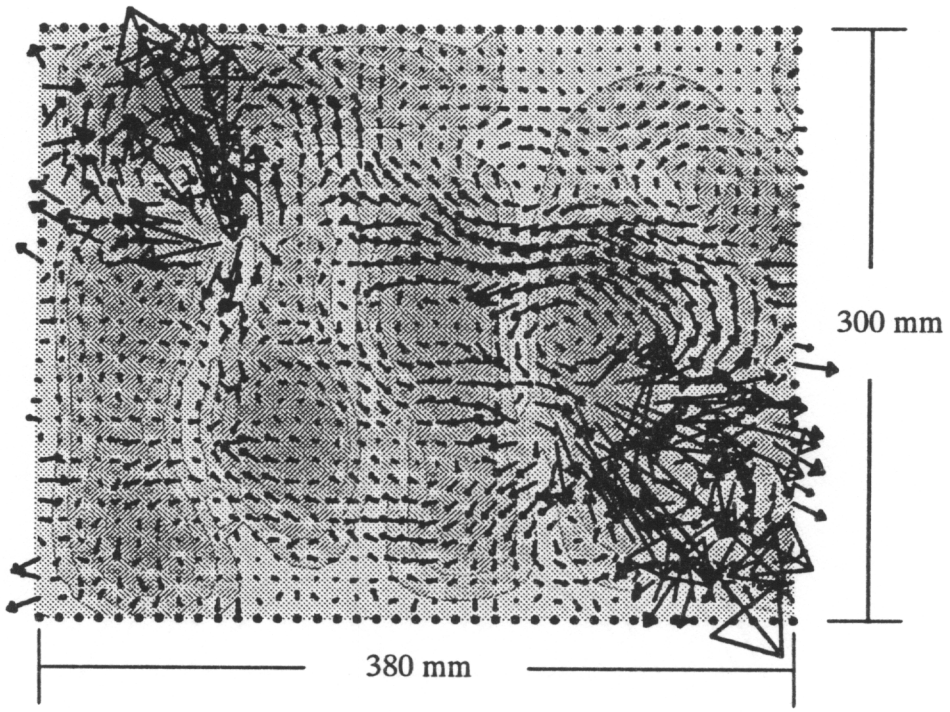

Figure 5.38. Power-flow vector plot and velocity field at 1100.0 Hz

As in the previous cases, to ensure that an accurate model of the power in the plate was obtained a convergence analysis was performed. Figure 5.39 illustrates the convergence results for shaker 1. In these models it is shown that the 8x8 element model more closely represents the appropriate magnitude but has a larger spatial error compared to the 12x12 element model. However, the "best" model over all, based on the convergence of the power around shaker 1, is shown to be the 15x15 element model.

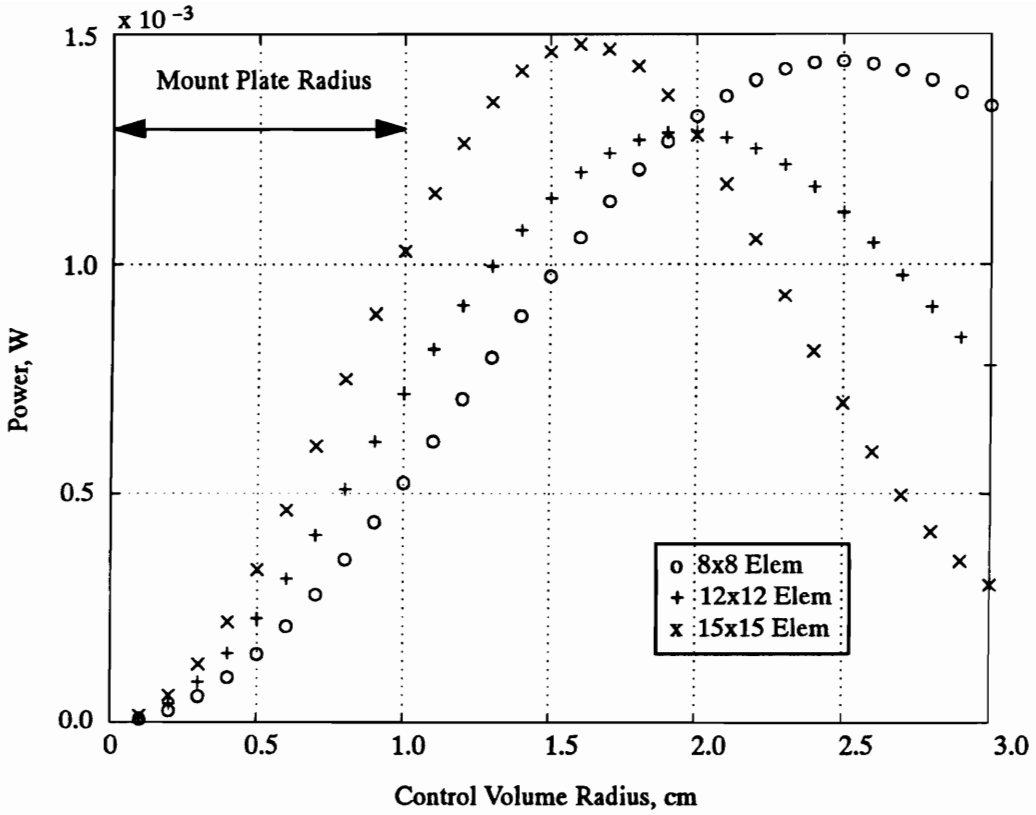

Figure 5.39. Power in each control volume around shaker 1 at 1100.0 Hz

Figure 5.40 illustrates the power convergence for shaker 2. In this case, unlike the power models around shaker 1, the 12x12 element model is considerably better than the 8x8 element model in the representations of both the magnitude and spatial location of the maximum power. Again, the 15x15 element model provides the "best" model of the power in the structure. These figures also indicate that the spatial error in the maximum power computation for shaker 1 was 6 mm and for shaker 2 was only 3 mm. These results could possibly have been improved had more laser data been acquired which would have allowed a finer mesh to be applied.

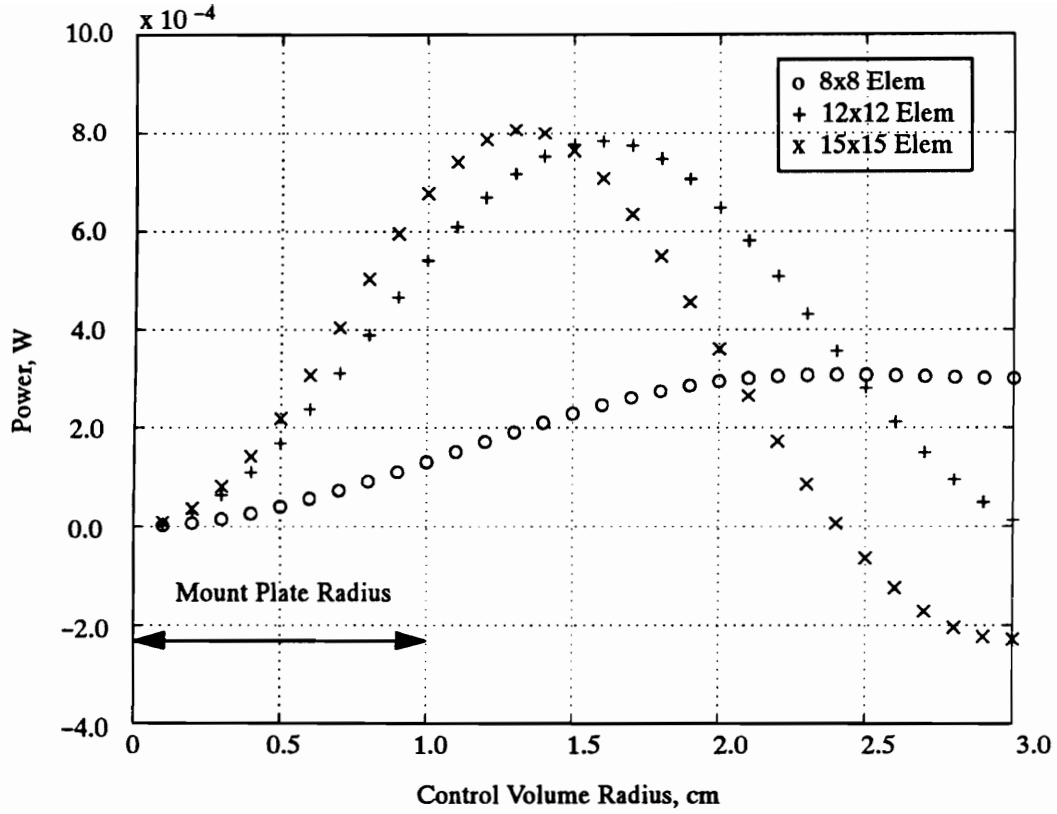

Figure 5.40. Power in each control volume around shaker 2 at 1100.0 Hz

Table 5.15 summarizes the percent differences between the three methods. It is shown that the power computed by Methods 2 and 3 compare very closely at both shaker 1 and shaker 2. It is further shown that the power computed by the ESPF method at shaker 2 compares to within 2.0% of the power computed by Methods 2 and 3. The power computed by the ESPF method at shaker 1 does not compare as closely as the power computed at shaker 2 but this could be due to not being exactly aligned with the source as discussed in the 909.0 Hz case.

Table 5.15. Comparison of the maximum power computed by the ESPF method and the injected power and absorbed power computed by Methods 2 and 3 at 1100.0 Hz

Power Measurement Location and comparison definition	ESPF Method Max. Power in C. V. 15x15 mesh	Method 2 Z-Head using Iotech and SGI system	Method 3 Z-Head HP Analyzer cross spec. technique
Shaker 1 (source) mW	+1.477	+1.733	+1.720
Shaker 2 (sink) mW	+0.808	+0.819	+0.822
% diff. compared to Method 1 (gage 1, gage 2)	------- -------	+17.33 +1.49	+16.45 +1.86
% diff. compared to Method 2 (gage 1, gage 2)	-14.77 -1.34	------- -------	-0.75 +0.37
% diff. compared to Method 3 (gage 1, gage 2)	-14.13 -1.70	+0.76 +0.37	------- -------

Table 5.8 lists the force gage and accelerometer calibration constants which were used in Methods 2 and 3 to compute the power. Since the gages were not removed from the plate and no adjustments took place between the 1100.0 Hz case and the 311.0 Hz these values are the same as those used in the 311.0 Hz case.

5.5 Chapter Summary

Four different frequencies have been used to validate the ESPF method. The first frequency of 79.0 Hz corresponded to a near-resonance frequency. The other three frequencies of 311.0 Hz, 909.0 Hz, and 1100.0 Hz corresponded to off-resonance frequencies. The results from all four frequencies illustrate the ability of the ESPF method to provide accurate models of the power in the plate.

In each power-flow vector plot the power flow followed the general trend of flowing through the areas of high velocity. This same phenomena has been observed by other researchers [31]. For the low frequency cases the general power-flow path can be predicted simply from plots of the velocity field. For example, in the 79.0 Hz case which corresponds

closely to the first mode of the plate it should be expected that the main flow of energy will pass directly through the center of the plate. Also from the velocity field obtained for the 311.0 Hz case it should be expected that most of the energy will flow along the bottom of the plate through the high velocity area and then up to the sink. In the higher frequency cases this method of predicting the power-flow paths is much more complicated. However, by studying the figures this same result is manifested in both the 909.0 Hz case and the 1100.0 Hz. This is another verification that the ESPF method is capable of representing an accurate power-flow map.

The maximum power computed by the ESPF method compared to within 12% in the 79.0 Hz case and to within 9% in the 311.0 Hz case. Considering the possible causes of differences in the results, such as calibration errors, material property and plate dimension uncertainties, and measurement errors in the registration process and the location of the impedance head mount plates, these results are very encouraging and clearly demonstrate that the ESPF method has the ability to accurately measure the power in a vibrating plate. The spatial errors at which the maximum power was computed was 3.4 cm for the 79.0 Hz case and 2.4 cm in the 311.0 Hz case.

At the lower frequencies the magnitudes and spatial error were easily computed by using the control volume approach. This is mainly because the power-flow paths were somewhat direct from one shaker to the other. In the higher frequency cases the power did not correspond as well in magnitude to the power computed by Methods 2 and 3. However, the spatial error at where the maximum power occurred was greatly reduced. The magnitudes did not compare as closely due mainly to the sensitivity of where the centers of the control volumes were placed. The spatial error decreased due to the fact that at the higher frequencies the mode shape helped the shear forces be represented more accurately. In the low-frequency cases a relatively smooth representation of the force was obtained because the mode shape corresponded to a low mode. However, in the higher frequency cases, the

increased spatial wave number helped the shear forces be more accurately modeled. It should be noted that the spatial error does not imply that the location of the source was off by this distance. It implies that the net maximum power crossing a control volume was obtained at the given distance away from the true center of the source. The center of the source is still correctly determined by the ESPF method. It is simply a matter of a smoother representation of the shear force which causes the power to reach a maximum slightly away from the center of the source.

In conclusion, it has been clearly shown by four different cases that the ESPF method provides both an accurate representation of the power magnitudes and spatial locations of the power sources and sinks. This close comparison between the power computed by the ESPF method and the injected power computed by Methods 2 and 3 defines a new standard of measure for experimental power methods. Other experimental power methods have been deemed validated by their developers by simply showing that their method determines whether power is being injected or extracted by the external shaker. They do not even attempt to compare power values.

Chapter 6

Summary

6.1 General Summary

As demands for stronger, faster, and lighter designs continue to push technology new methods of design will be developed. This dissertation presented one such method which is based on mapping the power flow in vibrating structures. Power-flow maps provide similar information for dynamic structures as load paths and free-body diagrams provide for static structures. The power-flow map indicates where energy is entering the system, leaving the system, and the transmission paths through the structure. This information provides significant insight to the design or control of the structure. Many analytical and experimental power-flow techniques have been developed through the years. These two methods each provide certain capabilities and suffer from certain deficiencies.

The analytical models based on the finite element approach can provide spatially continuous power results. These methods also allow relatively large frequency ranges to be investigated relatively quickly compared to the experimental methods. However, once the frequency becomes too high, the order of the elements or the number of the elements required in the model render the finite element methods inefficient and expensive. SEA is an analytical ap-

proach which was developed to overcome the high frequency deficiencies of the finite element models. SEA, however, does not provide a detailed spatial map of the power in the structure. The main deficiencies in both the finite element methods and SEA is the inability to accurately model the boundary conditions, material loss factors, and near-field effects. In real applications, which often consist of complex structures, these parameters can be extremely difficult to model.

The experimental models represent the true system dynamics in that the boundary conditions and near-field effects are measured. However, due to the complexity in acquiring the measurements many experimental models neglect the near-field and only compute the power in the far-field. The most significant deficiency in the experimental methods is the inability to provide a spatial model of the power in the structure. In most experimental techniques the velocity is measured at a few discrete points and a finite difference approach is used to compute the power over the entire structure.

The ESPF approach presented in this dissertation is novel in that it combines the strengths of the analytical methods and the experimental methods. The ESPF technique develops a spatially continuous power model derived from spatially dense measurements of the velocity field over the entire structure. The ESPF method, therefore, captures the response imposed by the true boundary conditions and the near-field effects and provides a spatially continuous model of the power.

Chapter 3 of this dissertation presented the theoretical development of the ESPF method. The current capabilities of the ESPF method are derived from the deformation models for Bernoulli-Euler beams and Love-Kirchoff plates. The method is also limited to computing the power due to transverse motion only. However, the extension to more complex mechan-

ics models is simply a matter of deriving the equations for the generalized forces and velocities in terms of the displacements and incorporating them into the ESPF method. The mechanics to compute the power due to in-plane motion have also been developed. The difficulties in computing the power due to in-plane motion lie in the ability to extract accurate models of the in-plane velocity with the current SLDV system. Once the capabilities to accurately model the in-plane velocity have been acquired, the extension of the ESPF method to compute the power due to in-plane motion is straight forward.

Chapter 4 validated the ESPF method based on simulated laser data. The simulated laser data provided the ability to control the amount of noise in the ESDM velocity model. In a 1 m simply supported beam model it was shown that the maximum power computed by the ESPF method compared to a purely analytical (exact) method to within a 6.25% error in magnitude and a 5 cm spatial error. It was further explained that a more converged mesh would provide even better results. In the same comparison for a 1.0 m x 0.7 m simply supported plate the power computation was shown to have a magnitude error of 1.3% and a 6 cm radial spatial error. It should be noted that in both the beam and plate cases the spatial error does not imply that the location of the source was off by this distance. It implies that the net maximum power crossing a control volume was obtained at the given distance away from the true center of the source. The center of the source is still correctly determined by the ESPF method. It is simply a matter of a smoother representation of the shear force which causes the power to reach a maximum slightly away from the center of the source. These results were very encouraging and lead to the next step which consisted of using the ESPF method to compute the power using experimental data.

The power results for an experimental simply supported plate forced with two shakers at frequencies of 79.0 Hz, 311.0 Hz, 909.0 Hz and 1100.0 Hz were presented in Chapter 5. In most cases one of the shakers acted as a source and the other as a sink. Three methods were used to compute the power in the plate and the results were compared. Method 1 consisted of using the ESPF approach to compute the power. Method 2 consisted of using data from the impedance heads attached to the shakers to compute the injected power. In Method 2 the data was collected with the same software and hardware as the data in Method 1. Method 3 consisted of computing the power using the imaginary component of the cross spectrum between the force and acceleration signals given by the impedance heads.

In the 79.0 Hz case the magnitude of the injected power was shown to compare within 11.84% between all three methods. The power extracted from the system was shown to compare within 12.25% between all three methods. The maximum power computed by the ESPF was shown to occur at a radius of 4.4 cm from the center of the source. This distance is 3.4 cm larger than a "perfect" representation of the force would have provided.

In the 311.0 Hz case the magnitudes of the injected and extracted power were shown to compare within 8.52% and 13.47% respectively. The maximum power in the ESPF method was computed at a radial distance of 2.4 cm larger than the actual area over which the force was applied. This distance is significantly less than the distance obtained in the 79.0 Hz case.

In the 909.0 Hz case the power extracted from the system was shown to compare in magnitude to within 18.60% at a radial distance of 0.5 cm larger than the actual area over which the force is applied. Due to the complexity of the power-flow path around shaker 1 the center location of the control volume was extremely sensitive to error. Therefore, the control volume approach of comparing the power at this shaker could not be accurately performed.

In the final case of 1100.0 Hz, the power magnitudes at shakers 1 and 2 were shown to compare within 17.33% and 1.86% respectively. The spatial difference in the maximum power computation was under 0.6 cm for both shakers.

Although great care was exercised in the data acquisition process, there are many factors which could cause the differences in these results. For example, calibration errors, material property and geometric uncertainties, imperfect signal processing techniques, and poor laser registration would cause significant errors in the power results.

Due to the results obtained and the possible mechanisms for error, it is concluded that the ESPF method is a very useful tool in predicting the magnitude of the power in vibrating beams and plates. It is further concluded that the ESPF method is more capable of computing the correct magnitude and spatial location of the power than any other experimentally based method reported in the literature. In addition, the ESPF method has the advantages of converging the power model, providing a spatially continuous model, and easy in-field use.

6.2 Future Work

There are several areas in which the ESPF method will be improved. This section briefly outlines these areas.

6.2.1 Test Setup and Data Acquisition

Future improvements in the test setup and data acquisition will consist of both hardware and software developments. Further advances in the hardware will be made by continued use and understanding of the laser capabilities and deficiencies. As laser technology is improved, the ESDM velocity models will be improved which will greatly enhance the power of the ESPF method. For example, one improvement would be to reduce the noise floor of the laser.

This would be done by improving the quality of the photo-detectors and the electronics in the laser system. A competitor of Ometron Inc., claims to have already produced a SLDV which has reduced the noise floor by an order of magnitude. Another major improvement would be the upgrading of the mirror controllers. This would provide better laser pointing capabilities which could greatly improve the laser registration results and the accuracy of the ESDM velocity model. Although the focus of the laser beam is not a major issue on highly retro-reflective surfaces, the development of an auto-focus system could also improve the results especially when scanning large structures or when scanning at high angles of incidence.

The software improvements would consist of developing an automated calibration technique. This would reduce the setup time and improve the calibration quality by applying statistics to the calibration results. In the signal processing stage of the method, a more complex time signal model could be incorporated into the method which would allow for multi-frequency processing. This would reduce the number of scans which would need to be performed when investigating a given frequency range. A time-signal model which included higher harmonics of the forcing frequency could also improve the results by providing a better model of the signal.

6.2.2 Velocity-Field Representation

Currently the ESPF method is constrained to compute the power due to transverse motion in flat beam or plate structures. A significant impact could be made by developing the techniques to compute the power due to in-plane motion. The current inability to compute the in-plane power component is due to both deficiencies in the laser hardware and the ability to acquire highly accurate laser registration results as discussed in Chapter 3. It is postulated

that the main problem with the laser is the accuracy with which the laser beam can be positioned. As the quality of the scanning mirrors is increased the positional accuracy of the laser will also improve. Other components of the laser such as the photo diodes which detect the signal could also be improved which would improve the quality of the signal and reduce the noise floor of the laser. It was clearly demonstrated that given perfect, noise free data, the ESDM technique accurately reconstructs the complete 3-D velocity field. However, under experimental conditions where the out-of-plane component of the velocity field is dominant it has been shown that the in-plane velocity field does not converge. Therefore, in order to compute the power due to in-plane motion the quality of the signal must be improved. Once these two issues have been resolved the ESPF method can easily be extended to compute the power due to in-plane motion.

The ability to compute the power on curved surfaces would require two major developments. The first of these developments would be the implementation of non-uniform rational B-splines or some other technique to accurately model the test structure geometry. The incorporation of non-uniform B-splines would also allow localized mesh refinement. This could significantly improve the power results in the areas of high power input or extraction. The second development would be the incorporation of the signal offset which is computed in the signal processing into the ESDM velocity model solution. This extension would greatly enhance the capabilities of the ESPF method by allowing the power in arbitrary 3-D structures to be computed.

6.3 Final Remarks

The goal of this research was to develop an experimentally based power-flow method which derives a spatially continuous model of the power in vibrating structures. This goal

has been accomplished by the development of the ESPF method. Development of the ESPF method has provided the understanding and vision of where this type of research can eventually lead. Future developments of the ESPF method will continue to have this technique be one of the leaders in the world of experimental power flow.

References

[1] Strean, R. F., "Characterization of Laser Noise in Free-Free Beam Structures Using a Scanning Laser Doppler Vibrometer," Masters Thesis, Virginia Polytechnic Institute and State University, Department of Mechanical Engineering, Blacksburg, VA, 1995.

[2] Montgomery, D. E., "Modeling and Visualization of Laser-Based Three-Dimensional Experimental Spatial Dynamic Response," Ph.D. Dissertation, Virginia Polytechnic Institute and State University, Department of Mechanical Engineering, Blacksburg, VA, 1994.

[3] Lopez-Dominguez, J. C., "Reconstruction of 3-D Structural Dynamic Response Fields: An Experimental Laser-Based Approach with Statistical Emphasis," Ph.D. Dissertation, Virginia Polytechnic Institute and State University, Department of Mechanical Engineering, Blacksburg, VA, 1993.

[4] Doktor, C. A., "Development of a Statistical Method for Validating ESDM Strain-Field Output," Masters Thesis, Virginia Polytechnic Institute and State University, Department of Mechanical Engineering, Blacksburg, VA, 1995.

[5] Moshier, M., "Laser-Based Broad-Band Spatially Dense Automated Data Acquisition System," Masters Thesis, Virginia Polytechnic Institute and State University, Department of Mechanical Engineering, Blacksburg, VA, 1996.

[6] Zeng, X., "The Determination of the Position and Orientation of a Scanning Laser Doppler Vibrometer," Ph.D. Dissertation, Virginia Polytechnic and State University, Department of Mechanical Engineering, Blacksburg, VA, 1994.

[7] Noiseux, D. U., "Measurement of Power Flow in Uniform Beams and Plates," *Journal of the Acoustical Society of America*, Vol. 47, 1970, pp. 238-247.

[8] Lyon, R. H., Statistical Energy Analysis of Dynamical Systems, MIT Press, Cambridge, MA, 1975.

[9] Hsu, K. H., Nefske, D. J., and Akay, A., Statistical Energy Analysis, ASME Winter Annual Meeting, NCA-Vol. 3, 1987.

[10] Maidanik, G. and Dickey, J., "Modal and Wave Approaches to the Statistical Energy Analysis (SEA)," Statistical Energy Analysis, edited by Hsu, K. H., Nefske, D. J., and Akay, A., ASME Winter Annual Meeting, NCA-Vol. 3., 1987, pp. 63-71.

[11] Fahy, F., Sound and Structural Vibration Radiation, Transmission, and Response, Academic Press Limited, San Diego, CA, 1985.

[12] Fahy, F. and White, R. G., Statistical Energy Analysis and Vibrational Power Flow, *Proceedings of the Structural Intensity and Vibration Energy Flow; 3rd International Congress on Intensity Techniques,* 1990, pp. 29-35.

[13] Remington, P. J., and Manning, J. E., "Comparison of Statistical Energy Analysis Power Flow Predictions with an "Exact" Calculation," *Journal of the Acoustical Society of America*, Vol. 57 No. 2, 1975, pp. 374-379.

[14] Woodhouse, J., "An Introduction to Statistical Energy Analysis of Structural Vibration," *Journal of Applied Acoustics*, Vol. 14, 1981, pp. 455-469.

[15] Pavic, G., "Measurement of Structure Borne Wave Intensity, Part I. Formulation of the Methods," *Journal of Sound and Vibration*, Vol. 49, No. 2 1976, pp. 221-230.

[16] Pavic, G., "Measurement of Vibrations by Strain Gauges, Part II: Selection of Measurement Parameters," *Journal of Sound and Vibration*, Vol. 102, No. 2, 1985, pp. 165-188.

[17] Maynard, J. D., Williams, E. G., and Lee, Y., "Nearfield Acoustic Holography: I. Theory of Generalized Holography and the Development of NAH," *Journal of the Acoustical Society of America*, Vol. 78, No. 4, 1985, pp. 1395-1413.

[18] Williams, E. G., and Dardy, H. D., "Nearfield Acoustical Holography Using an Underwater Automated Scanner," *Journal of the Acoustical Society of America*, Vol. 78 No. 2, 1985, pp. 789-798.

[19] Pascal, J. C., Carniel, X., Chalvidan, B. and Smigielski, P., "Determination of Structural Intensity and Mechanical Excitation Using Holographic Interferometry," *Proceedings of the Structural Intensity and Vibration Energy Flow; 4th International Congress on Intensity Techniques*. Senlis, France, 1993, pp. 137-144.

[20] Williams, E. G., Dardy, H. D., and Fink, R. G., "A Technique For Measurement of Structure-borne intensity in plates," *Journal of the Acoustical Society of America*, Vol. 78, No. 6, pp. 2061-2068.

[21] Nefske, D. J. and Sung, S. H., "Power Flow Finite Element Analysis of Dynamic Systems: Basic Theory and Application to Beams," *Journal of Vibration, Acoustics, Stress, and Reliability in Design*, Vol. 111, 1989, pp. 94-100.

[22] Langley, R. S., "Analysis of Beam and Plate Vibrations by Using the Wave Equation," *Journal of Sound and Vibration*, Vol. 150, No. 1, 1991, pp. 47-65.

[23] Centre Technique Des Industries Mecaniques, *Proceedings of the Structural Intensity and Vibration Energy Flow; 3rd International Congress on Intensity Techniques.* Senlis, France, 1990.

[24] Hambric, S. A., "Influence on Different Wave Motion Types on Finite Element Power Flow Calculations," *Proceedings of the Structural Intensity and Vibration Energy Flow; 3rd International Congress on Intensity Techniques*, 1990, pp. 215-222.

[25] Gavric, L., Carniel, X., and Pavic, G., "Structure-Borne Intensity Fields in Plates, Beams, Plate-Beam Assemblies," *Proceedings of the Structural Intensity and Vibration Energy Flow; 3rd International Congress on Intensity Techniques*, 1990, pp. 223-229.

[26] Carroll, G. P., "Phase Accuracy Considerations for Implementing Intensity Measurements in Structures," *Proceedings of the Structural Intensity and Vibration Energy Flow; 3rd International Congress on Intensity Techniques,* 1990, pp. 241-247.

[27] Carroll, G., P., "Structural Response and Power Flow Measurements Utilizing Cross Spectra," Ph.D. Dissertation, The Catholic University of America, Washington, D.C., 1987.

[28] McDevitt, T. E., Koopmann, G. H., and Burroughs, C. B., "A Detailed Investigation into Cross-Spectral Laser Doppler Techniques for Flexural and Longitudinal Vibrational Intensity Measurements," *Proceedings of the Structural Intensity and Vibration Energy Flow; 3rd International Congress on Intensity Techniques*, 1990, pp. 173-180.

[29] Hayek, S. I., Pechersky, M. J., and Suen, B. C., "Measurement and Analysis of Near and Far Field Structural Intensity by Scanning Laser Vibrometry," *Proceedings of the Structural Intensity and Vibration Energy Flow; 3rd International Congress on Intensity Techniques,* 1990, pp. 281-288.

[30] Bouthier, O. M. and Bernhard, R. J., "Models of Space Averaged Energetics of Plates," *AIAA Journal,* Vol. 30, No. 3, 1992, pp. 616-623.

[31] Tanaka, N., Synder, S. D., Kikushima, Y., and Kuroda, M., "Vortex Structural Power Flow in a Thin Plate and the Influence on the Acoustic Field," *Journal of the Acoustical Society of America*, Vol. 96, 1994, pp. 1563-1574.

[32] Gibbs, G. P., "Simultaneous Active Control of Flexural and Extensional Power Flow in Thin Beams," Ph.D. Dissertation, Virginia Polytechnic Institute and State University, Department of Mechanical Engineering, Blacksburg, VA, 1993.

[33] Miller, D. W. and Hall, S. R. "Experimental Results Using Active Control of Traveling Wave Power Flow," *Journal of Guidance, Control, and Dynamics*, Vol. 14, No. 2, 1991, pp. 350-359.

[34] Pan, J. and Hansen, C. H., "Active Control of Vibratory Power Flow in a Beam Part I: Physical System Analysis," *Journal of the Acoustical Society of America*, Vol. 89, No. 1, 1991, pp. 200-109.

[35] Norwood, C. J., and Wood, L. A., "Damping Fault Detection Using Structural Intensity," *Proceedings of the Structural Intensity and Vibration Energy Flow; 3rd International Congress on Intensity Techniques,* 1990, pp. 323-330.

[36] Centre Technique Des Industries Mecaniques, *Proceedings of The Structural Intensity and Vibration Energy Flow; 4th International Congress on Intensity Techniques.* Senlis, France, 1993.

[37] Lee, D., Berthelot, Y. H., and Jarzynski, J., "A Laser Probe for Measurements of In-Plane Structural Vibrations," *Proceedings of the Structural Intensity and Vibration Energy Flow; 3rd International Congress on Intensity Techniques,* 1990, pp. 181-288.

[38] The 1995 International Congress on Noise Control Engineering, *Proceedings of Inter Noise 1995, Edited by Bernhard, R. J. and Bolton, J. S.*, New Port Beach, CA, 1995.

[39] Morikawa, R., Nakamura, K., and Ueha, S., "Structural Intensity Derivation Using Normal and In-plane Vibration Displacements Measured by A Laser Doppler Vibrometer," *Proceedings of Inter-Noise 1995, Edited by Bernhard, R. J. and Bolton, J. S.*, Vol. 1, 1995, pp. 637-640.

[40] Benes, E., Exner, C., Focke, C. Groschl, M., and Pavic, G., "Multipoint Optical Measurement of Structural Intensity," *Proceedings of Inter-Noise 1995, Edited by Bernhard, R. J. and Bolton,*, Vol. 1, 1995, pp. 665-668.

[41] Mitchell, L. D., Blotter, J. D., and West, R. L., "Calibration, Who Needs Calibration," *Proceedings of the 15th International Modal Analysis Conference*, to be published.

[42] Drain, L. E., The Laser Doppler Technique, John Wiley and Sons Ltd., 1980.

[43] Galaitsis, G. S., "Calibration of VPI laser head with low-pass filter removed," *Laser Tasks Instructions Manual*, Virginia Polytechnic Institute and State University, Modal Analysis Laboratory, Blacksburg, VA, 1991.

[44] Zeng, X. Mitchell, L. D., and Agee, B. L., "A Laser Position Determination Algorithm for an Automated Mechanical Mobility Measurement System," *Proceedings of the 11th International Modal Analysis Conference,* Kissimmee, FL, 1993, pp. 122-129.

[45] Lindholm, B. E., "Three-Dimensional Position Registration of a Scanning Laser Doppler Vibrometer," *Proceedings of the 14th International Modal Analysis Conference*, 1996, pp. 830-836.

[46] Cook, R. D., Malkus, D. S., and Plesha, M. E., Concepts and Applications of Finite Element Analysis Third Edition, John Wiley and Sons Ltd., 1989, pp. 457.

[47] Kreyszig, E., Advanced Engineering Mathematics Sixth Edition, John Wiley, 1988, pp. 325.

[48] Bartels, R. H., Beatty, J. C., and Barsky, B. A., An Introduction to Splines for Use in Computer Graphics and Geometric Modeling, Morgan Kaufmann Publishers, Inc., Los Altos, CA, 1987.

[49] Blotter, J. D. and West, R. L., "Experimental Mechanical Intensity In Plates Using A Scanning Laser Doppler Vibrometer," *Proceedings of the 13th International Modal Analysis Conference*, 1995, pp. 762-772.

[50] Shames I. H. and Dym, C. L., Energy and the Finite Element Methods in Structural Mechanics, Hemisphere Publishing Corporation, 1985, pp. 183-188.

[51] Cremer, L., Heckl, M., and Ungar, E. E., Structure-Borne Sound, Springer-Verlag, New York Berlin Heidelberg, 1973.

[52] Maysenholder, W., "The Reactive Intensity of General Time-Harmonic Structure-Borne Sound Fields," *Proceedings of the Structural Intensity and Vibration Energy Flow; 4th International Congress on Intensity Techniques,* Senlis, France, 1993, pp. 63-70.

[53] Meirovitch, L., Elements of Vibration Analysis, McGraw-Hill, 1986, pp. 221.

[54] Pinnington, R. J., and White, R. G., "Power Flow Through Machine Isolators To Resonant and Non-resonant Beams," *Journal of Sound and Vibration*, Vol. 75 No. 2, 1981, pp. 179-197.

[55] J. W. Verheij, "Cross Spectral Density Methods for Measuring Structure Borne Power Flow on Beams and Pipes," *Journal of Sound and Vibration,* Vol. 70, 1980, pp. 133-139.

[56] Pavic, G. "Energy Flow Induced by Structural Vibrations of Elastic Bodies," *Proceedings of the Structural Intensity and Vibration Energy Flow; 3rd International Congress on Intensity Techniques*, 1990, pp. 21-28.

[57] Barker, A. H., Jaeger, P. E., and Oliver, D. E., "Non-Contacting Vibration Measurement: Role in Design and Industrail Applications," *Proccedings of the Third International Conference on Stress Analysis by Thermoelastic Techniques*, SPIE Vol. 1084, 1989, pp. 293.

[58] Ometron VPI Sensor Operator's Manual.

Appendix A

Scanning Laser Doppler Vibrometer

A.1 General Overview of the SLDV

The scanning laser Doppler vibrometer (SLDV) used in this research was an Ometron Vibration Pattern Imaging Sensor (VPI). This laser is manufactured and sold by Ometron Limited based in London, England. The original development of the SLDV was conceived by Drain and Moss [42]. The SLDV contains a Class II He-Ne source with a maximum emitted radiation of 1 mW. Velocity amplitudes in the range of 0 to ± 1 m/s from DC to 100 kHz can be measured at working distances of up to 200 m. The SLDV has three dynamic ranges. The velocity amplitudes for these ranges are 0-0.01 m/s, 0-0.1 m/s, and 0-1.0 m/s. The accuracy of the output of the sensor is approximately $\pm 3\%$ of full scale for each of the three ranges.

The SLDV is a scanning system which has two mirrors that position the laser beam under manual or computer control. The mirror deflection range is ± 12.5 degrees in both the vertical and horizontal directions. The SLDV is best suited for in door use but theoretically capable of high performance under extreme environmental conditions.

The underlying principles of the SLDV are quit simple in nature. The familiar passing of a car with a siren is a good example of how sound waves change frequency when emitted from a moving source. In the same manner that sound waves reflected from, or

emitted by, a moving object suffer a frequency change a beam of light reflected from a moving surface also experiences a change in frequency. The small change in frequency of the light wave can be measured very accurately using optical interferometry and electronic frequency measurement.

A.2 SLDV Measurement Principle

The SLDV is based on a Michelson interferometer in that the laser beam is divided into a reference beam and a signal beam as shown in Fig. A.1. The signal beam is positioned onto the vibrating structure by the scanning mirrors. As the laser beam hits the vibrating structure the light from the laser beam is scattered in all directions. The light reflected back along the signal beam is re-combined with the internal reference beam. As the structure vibrates, the path difference between the incident and reflected beams changes. This change causes an intensity modulation of the re-combined beam due to the interference between the reference and signal beams. One complete cycle of intensity modulation corresponds to a surface movement of $\frac{\lambda}{2}$ where λ is the wavelength of the He-Ne laser source. This wavelength for the He-Ne laser has been measured to be $\lambda = 3.16 \times 10^{-7}$ m. The intensity modulation frequency, F_d, is related to the surface velocity, v, as shown by Eq. (A.1)

$$F_d = \frac{2v}{\lambda} \tag{A.1}$$

The re-combined beam is then split into two beams which are detected by independent channels. The two detection channels are set such that a quarter of a wavelength difference in the interferometric paths exists. This path length difference causes a 90 degree phase shift between the two signals. In Fig. A.1 these two channels are denoted by sin and cos. The direction of the structure motion can be determined by which signal leads the other in phase. These two Doppler signals are routed into a dual channel balanced modulator and are modulated by internally generated sine and cosine signals at a carrier frequency F_c.

Summing the two modulated signals results in a single frequency shifted output signal at a frequency of $F_c + F_d$ or $F_c - F_d$ depending on the direction of motion. This signal is also known as a Single Side Band Suppressed Carrier which is denoted SSBSC in the figure. An electronic frequency tracking circuit is then used to derive an analog voltage which represents the velocity of the vibrating surface [57][58].

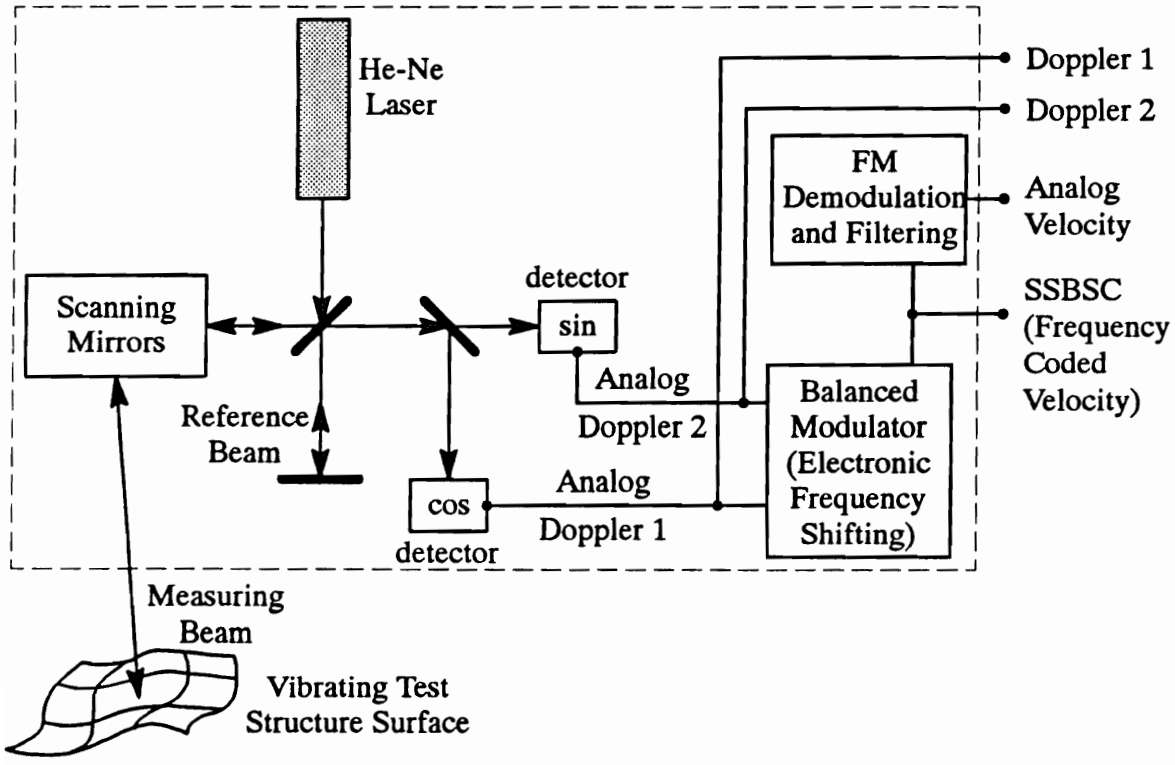

Figure A.1. Schematic of the LDV Instrument

Appendix B

ESPF Computer Code Flow Chart

The ESPF method consists of three main stages. Stage 1 is the data acquisition which consists of the signal processing code developed by Doktor and Montgomery [2]. Stage 2 consists of code developed for the laser registration process and the ESDM velocity-field solution. Details of this code were presented by Montgomery [2]. Stage 3 of the ESPF method computes the power from the velocity field obtained in Stage 2. A flow diagram of the computer code developed for Stage 3 is shown in Fig. B.1. The program names are shown in bold letters.

The Stage 3 computer code consists of first rearranging the format of the control points that are used represent the velocity field. This task is performed by the program "CP2.m" which is written in Matlab. All the other code is written in Mathematica. The only input required for CP2.m is the number of elements in the velocity model and the control point obtained by the ESDM computer code.

After the control points have been rearranged the derivatives required in the power equations are computed by running a program called Main_Deriv_Comp. Main_Deriv_Comp is written in a Mathematica Notebook. This is the main program which calls several sub-programs to compute the derivatives. The first process performed in Main_Deriv_Comp is the mapping of the points where the power is to be computed to (x,y) and (ξ, η) coordinates. This is done through the sub-program XI_ETA. The input to XI_ETA

is the number of elements in the velocity model and the number of points where the power is to be computed. The second process consists of executing two programs in an interactive fashion for each point at which the power is computed. These two programs are EXT_VEL and GFORCE_AVEL. EXT_VEL computes the transverse velocity at each point and GFORCE_AVEL computes all the generalized forces and angular velocities.

After Main_Deriv_Comp has finished, pfp1 which is another Mathematica Notebook program is used to compute the power from the derivatives obtained from the output of Main_Deriv_Comp. In this program the material properties, plate thickness, and forcing frequency are entered. This program also plots the power-vector field.

The laser data sets, registration files, impedance head data files, and the velocity solutions are currently located on the HP workstation, snoopy, in the directory ../blotter/Research. Under this directory the file names clearly indicate the associated content.

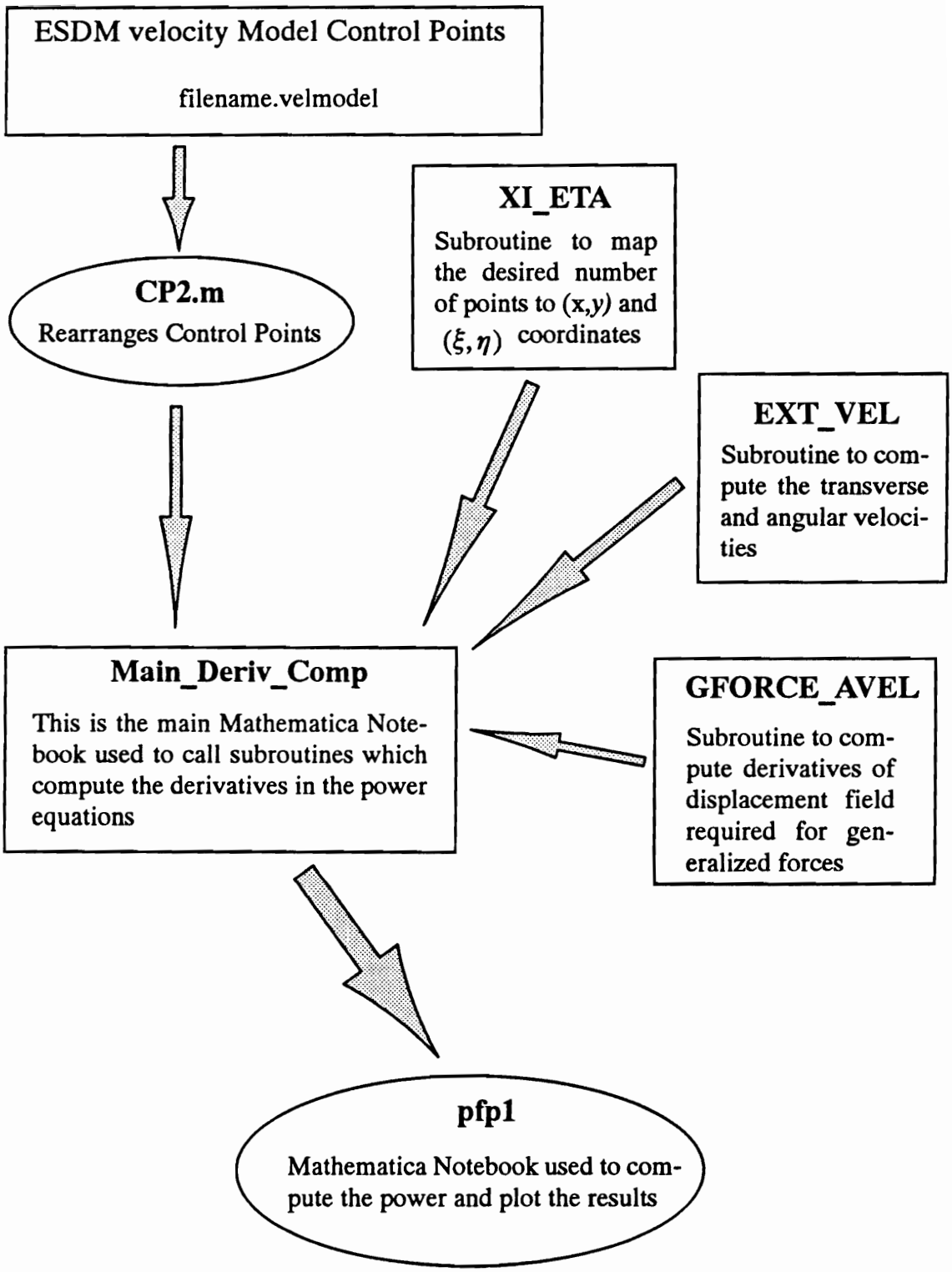

Figure B.1. Flow chart of the ESPF computer code

Vita

Jonathan Daren Blotter was born in Logan, Utah on August 30, 1965. He graduated from Sky View High School in 1983. After returning from a two year church mission in Honduras and Belize he attended Brigham Young University in the fall of 1986. He married Marjorie E. Jones on August 24, 1988 in Logan, Utah. After his marriage Jonathan continued his studies in Mechanical Engineering at Utah State University in Logan, Utah where he received his Bachelor of science degree in 1991 and his Master of Science degree in 1993. His thesis work dealt with analytical modeling of stress and strain in circular tunnels in rock. This research was funded by and eventually lead to permanent employment with Defense Group Incorporated, Engineering and Analysis in Arlington, Virginia. In January of 1993, after a year in Arlington, Jonathan and his family moved to Blacksburg, Virginia to pursue a Ph.D. in Mechanical Engineering at Virginia Tech. After completing his Ph.D. in August of 1996, Jonathan accepted a tenure-track assistant professor position at Idaho State University where he plans to pursue his research interests and continue to develop his teaching skills.